Surface Deformations of Magnetic Continua in Homogeneous Fields

Von der Universität Bayreuth
zur Erlangung des Grades eines
Doktors der Naturwissenschaften (Dr. rer. nat.)
genehmigte Abhandlung

von

Christian Gollwitzer

aus Weiden i.d.OPf

1. Gutachter: Prof. Dr. Ingo Rehberg
2. Gutachter: PD Dr. Stefan Wehner

Tag der Einreichung: 15.12.2009
Tag des Kolloquiums: 04.03.2010

Zusammenfassung

Diese Arbeit beschäftigt sich mit magnetischen Flüssigkeiten und Gelen. Bei diesen auch *Ferrofluide* bzw. *Ferrogele* genannten Materialen handelt es sich um synthetisch hergestellte Suspensionen magnetischer Nanoteilchen in einer Trägerflüssigkeit (Rosensweig 1985), die im Fall des Gels zusätzlich noch geliert wird (Zrínyi *et al.* 1997*a*). In ihren magnetischen Eigenschaften ähneln Ferrofluide und -gele den gewöhnlichen Paramagneten, jedoch übertreffen sie diese um einen Faktor $10^3 \ldots 10^5$ in der Suszeptibilität und werden daher auch als *superparamagnetisch* bezeichnet.

Seit der ersten erfolgreichen Synthese von Ferrofluiden durch Papell (1965) und der Entdeckung der Normalfeldinstabilität durch Cowley & Rosensweig (1967) wurden eine Reihe grundlegender Experimente und einige technische Anwendungen vorgeschlagen, von denen einige bereits kommerziell im Einsatz sind; ein Überblick dazu findet sich in dem von Odenbach (2009) herausgegebenen Buch. Die meisten der technischen Anwendungen basieren auf der
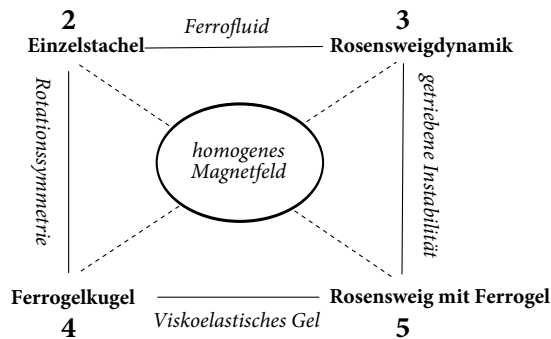

ABBILDUNG Z.1: Graphische Übersicht über die Beziehungen zwischen den Experimenten in dieser Arbeit. Die Kurznamen und Nummern der Kapitel sind in den Ecken angeordnet, die kursiv gedruckten Eigenschaften auf den Verbindungslinien zeigen die Beziehungen zwischen den Kapiteln an.

Fähigkeit der magnetischen Fluide und Gele, ihre Form und Fließeigenschaften unter Einfluss eines Magnetfeldes zu verändern (Zrínyi *et al.* 1997*b*), beziehungsweise im inhomogenen Magnetfeld eine Kraft in Richtung des Gradienten zu erfahren (Lange 2002*b*). Eine Verformung kann jedoch auch im homogenen Feld hervorgerufen werden. Hierzu werden in dieser Arbeit vier Experimente vorgestellt, die die Formänderungen beim Anlegen eines homogenen Magnetfeldes untersuchen.

Dafür werden zwei grundlegende Geometrien herangezogen: Eine Kugel aus magnetischem Material und eine ausgedehnte flache Schicht. Im ersten Fall führt das Anlegen eines Feldes zur Deformation der Kugel in ein prolates Ellipsoid, wobei die längere Achse parallel zu den Feldlinien ist. Dieser Effekt wird von Raikher & Stolbov (2003) als »Magnetodeformation« bezeichnet und in dieser Arbeit erstmalig mit Ferrogel experimentell realisiert. Im Fall der ausgedehnten Schicht werden durch ein Magnetfeld, welches senkrecht zu der Schicht verläuft, regelmäßig angeordnete Stacheln an der Oberfläche hervorgerufen, die sogenannte Rosensweig- oder Normalfeldinstabilität (Cowley & Rosensweig 1967). Im Unterschied zu der Kugelgeometrie handelt es sich bei diesem Phänomen um eine symmetriebrechende Instabilität der Oberfläche, welche erst oberhalb einer Schwelle B_c der magnetischen Induktion auftritt, während die Kugel bereits bei beliebig kleinem externen Magnetfeld deformiert wird.

Die Beziehungen zwischen den einzelnen Experimenten in dieser Arbeit stellt Abbildung Z.1 in graphischer Form dar. Jedes Kapitel beleuchtet die Verformung der magnetischen Kontinua im homogenen Feld aus einem anderen Blickwinkel, wirft aber auch neue Fragen auf, die insbesondere als Aufforderung an die Modellbildung gerichtet sind. Im Folgenden sollen die einzelnen Experimente kurz zusammengefasst werden.

Teil I beschreibt Experimente mit Ferrofluiden. Kapitel 2 behandelt die Normalfeldinstabilität, wobei die Größe des Gefäßes bewusst reduziert wird, bis nur noch ein einzelner Ferrofluidstachel im Zentrum des zylinderförmigen Gefäßes entsteht. Die möglichen Oberflächenformen sind also zylindersymmetrisch und damit leicht zugänglich für numerische Simulationen und experimentelle Messmethoden. Zwei unterschiedliche Messverfahren zur Bestimmung der Amplitude des zentralen Stachels werden verwendet und miteinander verglichen: Die Röntgenabsorptionsmethode nach Richter & Bläsing (2001), bei der die Schichtdicke des Fluids aus radioskopischen Bildern bestimmt wird, und die

Lasermethode nach Megalios *et al.* (2005), bei der ein Laserstrahl auf die freie Oberfläche fokussiert wird. Es ergibt sich eine sehr gute Übereinstimmung bis auf wenige Prozent zwischen den Experimenten und den Rechnungen, die in enger Zusammenarbeit von einer Gruppe um A. Boudouvis an der technischen Universität in Athen (NTUA) durchgeführt wurden. Es bleibt die Frage offen, ob sich ein analytischer Ausdruck für die Oberflächendeformation in dieser symmetrischen Geometrie finden lässt.

In Kapitel 3 wird ein hochviskoses Ferrofluid verwendet, um die nichtlineare Dynamik der Musterbildung der Rosensweiginstabilität zu untersuchen. Aus den Messdaten wird die lineare Wachstumsrate für kleine Amplituden extrahiert, welche mit einer Theorie von Knieling *et al.* (2007) verglichen wird. Das Messverfahren erlaubt darüber hinaus die Bestimmung einer vollständig nichtlinearen Amplitudengleichung, die mit theoretischen Modellen qualitativ verglichen wird. Die Modelle können bislang allerdings nur in einem engen Bereich um den kritischen Punkt Aussagen treffen und daher nicht quantitativ mit den Messdaten verglichen werden. Die Aufgabe, die an die Modellbildung gestellt wird, besteht also darin, Modelle mit einem größeren Gültigkeitsbereich aufzustellen. Außerdem wird die spontane Entstehung von lokalisierten Mustern beobachtet, die in der Nähe der instabilen Lösung auftreten. Ähnliche Muster wurden von Richter & Barashenkov (2005) durch eine externe Störung erzeugt. In nachfolgenden Experimenten kann die spontane Entstehung dieser Zustände näher untersucht werden.

Teil II der Arbeit beschreibt Experimente mit thermoreversiblen Ferrogelen (Lattermann & Krekhova 2006), die im Rahmen der Forschergruppe 608 der DPG von einer Arbeitsgruppe aus der Chemie zur Verfügung gestellt wurden. Kapitel 4 widmet sich der Magnetodeformation. Eine Kugel aus Ferrogel wird einem homogenen Magnetfeld ausgesetzt. Das plötzliche Einschalten des Feldes führt neben der Streckung in Feldrichtung zu einer Schwingung der Kugel um den neuen Gleichgewichtspunkt. Die Deformation der Kugel nimmt zusätzlich auf einer längeren Zeitskala kontinuerlich zu aufgrund der viskoelastischen Eigenschaften des verwendeten Ferrogels. Beide Phänomene können durch einen modifizierten harmonischen Oszillator beschrieben werden, dessen Federkonstante sich mit der Zeit verändert. Aus der Deformation in Feldrichtung und senkrecht dazu lässt sich die Poissonzahl des sehr weichen Gels ermitteln, welche anderweitig schwierig zu messen ist. Es zeigt sich, dass das Gel nahezu inkompressibel ist. Die absoluten Werte für die Deformation werden mit zwei

Theorien von Landau & Lifschitz (1960) und Raikher & Stolbov (2005*a*) verglichen, die allerdings nur den statischen Fall ohne viskosen Fluss berücksichtigen. Die gemessenen Deformationen übersteigen die berechneten Werte um 70 %. Es bleibt zu klären, ob eine Erweiterung der Theorie auf den dynamischen Fall mit einem viskoelastischen Gel diese Diskrepanz auflösen kann.

Kapitel 5 realisiert erstmalig die Normalfeldinstabilität mit einem Ferrogel, die von Bohlius *et al.* (2006*a*) vorhergesagt wurde. Eine flache Schicht eines thermoreversiblen Ferrogels wird bei unterschiedlichen Temperaturen dem Magnetfeld ausgesetzt. Damit das Gel weich genug ist und die elastischen Kräfte die Oberflächeninstabilität nicht vollständig unterdrücken, muss bislang eine Temperatur im viskoelastischen Übergangsbereich verwendet werden. Das Magnetfeld wird periodisch moduliert und die Amplitude der Instabilität gemessen, die mit derselben Frequenz moduliert ist. Der Vergleich mit mechanischen Messungen zeigt, dass die Antwort linear mit der komplexen Viskosität skaliert. Für einen quantitativen Vergleich mit der Theorie von Bohlius *et al.* (2006*a*) wäre ähnlich zu Kapitel 4 eine Erweiterung der Theorie auf den dynamisch getriebenen Fall für ein viskoelastisches Gel nötig.

Insgesamt lässt sich feststellen, dass die Experimente zur Normalfeldinstabilität in dieser Arbeit verschiedene Grenzfälle untersuchen, nämlich eine seitlich begrenzte Geometrie und den Einfluss großer Viskositäten und elastischer Kräfte. Das Kapitel zur Magnetodeformation einer Ferrogelkugel liefert die ersten Messdaten zu diesem Effekt. Jedes der Experimente gibt außerdem weiterführende Anregungen für die Modellbildung.

Abstract

In this thesis, experiments with magnetic liquids and gels are presented. These *ferrofluids* and *ferrogels* are synthetically created suspensions of magnetic nanoparticles in a carrier liquid (Rosensweig 1985). By adding a gelator, such a ferrofluid can be turned into a ferrogel (Zrínyi *et al.* 1997*a*). The magnetic properties of these substances are similar to a usual paramagnet with the important difference, that the susceptibility of the former is higher by a factor of $10^3 \ldots 10^5$.

The first successful synthesis of ferrofluids by (Papell 1965) and the discovery of the normal field instability by Cowley & Rosensweig (1967) triggered a wealth of scientific research. Several technical applications have been proposed, some of which are commercially available in the meantime. For a review of these experiments and applications see e.g. the book by Odenbach (2009). Most of the technical applications are based on the Kelvin force, which pushes a paramagnetic substance in the direction of a magnetic field gradient Papell (1965), and the change of the mechanical properties and the shape in inhomogeneous fields Zrínyi *et al.* (1997*b*). A transformation of the shape can also be induced by the application of a homogeneous field. In this thesis, four experiments on the surface deformation in homogeneous magnetic fields are presented.

Two geometric configurations are considered: a horizontally extended flat layer with a free surface as well as a spherical sample. In both cases, the application of a homogeneous magnetic field leads to changes of the shape of the free boundary. In the case of the spherical geometry, the sample is deformed into a prolate ellipsoid under the action of the field, a phenomenon named "magnetodeformational effect" by Raikher & Stolbov (2003). The magnetic field presumably remains homogeneous inside the ellipsoidal sample (Jackson 1998), and the transition of the shape is smooth. In case of the extended flat layer, an abrupt shape transition into a patterned state takes place, the normal field or Rosensweig instability (Cowley & Rosensweig 1967). The magnetic field inside the sample is distorted by the transition with the same wavelength as the pattern
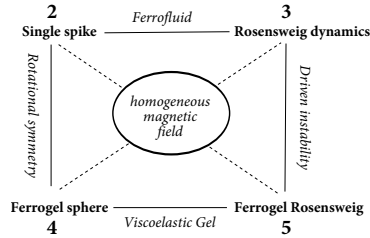
FIGURE A.1: Relations between the experiments. The numbers and the terms in boldface represent the four main chapters of this thesis. The common properties between them are marked in italics along the connecting lines (solid and dashed).

on the surface. In contrast to the smooth deformation of the sphere, this is an instability, which breaks the translational symmetry, and the transition occurs at a certain threshold value of the magnetic induction B_c.

A graphical overview of the experiments in this thesis and the relations between them is given in figure A.1. Each chapter sheds light on the surface deformations of magnetic continua from a different point of view and eventually raises new questions, which are formulated as a specific challenge to the theoretical analysis. Each of the experiments is briefly summarized in the following paragraphs.

Part I of the thesis considers ferrofluids. In chapter 2, the ideal geometry of an infinitely extended flat layer is intentionally reduced to a cylinder such that only a single spike in the centre exists, and the solution space becomes rotationally symmetric. This makes the problem very feasible for experimental methods and numerical simulations. Two measurement techniques are applied and compared to each other, namely an X-ray technique by Richter & Bläsing (2001), where the surface deformation is extracted from radioscopic images, and a laser technique by Megalios *et al.* (2005), which focuses a laser spot onto the surface. The experiments and the simulations, the latter performed in close cooperation with a group in Athens, show a convincing agreement within a few percent. It remains an open question, whether the result can be deduced in analytic form, however.

In chapter 3, a highly viscous ferrofluid is utilized to study the nonlinear dynamics of the normal field instability at very low Reynolds numbers. The linear growth rate for the growth and decay of the pattern at small amplitudes

is extracted from the measurements and compared with a theoretical model by Knieling *et al.* (2007). In addition, the measurement technique provides the reconstruction of a fully nonlinear amplitude equation, which is qualitatively compared to model equations. These nonlinear amplitude equations can only describe the dynamics of the growth in the immediate vicinity of the critical point so far. For a quantitative comparison, there is a need for a model with an extended range of validity. Additionally, localized patterns are observed which arise spontaneously in the neighbourhood of the unstable solution branch. Similar patterns have previously been observed by Richter & Barashenkov (2005) with the help of an external disturbance. An in-depth experimental study and theoretical analysis of the spontaneous formation of these patterns can be performed in future work.

Part II of the thesis deals with thermoreversible ferrogels (Lattermann & Krekhova 2006), which have been made available by a chemistry group in a common project of the German Science Foundation (Forschergruppe 608). Chapter 4 studies the magnetodeformational effect. An experimental realization of this phenomenon was completely missing, even though theoretical predictions exist since 1960. Chapter 4 fills this gap and demonstrates that the magnetodeformational effect indeed exists. A ferrogel sphere is exposed to homogeneous magnetic field. When the field is applied suddenly, the sphere not only elongates in the direction of the field, but also vibrates about the new equilibrium. On a longer time scale, the deformation continuously increases due to the viscoelastic properties of the gel. Both phenomena can well be described by a harmonic oscillator model, where the spring constant changes with time. From the deformation parallel and perpendicular to the applied field, Poisson's ratio can be calculated, which turns out to be close to the limit of incompressibility. The absolute values of the deformation are compared to the models by Landau & Lifschitz (1960) and Raikher & Stolbov (2005*a*). There is a deviation of about 70 %, that is due to the viscoelastic properties of the ferrogel, which are not taken into account in the static models. Therefore the experiment challenges the theoretical analysis to provide a dynamic theory, which can incorporate viscoelastic material properties, especially time dependent elastic moduli.

In chapter 5, the normal field instability is realized for the first time with a ferrogel. This experiment has been proposed by Bohlius *et al.* (2006*a*). A flat layer of a thermoreversible ferrogel is exposed to a homogeneous magnetic field

at different temperatures, where the gel is viscoelastic. This is a consequence of the need for a very soft material, such that the growth of the pattern is not completely suppressed by the elastic forces. The magnetic field is periodically modulated in time, and the amplitude of the instability is measured, which is modulated with the same frequency. The comparison with rheological measurements reveals a scaling of the modulated amplitude with the complex viscosity of the ferrogel. The theory by Bohlius *et al.* (2006*b*), on the other hand, does not account for viscoelastic effects and a modulated field. An extension of the theory, which incorporates viscoelasticity and an external driving, is therefore needed to quantitatively compare the experimental results with, similar to the case of the ferrogel sphere.

To conclude, the surface deformation of magnetic continua in homogeneous fields has been examined on the basis of four phenomena. While the experiments on the normal field instability examine different limiting cases, namely a confined geometry and the influence of high viscosity and viscoelasticity, the chapter about the magnetodeformational effect with a ferrogel sphere provides the first experimental data. Each experiment shows aspects which are not yet completely understood and poses a challenge to the theoretical analysis. Further experimental work can be directed towards unexplored phenomena such as the spontaneous formation of localized patterns.

Contents

1 Introduction

Magnetism is one of the oldest physical phenomena observed by mankind. From the first observation, that lodestone has the mysterious power to attract iron, magnetism has kept on fascinating people until today (Hickey & Schibeci 1999). The Greek word *ὁ μαγνήτης λίθος* , from which *magnet* is derived, literally translates into "the stone from Magnesia", a place in Asia Minor where lodestone has been mined (Merriam-Webster 1999). It was not until the 19th century, that Ørsted (1821) discovered the connection between magnetism and an electric current. He observed, by accident, that a magnetic needle is influenced by an electric current flowing in a nearby wire. He also coined the term electromagnetism upon his discovery and paved the way to a unified theory of electricity and magnetism, eventually completed by Maxwell (1861).

Before the important contributions of the 19th century, physicists believed that magnetism of matter is restricted to a few solid materials, like lodestone and iron. The very weak effects of dia- and paramagnetism in virtually all matter, previously overlooked because of their small impact in macroscopic experiments, have been observed and described in detail by Faraday (1846). He also examined the magnetic properties of several fluids like water, alcohol, ether,

FIGURE 1.1: A lodestone attracting some paper clips. Taken from Wikipedia (2009).
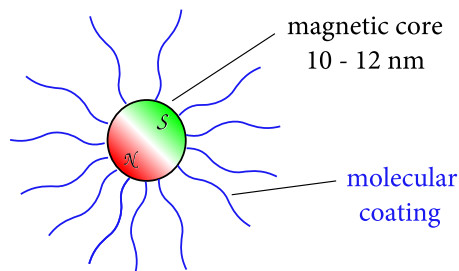
FIGURE 1.2: A magnetic nanoparticle. It consists of a ferromagnetic single-domain core, which is covered by a surfactant.

magnetic core
10 - 12 nm

molecular
coating

blood, and air, and found them to be diamagnetic. However the magnetism of these substances is considerably smaller than that of ferromagnetic bodies. Faraday (1846) himself stresses the fact, that "the effects [of diamagnetism] require magnetic apparatus of great power and under perfect command." Until today, no pure fluid is known that exhibits magnetism with a strength comparable to a ferromagnetic solid. The strongest known paramagnetic fluid, liquid oxygen, has a susceptibility of $\chi = 4.1 \cdot 10^{-3}$ (Fleming & Dewar 1898), six orders of magnitude smaller than the typical susceptibility of iron.

It is, however, possible to synthesize magnetic fluids with a susceptibility of $\chi \approx 1$ to 10 by suspending ferromagnetic nanoparticles (cf. figure 1.2) in a non-magnetic carrier liquid (Papell 1965). These particles typically consist of a ferromagnetic core made of magnetite (Fe_3O_4) or cobalt, coated with a surfactant. Such a magnetic fluid, also called ferrofluid, forms a stable suspension. The core of the particles has a diameter in the range of a few nanometres up to $\approx 20\,$nm and consists of a single magnetic domain. It is therefore permanently magnetized. The coating is necessary to inhibit the agglomeration of the particles due to Van-der-Waals or dipolar interaction, and the size of the particles must be small enough that their Brownian motion prevents them from sedimentation. The paramagnetic transition of the core establishes a lower limit of the size – beyond a critical size of the particles, the magnetic cores become paramagnetic and loose their permanent magnetic moment.

From a macroscopic point of view, a ferrofluid can be seen as a magnetizable, homogeneous dark brown to black liquid (Rosensweig 1985). One caveat: although these magnetic fluids are called *ferro*fluids, their total magnetization vanishes in the absence of an external magnetic field, even though the particles itself do have ferromagnetic ordering. This is due to the thermal fluctuations of the orientation of the magnetic moments, which lead to an overall zero magne-

tization. Consequently, ferrofluids appear as strongly paramagnetic liquids, and thus are often called *superparamagnetic*. Many of the properties of ferrofluids seen in macroscopic experiments can be understood satisfactorily from this viewpoint. Only sometimes, more insight is provided by thinking in terms of individual particles.

In contrast to a magnetizable solid, a ferrofluid has an additional degree of freedom, namely its shape. While it is generally possible, that a ferromagnetic solid changes its shape in response to an applied magnetic field – a phenomenon called magnetostriction (Joule 1842) –, a liquid has no preferred configuration and thus can change its shape much more easily. The deformation achieved by magnetostriction of ferromagnetic crystals is typically less than 1 %. Joule (1842), who first described magnetostriction after being given a hint "a few weeks ago [by] an ingenious gentleman of this town", measures a relative deformation of ½₀₀₀₀ for iron and states, somewhat disappointed, "with regard to the application of this new force to the movement of machinery, I have nothing favourable to advance." Nevertheless, using modern magnetostrictive materials, a deformation of a few percent is possible, which is termed "giant" (Kakeshita *et al.* 2000). In contrast, a ferrofluid volume can easily be deformed by several 100 % under the influence of a magnetic induction of only a few mT (Bacri & Salin 1982). This opens up opportunities for new physical phenomena. Landau & Lifschitz (1960) dedicate a whole volume of their series of textbooks on theoretical physics to the description of continuous media in conjunction with electric and magnetic fields. But before the invention of magnetic nanoparticles, experimentalists have been restricted to very small susceptibilities, when a deformable material was needed in the magnetic case. The successful synthesis of ferrofluids therefore triggered a lot of scientific research (Rosensweig 1987), and also a wide range of technical and medical applications has been proposed, a few of which are already in daily use. Among the commercially available products are ferrofluidic seals, hi-fi loudspeakers and material separation (Berkovski & Bashtovoy 1996; Blums *et al.* 1997). Upcoming technical and medical applications are e.g. described in the review articles by Bayat *et al.* (2009) and Trahms (2009).

In addition to ferrofluids, we also consider ferrogels. A *ferrogel* is a polymer gel with added magnetic nanoparticles, so that the magnetic properties are similar to ferrofluids, while the mechanic properties resemble those of a gel (Zrínyi *et al.* 1997*a*). In contrast to the aforementioned ferromagnetic solids, these gels

Figure 1.3: A photograph of the Rosensweig instability.

are rather soft – the shear modulus is of the order 10 kPa, which is six to seven orders of magnitude softer than ferromagnetic metals. Therefore, the response of a ferrogel to magnetic fields, i.e. the change of its shape, can be expected to be comparable in magnitude as for a true ferrofluid, while there exists a preferred configuration when no field is applied. Many new applications are proposed for such an elastic, yet soft and responsive material like magnetic soft actuators, magnetic valves, magnetoelastic automotive robots (Zimmermann *et al.* 2006, 2007), artificial muscles (Babincová *et al.* 2001), and magnetically controlled drug delivery (Lao & Ramanujan 2004).

Most of these applications involve the use of inhomogeneous magnetic fields. In a gradient magnetic field, the Kelvin force $\mu_0(\boldsymbol{M}\nabla)\boldsymbol{H}$ attracts a paramagnetic material towards the stronger magnetic field. In this way Zrínyi *et al.* (1996), e.g., achieved very large deformations of a ferrogel sample. In this thesis, we will focus on the shape transitions of magnetic continua in *homogeneous magnetic fields.* The most prominent of these phenomena is certainly the normal field, or Rosensweig, instability found by Cowley & Rosensweig (1967). When a flat layer of magnetic liquid is exposed to a magnetic field which is oriented normal to the surface, i.e. parallel to the gravity, the previously flat

(a)   (b)
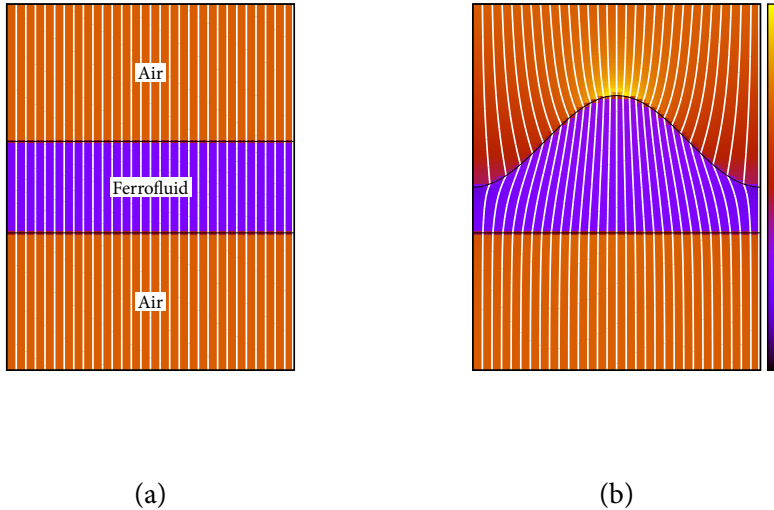
FIGURE 1.4: Magnetic field in a ferrofluid layer surrounded by air, when the layer is flat (a) and distorted by a hump (b). The direction and strength of the magnetic field $\boldsymbol{H}$ (in arbitrary units) is shown by the field lines and the colour code, respectively.

surface can deform into an array of spikes (cf. figure 1.3). The distance of these spikes is typically around 1 cm and the height varies from a few mm to a few cm.

A basic intuitive explanation of this striking phenomenon can be given by simple energy considerations. The total free energy of a liquid at rest consists of three contributions, namely the gravitational, or hydrostatic energy, the surface energy and, in case of a magnetizable liquid, the magnetic field energy (Rosensweig 1985)

$$E_{\text{total}} = E_{\text{hyd}} + E_{\text{surf}} + E_{\text{mag}}.$$

Figure 1.4 (a) displays a flat layer of magnetic liquid in a homogeneous magnetic field. When the flat surface is disturbed to form a hump (figure 1.4 b), the gravitational energy increases, because fluid needs to be raised to the tip of the spike. Likewise, the increase of the total surface enlarges the surface energy.

On the other hand, the total magnetic energy decreases. To see this, recall that the demagnetizing field contributes positively to the overall energy – a paramagnetic needle orients parallel to the field lines in the effort to decrease the demagnetizing field. In the case of a flat layer with the maximum possible demagnetization factor 1, the formation of a hump also decreases the magnetic field energy as it reorients the paramagnetic liquid parallel to the field lines. The energy reduction by this change of the geometry grows with the field strength, while the energy increases due to gravitational and surface terms are constant with respect to the magnetic field. Consequently, the total free energy E_{total} can be decreased by the formation of spikes above a certain threshold value B_c of the magnetic induction. A more rigorous derivation from this energy balance leads directly to the complete bifurcation scenario for the Rosensweig instability and has been first performed by Gailitis (1977) and later on refined by Friedrichs & Engel (2001) in the form of a weakly nonlinear approximation. Bohlius *et al.* (2006*b*) finally extended it to the case of a ferrogel.

This thesis is divided into two parts. In part I we consider usual ferrofluids. Chapter 2 describes an experiment with a reduced size of the vessel containing the ferrofluid, such that only a single spike exists in the middle of the container. We compare measurements done with two entirely different experimental methods with the outcome of a numerical simulation (Gollwitzer *et al.* 2009*b*).

In chapter 3 we examine the dynamics of the pattern on the surface, when the magnetic field is changed suddenly. To do this, we use a highly viscous ferrofluid that is additionally cooled to increase its viscosity even further. This slows down the dynamics of the system to a time scale that is easily accessible by the experiment.

Part II deals with thermoreversible magnetic gels (Lattermann & Krekhova 2006). In chapter 4 we examine a ferrogel sphere in a homogeneous magnetic field. According to simple energy considerations, the sphere must elongate in the direction of the magnetic field. This problem dates back to Landau & Lifschitz (1960), and has been recomputed recently by Raikher & Stolbov (2005*a*). After the results from chapter 4 have been published (Gollwitzer *et al.* 2008), Morozov *et al.* (2009) offered yet another theoretical variation on this topic.

In chapter 5 we describe the realization of the Rosensweig instability with magnetic gels. A theoretical model by Bohlius *et al.* (2006*a*) modifies the description of the Rosensweig instability incorporating elasticity to describe

surface instabilities in magnetic gels. We use a thermoreversible ferrogel to examine the normal field instability and compare the result to the model by Bohlius *et al.* (2006*a*). These results are published in Gollwitzer *et al.* (2009*a*).

A more detailed introduction to these topics is given separately in each chapter.

Part I

Ferrofluids

2 A single ferrofluid peak in a cylindrical container

A small cylindrical container is filled with ferrofluid and exposed to a normal magnetic field. The diameter of the container is chosen such, that no extended pattern appears on the surface, but only a single spike in the centre. This confined geometry makes the problem very feasible for both experimental methods and numerical simulations. The height of the spike as a function of the applied magnetic induction and its shape have been determined using two different experimental methods, namely an X-ray technique by Richter & Bläsing (2001) and a laser method following Megalios *et al.* (2005). The results compare very well to computer simulations, which have been carried out in the group of A. Boudouvis at the National Technical University of Athens. This chapter poses two questions – how does the confined geometry change the pattern on the surface, and how well do the experimental and numerical methods match, when there are realistic assumptions about the geometry and the material parameters. The results in this chapter have been published as a regular article in the New Journal of Physics (Gollwitzer *et al.* 2009*b*).

2.1 Introduction

Rotational symmetric systems with broken up-down symmetry become first unstable due to a transcritical bifurcation to hexagons, which is hysteretic (Cross & Hohenberg 1993). Examples are non-Boussinesq Rayleigh-Bènard convection (Busse 1967) and chemical reactions (Turing 1952). It also holds for the Rosensweig, or normal field, instability, when a layer of magnetic fluid is exposed to a normal magnetic field. The first observation of this instability by Cowley & Rosensweig (1967) and its explanation with a linear stability analysis in the same article 40 years ago triggered numerous efforts to describe also the nonlinear aspects of the phenomenon theoretically. Gailitis (1977), later

Friedrichs & Engel (2001) and Friedrichs (2002) and most recently Bohlius *et al.* (2006*b*) used the principle of free energy minimization to predict the pattern ordering, wavelength and final amplitude of the peaks on an infinitely extended surface. The numerical computations by Boudouvis (1987) and Boudouvis *et al.* (1987) predict quantitatively the hysteresis in spike height in unbounded ferrofluid pools. Matthies & Tobiska (2005) calculate also the dynamics of an infinite periodic lattice of peaks.

The experiments, however, are performed with limited amounts of fluid. A finite layer depth in the vertical dimension has been incorporated into the theory by Friedrichs & Engel (2001). According to Lange *et al.* (2000), the infinitely deep limit is well approximated if the depth exceeds at least the wavelength of the pattern. However, in the horizontal dimension the finite container size has not been considered. Therefore, experimental realizations approximated this limit of an infinitely extended layer by several different approaches. Abou *et al.* (2001) used a very large aspect ratio, whereas Gollwitzer *et al.* (2007) employed an inclined container edge. Richter & Barashenkov (2005) used a magnetic ramp to minimize the influence of the border for the Rosensweig instability, whereas Embs *et al.* (2007) independently applied it to the Faraday instability in ferrofluid.

The question arises, what happens if the container size is intentionally reduced until only a single spike is left. In this case, all symmetries are kept, nonetheless the character of the bifurcation may change. Indeed, in experiments before the seminal work of Bacri & Salin (1984), it was difficult to uncover a hysteresis due to the small container size.

Although there have been numerous experiments in small containers merely because they are simple and cheap, a systematic study of the influence of the constrained geometry on the bifurcation is missing. One reason is, that model descriptions which deal with the finite container size are rare. So far, we know only the work by Friedrichs & Engel (2000) where the free surface is modelled by a four parameter function to fit the measurements by Mahr & Rehberg (1998). In this case, a highly susceptible fluid still showed a hysteretic transition.

In the present chapter, we demonstrate, that a transcritical bifurcation to hexagons, as found by e.g. Gollwitzer *et al.* (2007), becomes an imperfect super-critical bifurcation to a single spike, if the container size is reduced sufficiently. This is the outcome of a numerical model which is able to calculate the stable and unstable solutions for given container size and fluid parameters. It also

Quantity		Value	Error
Surface tension[a]	σ	30.57	$\pm 0.1\,\mathrm{mN\,m^{-1}}$
Density	ρ	1236	$\pm 1\,\mathrm{kg\,m^{-3}}$
Contact angle with the container wall	α_c	10	$\pm 0.3\,^\circ$
Viscosity	η	120	$\pm 5\,\mathrm{mPa\,s}$
Saturation magnetization	M_S	28.7	$\pm 0.4\,\mathrm{kA\,m^{-1}}$
Initial susceptibility	χ_0	1.2023	± 0.005
Exponent of the Γ-distribution	α	6.3892	± 0.5
Typical diameter	d_0	0.962	$\pm 0.03\,\mathrm{nm}$
Volume fraction	ϕ	6.43	$\pm 0.1\,\%$

TABLE 2.1: Material properties of the ferrofluid APG 512a (Lot F083094CX) from Ferrotec Co.

---

[a]The absolute error of the measurement is unknown. The error given here
   is taken from the analysis by Harkins & Jordan (1930)

takes into account the side-wall effects, namely the wetting and the fringing field. We compare the numerical results with our measurements of the surface topography. For the first time, we apply two different techniques which are capable of recording the amplitude (Megalios *et al.* 2005) and also the full topography of the fluid surface (Richter & Bläsing 2001), to the same experiment.

In the following two sections, we give an overview of the experimental methods. Subsequently, we describe the numerical computations. Finally, we compare all three results.

2.2 Measurements of the material properties

We used the ferrofluid APG 512a (Lot F083094CX) from Ferrotec for all experiments. It is based on an ester with a very low vapour pressure, suitable for vacuum pumps. It has an excellent long-term stability. Over one year, the critical induction has not changed by more than 3 %. In contrast to less stable magnetic liquids, the formation of agglomerates in the tips of the Rosensweig spikes was not observed. After applying magnetic fields for an hour, the field was switched off. Neither the visual inspection nor the X-ray images unveiled any agglomerates at the site of the spikes.
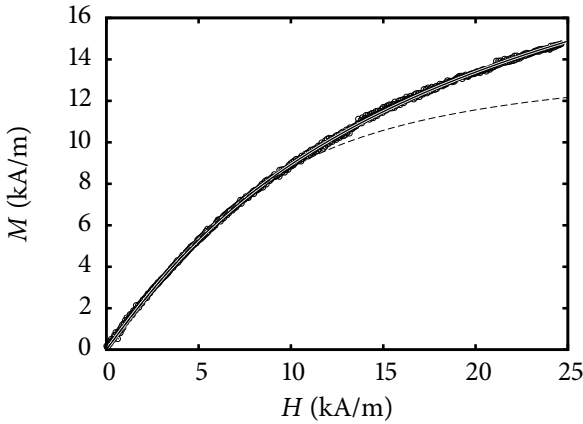
FIGURE 2.1: The magnetization curve of the ferrofluid. The circles denote the experimental values, the solid line is a fit with the model by Ivanov & Kuznetsova (2001). The dashed line is a fit with the Langevin function, that is valid only up to $H \lessgtr 10\,\mathrm{kA/m}$.

The Rosensweig instability is a counterplay between gravitational and surface terms on the one hand and magnetic forces on the other hand (Cowley & Rosensweig 1967). Therefore, a set of basic material properties of the fluid is necessary for a comparison with the theory, namely the surface tension σ, the density ρ and the magnetization curve $M(H)$. These quantities are summarized in table 2.1.

The surface tension has been measured using a commercial ring tensiometer (LAUDA TE1). This device wets a ring made from platinum wire, pulls it off the fluid surface and determines the maximum force acting on the ring, from which the surface tension can be computed following du Noüy (1919). According to an analysis by Harkins & Jordan (1930), the error for this method is smaller than 0.25 %, given that the density of the fluid and the geometry of the ring are known with sufficient accuracy.

The density ρ has been measured using a commercial vibrating tube densimeter (DMA 4100 by Anton Paar). This device enables us to determine the density with an error of 0.01 %.

The contact angle α_c was determined with the contact angle system OCA 20 (Dataphysics) by optical means. Three measurements were performed at the inner side wall of the container, which was tilted by 90 °. The difference between advancing and receding angle could not be measured in this way.

The magnetization curve $M(H)$ of the ferrofluid has the biggest influence on the surface pattern. It has been meticulously measured using a fluxmet-

ric magnetometer consisting of a Helmholtz pair of sensing coils with 6800 windings and a commercial integrator (Lakeshore Fluxmeter 480). The sample has been held in a spherical cavity with a diameter of 12.4 mm. This spherical shape ensures a homogeneous magnetic field inside the sample and an exact homogeneous demagnetization factor of ⅓, which makes it possible to get accurate results over the whole range of H. Figure 2.1 shows the magnetization curve of our ferrofluid. The solid and the dashed line provide two analytic approximations to $M(H)$. The dashed line is a fit with the Langevin approximation for monodisperse colloidal suspensions and provides the constitutive equation (Rosensweig 1985)

$$|\boldsymbol{M}| = M_{SL} L \left(3\chi_L \frac{|\boldsymbol{H}|}{M_{SL}} \right), \qquad (2.1)$$

where $L(x)$ is the Langevin function

$$L(x) = \frac{\cosh x}{\sinh x} - \frac{1}{x}. \qquad (2.2)$$

Only the data points within a range of $H \in [0\ldots10\,\text{kA/m}]$ have been taken into account for the estimation of the adjustable parameters $M_{SL} = 14.6\,\text{kA/m}$, which corresponds to the extrapolated saturation magnetization, and the initial susceptibility $\chi_L = 1.168$. A satisfying fit of the whole curve with this equation is not possible, because real ferrofluids consist of magnetic particles with a broad size distribution (Popplewell & Sakhnini 1995), which can further interact magnetically. This is also the reason for the difference between M_{SL} and the real saturation magnetization of the fluid, which is approximately twice as large according to the manufacturer information. We therefore make use of an additional model for dense polydisperse magnetic fluids derived by Ivanov & Kuznetsova (2001). This model assumes a gamma distribution of the particle diameters d with the density function

$$g_{d_0,\alpha}(d) = \frac{1}{d_0 \Gamma(\alpha + 1)} \left(\frac{d}{d_0} \right)^{\alpha} \exp\left(-\frac{d}{d0} \right) \qquad (2.3)$$

Here, $d_0 = 0.962\,\text{nm}$ and $\alpha = 6.39$ are parameters of the distribution. The model first computes the Langevin approximation of the polydisperse ferrofluid

by a weighted superposition of Langevin functions

$$M_L(H) = \phi M_F \int\limits_0^\infty d^3 g_{d_0,\alpha}(d) L\left(\pi d^3 \frac{\mu_0 M_F H}{6kT}\right) \mathrm{d}d \cdot \left(\int\limits_0^\infty d^3 g_{d_0,\alpha}(d)\mathrm{d}d\right)^{-1},$$

$$(2.4)$$

where ϕ is the volume fraction of the magnetically active core of the particles and $M_F = 446\,\mathrm{kA/m}$ is the bulk magnetization of the magnetite particles, which has not been considered an adjustable parameter, but instead assumed to be constant. The interaction of the particles is then treated with a mean-field approach. Therefore, a mean field H_e is calculated next

$$H_e = H + \frac{1}{3}M_L(H) + \frac{1}{144}M_L(H)\frac{\partial M_L(H)}{\partial H} \qquad (2.5)$$

and eventually the magnetization

$$M(H) = M_L(H_e) \qquad (2.6)$$

Many theoretical models also require the tangent susceptibility $\chi_t = \frac{\partial M}{\partial H}$, which can be found by differentiating equation (2.6) with the chain rule

$$\frac{\partial M}{\partial H} = \left.\frac{\partial M_L}{\partial H}\right|_{H_e} \cdot \left(1 + \frac{1}{3}\left.\frac{\partial M_L}{\partial H}\right|_H + \frac{1}{144}\left[\left(\frac{\partial M_L}{\partial H}\right)^2 + M_L \frac{\partial^2 M_L}{\partial H^2}\right]_H\right). \qquad (2.7)$$

The solid line in figure 2.1 displays the best fit with that model. The saturation magnetization given in table 2.1 is extrapolated from there. This extrapolation indicates together with the manufacturer information $M_S \approx 26\,\mathrm{kA/m} \pm 10\,\%$, that this model is very well fitted to our dense ferrofluid (c.f. Ivanov *et al.* 2007).

2.3 Measurements of the surface pattern

We fill a cylindrical container, machined from aluminium, with the ferrofluid and expose it to a magnetic induction ranging from $B = 7.6\,\mathrm{mT}$ to $B = 37.7\,\mathrm{mT}$. The depth of the container amounts to 20 mm and the diameter is 29.7 mm. This diameter is chosen by trial such that only one single spike emerges in the centre of the vessel for all magnetic inductions we apply. From the weight
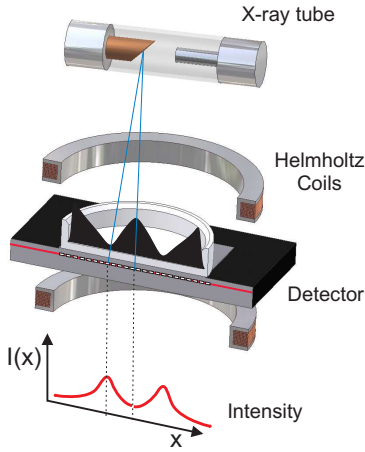
FIGURE 2.2: Sketch of the experimental setup (not to scale) for the X-ray method by Richter & Bläsing (2001)

of the filled container and the density, we calculate the amount of ferrofluid filled into the container to V_0 = 6.387 ml, which is equivalent to a filling height of D = 9.22 mm. Two complementary experimental methods were used to determine the height of the emerging spike in the centre of the vessel: the X-ray method by Richter & Bläsing (2001) and the laser method by Megalios *et al.* (2005), which are described in the following.

2.3.1 X-ray method

The X-ray apparatus comprises a stable X-ray point source, that emits radiation vertically from above through the fluid layer. The container is placed midway between a water cooled Helmholtz pair of coils, which generate a DC magnetic field of up to 40 mT. Directly below the container an X-ray camera with 512×512 pixels is located, which measures the transmitted intensity at every pixel in one plane underneath the fluid (Richter & Bläsing 2001). This setup is depicted in figure 2.2. The transmitted intensity of the X-rays is directly related to the height of the fluid above every corresponding pixel. To calibrate this relation, we use a wedge of known size, fill it with ferrofluid and place it in the empty container. In this calibration image, we therefore know the height of the fluid. Figure 2.3 shows the calibration data from the wedge. These are then fitted with
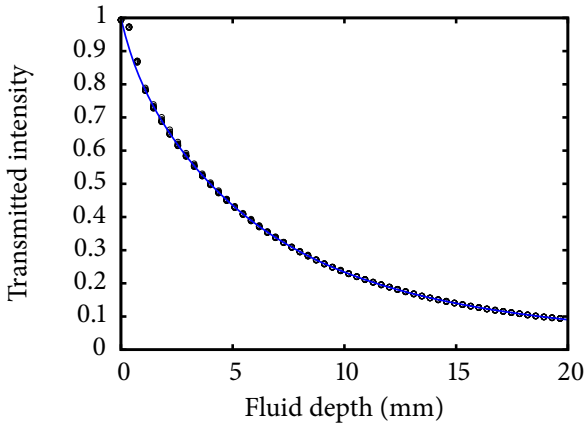
FIGURE 2.3: The transmitted intensity as a function of the fluid depth. The solid line is a fit with equation (2.8).
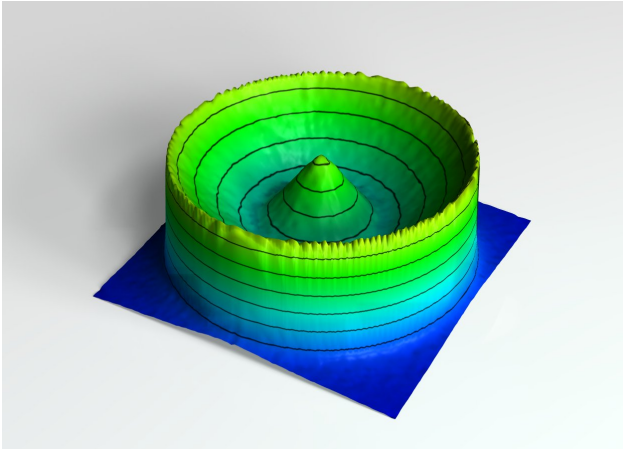
FIGURE 2.4: Three-dimensional reconstruction of the surface of the single spike at an induction of B = 22.69 mT. A related movie can be accessed at `http://stacks.iop.org/NJP/11/053016/mmedia`.

an overlay of three exponential functions

$$I(h) = I_0 \cdot \sum_{i=1}^{3} \alpha_i \exp(-\beta_i h) \tag{2.8}$$

as a practical approximation, denoted by the solid line in figure 2.3. Further details can be found in Gollwitzer *et al.* (2007).

After applying the inverse of (2.8) to an arbitrary image from the detector, we finally end up with a complete three-dimensional surface topography of the
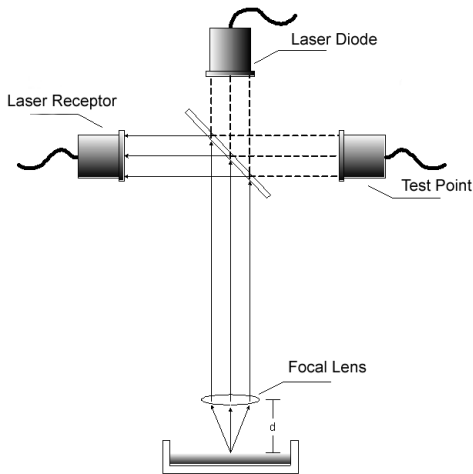
FIGURE 2.5: The experimental setup of the laser method by Megalios *et al.* (2005). The solid lines denote the path of the light reflected on the surface. The path sketched by the dashed lines is used to verify that the laser operates properly.

filled container. A reconstruction for one specific field is displayed in figure 2.4. A survey of the surface topography for different fields is provided by the related movie at `http://stacks.iop.org/NJP/11/053016/mmedia`.

2.3.2 Laser method

The laser method developed by Megalios *et al.* (2005) enables precise, relative measurements of the extrema of the surface topography. Figure 2.5 depicts the principle of operation. The container with the ferrofluid is situated in a long solenoid, which generates a vertical magnetic field. The solenoid is 33 cm long with an internal diameter of 13 cm and an external diameter of 14 cm. It has 1124 windings and produces up to 21 mT at its centre, with a variation of less than 1 % at the experimental region.

A laser beam is directed at the fluid surface through a semitransparent mirror, which splits the beam into two parts. One part is deflected sideways onto a test point and serves as an indicator, whether the laser operates correctly (the dashed path in figure 2.5). The other beam is focused on the fluid surface and the reflected light is deflected by the semitransparent mirror onto a photodiode detector (the solid path in figure 2.5).

The position of the focal spot can be adjusted by means of a micrometre
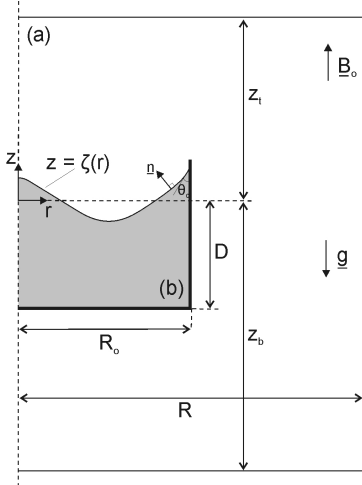
FIGURE 2.6: A small axisymmetric ferrofluid pool in the magnetic field.

screw. The maximum of the reflected intensity is reached, when the direction of the beam coincides with the normal vector of the surface at the focus spot and the distance of the lens from the surface is equal to the focal length. In normal operation, the beam is oriented vertically - thus the intensity of the signal reaches its maximum when the focus spot hits an extreme point of the surface, namely the top of a spike or the minimum in the centre of the meniscus. By tracing the maximum intensity of the reflected beam and recording the position of the laser optics, we get the position of the spike with micrometre resolution relative to some reference point. Also the absolute height of the spike above the bottom of the container can be determined by setting the reference point at the top of the container edge.

2.4 Governing equations and computational analysis

A scheme of a small cylindrical ferrofluid pool in a vertical magnetic field is shown in figure 2.6. The surrounding air and the embedded ferrofluid are denoted by (a) and (b), respectively. The applied field is uniform, i.e., of constant strength and vertical orientation, in a region far away from the pool. The field uniformity, however, is disturbed in the neighbourhood of the pool, due to the demagnetizing field of the pool itself. Therefore, the applied magnetic field

could be taken uniform only far away from the pool. In the following, the magnetic field distribution and the free surface deformation are taken as axially symmetric about the $r = 0$ axis (cf. figure 2.6).

The field distribution in regions (a) and (b) is governed by the equations of magnetostatics. The Gauss law for the magnetization reads

$$\nabla \cdot \boldsymbol{B} = 0, \tag{2.9}$$

where $\boldsymbol{B}$ is the magnetic induction. Since there are no free currents, the magnetic field $\boldsymbol{H}$ is irrotational and can be derived from a magnetostatic potential $\boldsymbol{H} \equiv \nabla u$ both inside and outside the ferrofluid and, provided that the materials are isotropic, it is parallel to $\boldsymbol{B}$ and so is the magnetization

$$\boldsymbol{B} = \mu \boldsymbol{H} = \mu_0 (\boldsymbol{H} + \boldsymbol{M}). \tag{2.10}$$

The magnetic permeability μ is constant in non-magnetic media, namely $\mu_a = \mu_0 = 4\pi \times 10^{-7} \mathrm{H/m}$; inside the ferrofluid, it depends on the field

$$\mu = 1 + \frac{M}{H}. \tag{2.11}$$

For the functional dependence $M(H)$, both constitutive equations which are discussed in section 2.2, are used. The first one comes from Langevin's theory for monodisperse colloidal suspensions (equation 2.1). The second one (equation 2.6) comes from the polydisperse model by Ivanov & Kuznetsova (2001) and assumes a gamma distribution of the particle diameters.

Writing equation (2.9) in terms of the magnetostatic potential, u, and taking into account the equation (2.10) yields

$$\nabla^2 u_a = 0, \quad \nabla \cdot (\mu \nabla u_b) = 0 \tag{2.12 a,b}$$

inside the non-magnetic phase (a) and inside the magnetic phase (b), respectively.

Equilibrium is governed by force balance along the ferrofluid free surface which is stated by the magnetically augmented Young-Laplace equation of

capillarity

$$-g\Delta\rho\zeta + \frac{1}{2}\mu_0 \int_0^{H_{bs}} M(H')\mathrm{d}H' + 2\aleph\sigma = K, \quad \text{at } z = \zeta(r), 0 \le r \le R_0 \quad (2.13)$$

where g is the gravitational acceleration, ρ is the density, σ is the surface tension and ζ is the vertical displacement of the free surface parametrized by the radial coordinate r, i.e., $\zeta = \zeta(r)$. The upper limit H_{bs} of the integral in the magnetization term is the field strength in the ferrofluid, evaluated at the free surface, i.e. at $z = \zeta(r)$.

The reference pressure K is constant at the free surface. The unit normal to the free surface $\boldsymbol{n}$ and the local mean curvature of the free surface $2\aleph$ are

$$\boldsymbol{n} = \frac{-\zeta_r\boldsymbol{e_r} + \boldsymbol{e_z}}{\sqrt{1 + \zeta_r^2}}, \quad 2\aleph = \frac{1}{r}\frac{\mathrm{d}}{\mathrm{d}r}\left(\frac{r\zeta_r}{\sqrt{1 + \zeta_r^2}}\right), \quad\quad\quad (2.14 \text{ a,b})$$

where $\boldsymbol{e_r}$ and $\boldsymbol{e_z}$ are mutually orthogonal unit vectors along the r- and z-axis, respectively, and $\zeta_r \equiv \mathrm{d}\zeta/\mathrm{d}r$.

The reference pressure K in equation (2.13) is determined by the constraint, that the ferrofluid volume is of fixed amount

$$2\pi \int_0^{R_0} \zeta r\mathrm{d}r = C = \text{const}, \quad\quad\quad (2.15)$$

i.e. we assume an incompressible liquid. The coordinate system, i.e. the location of the $z = 0$ line, is chosen such that $C = 0$.

The set of the governing equations (2.12 a,b), (2.13) and (2.15), needs to be solved for the magnetostatic potential $u_a(r, z)$ and $u_b(r, z)$, the free surface shape $\zeta(r)$ and the reference pressure K, taking into account the following boundary conditions (see also figure 2.6):

$$\frac{\partial u_a}{\partial r} = \frac{\partial u_b}{\partial r} = 0, \quad \zeta_r = 0 \text{ at } r = 0 \quad\quad\quad (2.16 \text{ a,b})$$

$$u_a = u_b, \quad \mu\boldsymbol{n} \cdot \nabla u_b = \mu_0 \boldsymbol{n} \cdot \nabla u_a \quad \text{at } z = \zeta(r) \text{ and } 0 \le r \le R_0 \tag{2.17a}$$

$$u_a = u_b, \quad \mu\frac{\partial u_b}{\partial r} = \mu_0\frac{\partial u_a}{\partial r} \quad \text{at } r = R_0 \text{ and } -D \le z \le \zeta(R_0) \tag{2.17b}$$

$$u_a = u_b, \quad \mu\frac{\partial u_b}{\partial z} = \mu_0\frac{\partial u_a}{\partial z} \quad \text{at } z = -D, 0 \le r \le R_0 \tag{2.17c}$$

$$u_a = 0 \text{ at } z = -z_b \tag{2.18}$$

$$\frac{\partial u_a}{\partial z} = \frac{B_0}{\mu_0} \text{ at } z = z_t, \quad \frac{\partial u_a}{\partial r} = 0 \text{ at } r = R \tag{2.19}$$

$$\zeta_r = \cot \alpha_c \text{ at } r = R_0. \tag{2.20}$$

The subscripts r and z denote differentiation with respect to r and z, respectively. Equations (2.16 a,b) are the conditions that the shape of the free surface and the magnetostatic potential are axially symmetric. Equations (2.17) are statements of the continuity of the potential and of the normal component of the magnetic induction across interfaces between two media with different magnetic permeabilities. In particular, it is by the equations (2.17b) that the fringing field is accounted for; this is due to the distortion of the magnetic field across the container walls, in the vicinity of the three-phase contact line, that is the liquid-air-solid junction. A datum for the potential is fixed by (2.18). Equations (2.19) are the conditions that the magnetic field be uniform far away from the pool. A contact angle α_c is prescribed by equation (2.20) and reflects the wetting properties of the magnetic liquid in contact with the solid wall of the container.

The governing equations give rise to a nonlinear, free boundary problem, owing to the presence of the free surface, the location of which enters the equations nonlinearly and is unknown a priori. An additional nonlinearity comes from the constitutive equation for the magnetization of the fluid. Such a problem is only amenable to computer-aided solution methods. The choice is the combination of Galerkin's method of weighted residuals and finite element basis functions (Kistler & Scriven 1983). Here we will only outline the appli-
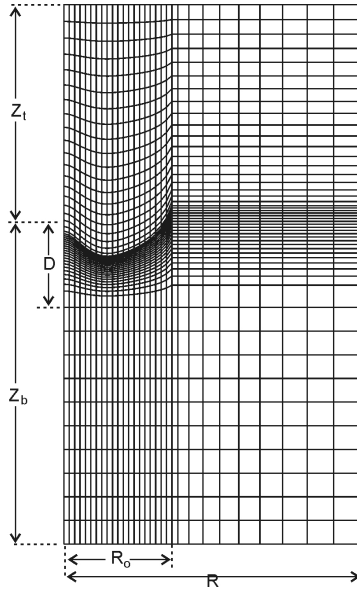
FIGURE 2.7: Sample of the discretized domain

cation of the method. Details can be found in previous works by Boudouvis *et al.* (1988) and Papathanasiou & Boudouvis (1998). The domain is tessellated into nine-node quadrilateral elements between vertical spines and transverse curves whose intersections with each spine are located at distances that are proportional to the displacement of the interface along that spine. The tessellation creates a mesh of nodes and at each node a finite element basis function is assigned that is unity at that node and zero at all other nodes. As the basis functions, we choose quadratic polynomials of the independent variables r and z. A sample of the computational mesh is shown in Figure 2.7. The dependent variables $u_a(r,z)$, $u_b(r,z)$ and $\zeta(r)$ are approximated in terms of a truncated set of the finite element basis functions. The governing equations are reduced with Galerkin's method to a set of nonlinear algebraic equations for the values of the unknowns u_a, u_b and ζ at the nodes and for the value of K.

At fixed values of the physical parameters, the nonlinear algebraic equation set is solved by Newton iteration. The parameter of interest here is the applied magnetic induction B_0, which appears in the boundary conditions (cf. equa-

tion 2.19a). Solution families, i.e., solutions at sequences of different values of B_0 are systematically traced with first-order continuation. The computational results reported are obtained with a mesh of 24000 nodes. The sensitivity of the spike height to further mesh refinement is practically negligible; namely, less than 0.2 % when doubling the mesh density. Three to five Newton steps are needed for the convergence at each value of the continuation parameter.

2.5 Comparison of experimental and numerical results

We record the surface profile for 200 different magnetic inductions $B_0 \in [7.6 \, \text{mT} \dots 37.7 \, \text{mT}]$ with the X-ray method described above. Inevitably, the magnetic induction in the neighbourhood of the container is distorted and strengthened in comparison to the induction for empty coils. The given values B_0 denote the spatially averaged magnetic induction below the container at a vertical distance of 23.8 mm from the bottom of the fluid layer. This corresponds to the boundary of the computational domain in the calculations. The height and position of the extreme point of the surface topography in the centre has been determined by fitting a paraboloid to a small circular region of the surface with a diameter of 1.5 mm. Figure 2.8 shows the resulting central height $\hat{h}(B_0)$. The red solid line marks the data for increasing induction. The magnetic fluid first rises at the edge of the container, thus the level of fluid in the centre of the vessel drops. The central height then corresponds to the minimum level in the centre. At a magnetic induction of around 16 mT, a single spike emerges in the centre that continues to rise for increasing induction. The central height then corresponds to the height of this spike. A small hysteresis is found when decreasing the field again. See the blue line in figure 2.8.

Using the laser method, we performed measurements of the spike height for 29 different magnetic inductions from 0 to 25.65 mT, which are also plotted in figure 2.8. By focusing the laser beam on top of the container edge, a reference point was taken to get absolute values for the central height $\hat{h}$ above the bottom of the container, denoted by the open squares. They differ from the X-ray measurement by a shift of 0.7 mm. However, if the reference point is adjusted by this shift, we find a nice coincidence of the data points from both methods, as shown by the open circles in figure 2.8.
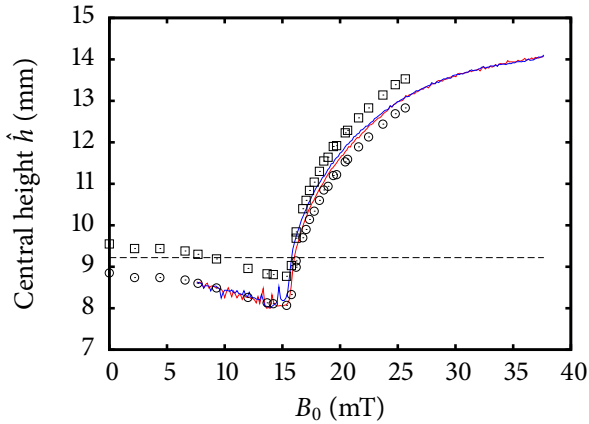
FIGURE 2.8: Height of the single spike or the minimum in the centre, respectively. The numbers given are the total absolute height of the fluid above the bottom of the container. For clarity, the individual 200 data points for one sweep are connected by a solid line. The red (blue) line denotes the values from the X-ray measurement for increasing (decreasing) field, respectively. The open squares show the results of the laser measurement. The open circles denote the laser data shifted on top of the X-ray data. The dashed line represents the filling level of the fluid according to the weight, neglecting the effects of the meniscus.

The inaccuracy of the reference point of the laser method can well be explained from the fact, that the laser beam cannot be focused precisely onto the top edge of the container. The vessel is machined from aluminium with a quite rough surface and diffuses the incident laser beam, which leads to the observed shift. This has been experimentally verified by comparing the height measurements of the bare aluminium and a ferrofluid surface at the same level. The difference in the reading is large enough to explain the shift between the laser data and the X-ray data. On the other hand, the accuracy of the reference point of the X-ray measurement depends on the positioning of the calibration wedge. The resolution of this position is limited by the lateral resolution of the detector, which leads to an estimate of the absolute error of 0.2 mm. Due to the roughness of the aluminium vessel, the X-ray data seem to be more precise than the laser data concerning the absolute height in the present experiment. Relatively, both yield practically the same result.

Further deviations may stem from the different ambient temperature at which
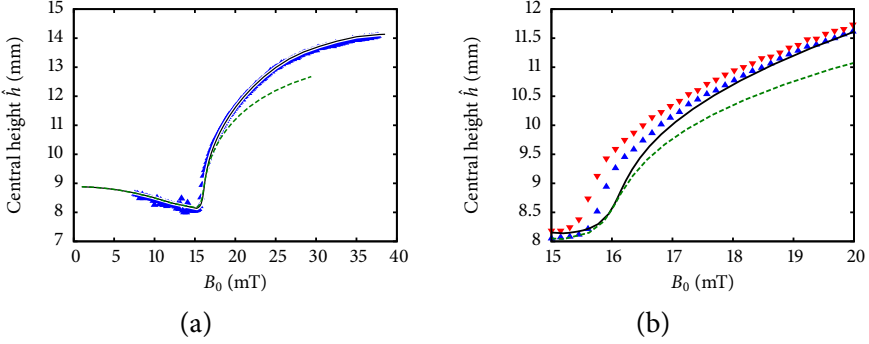
FIGURE 2.9: The central height $\hat{h}$ from the computations (lines) and from the X-ray experiment (triangles). Blue upward (red downward) triangles denote the values for increasing (decreasing) induction, respectively. The dashed green line is based on Langevin's law for the magnetization, while the black solid line employs the model by Ivanov & Kuznetsova (2001). (a) Full range (b) Zoom

the data were taken. Whereas in Bayreuth, the lab temperature was stabilized at $21 \pm 1\,^\circ\text{C}$, the temperature in Athens was $30\,^\circ\text{C}$. This leads to a reduced magnetization and may be the origin of a reduced spike height for higher fields (cf. figure 2.8).

After successfully comparing the results of the two measurement techniques, we now present the numerical predictions. The results of the computational analysis are depicted in figure 2.9 together with the X-ray data. The value corresponding to the central height $\hat{h}$ of the measurements is the height at the axis of symmetry $h|_{r=0} = \zeta|_{r=0} + D$, where D denotes the filling level. Two computational equilibrium paths are shown for two different models for the magnetization $M(H)$. The green dashed line displays the numerical result using Langevin's equation (2.1), while the black line makes use of the model by Ivanov & Kuznetsova (2001). For magnetic inductions up to 17 mT there is only a small difference between both results. This is explained by the similarity of both magnetization laws up to an internal field of $H \approx 10\,\text{kA/m}$, as shown in figure 2.1. For higher fields, however, Langevin's law is no longer a valid approximation. This leads to a rather big deviation between both theoretical curves. Regardless of the underlying magnetization curve, the numerical solutions show a continuous behaviour of $\hat{h}$ in the full range of B_0. In particular,

no turning points are traced on the curve. This is mentioned, since a pair of turning points, if existed, should imply a hysteresis in surface deformation observed when increasing and then decreasing B_0. Thus, from the theoretical calculations we do not expect any hysteresis. We stress this fact, because in the case of an infinitely extended container, a hysteresis is both expected theoretically (cf. Friedrichs & Engel 2001, e.g.) and found in the experiment and numerical calculations (cf. Gollwitzer *et al.* 2007, e.g.). Moreover, we tested the influence of the contact angle. A computation for $\alpha_c = 20\,^\circ$ does not deviate more than 60 μm from the above calculation over the full range of B. Thus, the spike height does only weakly depend on the contact angle.

Next, we compare the measurements with the numerical results. In the full range, the experimental data agree with the more advanced computations taking into account the magnetization law by Ivanov & Kuznetsova (2001). The difference is within only 1 % of the absolute height, except near the threshold, where it amounts to 6 %. This is natural for a sigmoidal function, where close to the steep increase the error can become arbitrarily large, when there are uncertainties of the control parameter. The difference between the thresholds in theory and experiment amounts to at most 3 % as can be seen from Figure 2.9 (b). It shows an enlarged view of $\hat{h}$ in the immediate vicinity of the threshold. In opposite to the numerical results, we observe in the experiment a small hysteresis between the data for increasing B_0, as marked by upwards triangles, and the one for decreasing B_0, denoted by downward triangles. The hysteresis is in the range of $\Delta B_0 = 0.2\,\text{mT}$. The origin for this hysteresis is a priori not clear.

Note, that Gollwitzer *et al.* (2007) measure a hysteresis of $\Delta B^\infty = 0.17\,\text{mT}$ for the same ferrofluid as in our case in a container with a diameter of $\approx 10 \times \lambda_c$. Remarkably, this value is in the same range as the one observed above. If the hysteresis in our experiment would be of the same nature, it should be much smaller due to the imperfection caused by the container edge (Cross & Hohenberg 1993). Therefore we suspect another mechanism. One candidate is a hysteretic wetting of the cylindrical wall. The difference between the advancing and the receding contact angle can be as large as 10 ° for a surface that has not been specially prepared (de Gennes 1985; Dussan 1979). Moving the contact line always costs energy. This may explain the small hysteresis of the spike height for increasing and decreasing induction. In our experiment, this effect is important, because the interfacial area between the fluid and the vertical wall
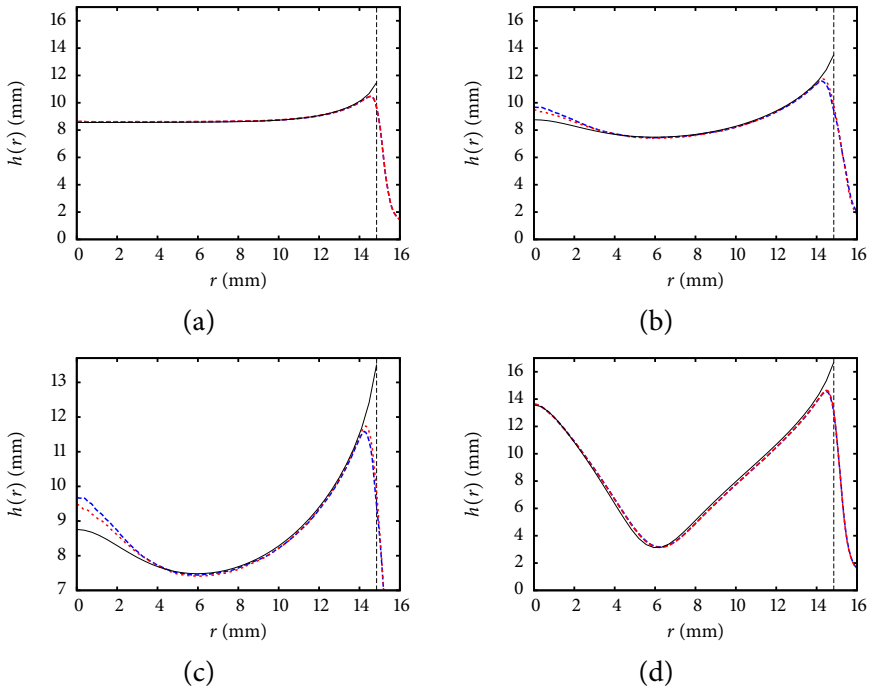
FIGURE 2.10: The ferrofluid free surface shapes at various magnetic field strengths. The solid lines show the numerically computed profiles, while the red (blue) dashed line gives radial interpolation of the experimental data for increasing (decreasing) magnetic induction. The vertical dashed line shows the side wall of the container. (a) B = 7.39 mT, (b) B = 16.17 mT, (c) Zoom of (b), (d) B = 29.70 mT

is comparable to the free surface of the fluid.

The availability of the complete surface topography from the X-ray method allows us not only to compare the central height, but also the shape of the spike or meniscus, respectively. Examples for the free surface shapes at selected values of the magnetic induction are shown in figure 2.10. The experimental data have been averaged angularly around the centre of the observed spike, which is not exactly in the centre of the container in the experiment. This off-centre distance is rather small (0.05 mm), however it must be taken into account, otherwise the averaging would disturb the shape of the spike.

Similarly to the comparison of the height alone, there are only slight differences between the computations and the experimentally observed shape. Most notably, we discern a drop at the edge of the container. The reason for this difference is two-fold: first, the angular average does not work well near the container border, because the centre of the spike is off-axis, as explained before. Second, the X-ray method has problems to accurately detect the height near the border, where the container wall shadows the X-rays. Further, for magnetic inductions near the threshold (cf. figure 2.10 b and c), the height of the tip differs by $\approx 1\,\text{mm}$. The reason is probably a slight shift of the critical induction (cf. figure 2.9), where the height is very sensitive to small changes of the induction B.

The hysteresis, already observed from the central height alone, manifests itself by a difference of the surface profiles for increasing and decreasing induction. Far away from the threshold, both profiles match nearly perfectly (figure 2.10 a and d), while there is a clear difference near the threshold (figure 2.10 b and c). The tip of the spike is considerably smaller for an increasing magnetic induction, while the level of the fluid near the container edge is higher. This corroborates a hysteretic wetting to be responsible for the hysteresis.

Apart from these differences, the deviation between the computed and measured profiles is around $1\,\%$.

2.6 Discussion and Conclusion

We have reduced the container size for the Rosensweig instability until only a single spike of ferrofluid remains. Whereas for our fluid, the extended system exhibits a transcritical bifurcation to hexagons, here an imperfect bifurcation sets in, and the axisymmetric free surface deformation evolves supercritically and monotonically. This is at least the outcome of the monolithic finite element approach, which takes into account the side-wall effects, namely the wetting and the fringing field, as well as the polydispersity of the fluid. We find a convincing agreement between theory and two independent measurement techniques, the errors being within $3\,\%$ without any adjustable parameter. The nonetheless observed hysteresis is due to the wetting.

Our findings immediately raise the issue of what is "in between", regarding the structure of the solution space – that is surface deformation versus applied

field and other key parameters – as the size of the pool grows laterally. This will be tackled in a forthcoming publication by Spyropoulos *et al.* (2010).

A transition from a transcritical backward to an imperfect forward bifurcation under spatial constraints has also been reported by Peter *et al.* (2005). Their spatial stripe forcing simultaneously breaks the rotational and translational symmetry. In our case it is sufficient to break the translational symmetry.

To conclude, we have quantitatively compared numerics and experiments of the Rosensweig instability in a system of finite size. This is a specific example, how external constraints may change a perfect transcritical bifurcation to an imperfect supercritical one.

3 Dynamics of the Rosensweig instability

In this chapter, we describe a method to reconstruct an amplitude equation for the Rosensweig instability from experimentally measured data. A flat layer of a ferrofluid is thermostated at 10 °C. At this temperature, the liquid has a relatively high viscosity of 4.48 Pa s, approximately 60× larger than for the ferrofluid used in chapter 2. Consequently, the dynamics of the formation of the Rosensweig pattern becomes very slow.

By sudden switching of the magnetic induction with a specialized measurement protocol, the system is pushed to an arbitrary point in the phase space spanned by the pattern amplitude and the magnetic induction. Afterwards, it is allowed to relax to its equilibrium point. From the dynamics of this relaxation, we find the linear growth rate and reconstruct the fully nonlinear amplitude equation, which describes the system. The linear growth rate is compared to theoretical predictions by Knieling *et al.* (2007) and the nonlinear dynamics is compared with standard amplitude equations.

When the system is placed into the neighbourhood of an unstable equilibrium point on the subcritical branch, stable localized patterns develop like the ones reported previously by Richter & Barashenkov (2005).

3.1 Introduction

When Aristotle (350 B.C.) described the motion of falling bodies, he incorrectly claimed that the velocity is constant and proportional to the mass of the body, because he did not know the concept of inertia. He has been later proven wrong by Galileo and Newton, who linked forces with acceleration. Aristotles' idea of motion, however, is a valid approximation in many cases, when a viscous fluid is involved and either the typical dimension d and the velocity v are small, or the kinematic viscosity v is high. In this limiting case of small Reynolds numbers

$Re = vd/v \ll 1$, the viscous forces outweigh inertia, and body and fluid motion is determined entirely by drag forces. The velocity is then directly proportional to the force acting on a fluid volume or the particle inside a viscous fluid (Kohr & Pop 2004). The Navier–Stokes equation in this limit reduces to just $\nabla p = \eta \Delta \boldsymbol{v}$, where p is the pressure and η the viscosity. The reduced equation does not directly depend on the time t any more. This leads to a qualitatively different behaviour, than what we experience in our daily life. For example, the flow of a fluid with high viscosity can be completely reversed by reversing the direction of motion. Heller (1960) demonstrates, that a droplet of ink inside a viscous liquid between two concentric cylinders can be deformed to several 100 % of its initial size, apparently mixing the ink with the surrounding fluid. After reversing the motion, the droplet is recovered almost perfectly. Consequently, mixing two jets of different fluids becomes increasingly difficult, when the Reynolds number is reduced, as for example in microfluidics applications (Johnson *et al.* 2002). Another example for motion at low Reynolds numbers $Re \approx 10^{-5}$ is the self propulsion of biological microorganisms like bacteria or swimming spermatozoa. Purcell (1977) formulates the conditions for the self propulsion in this case in his famous "scallop theorem". At this small scale, the motion of a swimmer is very different from macroscopic swimmers due to missing inertia.

In the case of the Rosensweig instability with a ferrofluid, the viscosity of the liquid and therefore the Reynolds number also play a role for the dynamics of the pattern formation. For an inviscid fluid ($\eta = 0$) and an infinitely deep container, Cowley & Rosensweig (1967) provide a linear stability analysis already in the very first description of the normal field instability to find the critical threshold B_c and the critical wavenumber k_c. Such a linear stability analysis approximates the dynamics of the pattern formation by an equation of motion for the amplitude A in the vicinity of the threshold induction and for very small amplitudes

$$\frac{\partial A}{\partial t} = w(B)A, \tag{3.1}$$

where $w(B)$ is the linear growth rate. This approach has been later extended by Salin (1993) to fluids with a finite viscosity, where the growth rate $w(B)$ depends on η, and to a finite depth of the container by Weilepp & Brand (1996). First experimental investigations on the growth of the pattern are provided by Lange *et al.* (2000, 2001), who also derive the growth rate for the case of

a viscous magnetic fluid and an arbitrary layer thickness D. This theoretical analysis has been later extended to the case of a nonlinear magnetization curve $M(H)$ by Knieling *et al.* (2007).

The nonlinear aspects of the dynamics have posed more difficulties to the theoretical analysis. To derive nonlinear amplitude equations, the adjoint operator of the system is needed, but very difficult to obtain (Lange 2002*a*). Only recently, Bohlius *et al.* (2007) successfully formulated the adjoint system and consequently tackled the issue of systematically deriving nonlinear amplitude equations (Bohlius *et al.* 2008). However, in-depth experimental investigations in this area are still missing. Knieling *et al.* (2007) focus more on the linear aspects of the pattern formation. The experiments and the numerical simulations they provide show also the nonlinear dynamics, but this depends heavily on the initial conditions and is therefore difficult to interpret quantitatively. Qualitatively, they observe the nonlinear growth of the pattern on the surface of two different magnetic fluids, the viscosities of which differ by a factor of ten. They find an oscillatory relaxation of the amplitude A of the pattern to its final value A_{fin}, when the magnetic induction B is suddenly switched to an overcritical value. These oscillations are prominent for the less viscous fluid, but decay rapidly for the more viscous liquid, where the Reynolds number is approximately $Re \approx 3$.

The key idea in this chapter now is to use a fluid with a very high viscosity to study the pattern formation of the Rosensweig instability. Consequently, the Reynolds number is very small $Re \approx 10^{-3}$, and the relaxation is monotonic and slow. Due to the long time scales, the growth of the pattern can be measured in the extended system using a two-dimensional X-ray imaging technique (Richter & Bläsing 2001; Gollwitzer *et al.* 2007), which provides the full surface topography, as opposed to the one-dimensional line cut, which has been observed by Knieling *et al.* (2007).

The heavily overdamped system not only gives access to the linear growth rate, but also the nonlinear dynamics can be studied quantitatively. Due to the strong damping, the dynamics of the pattern amplitude follows a first order equation of motion even in the nonlinear regime

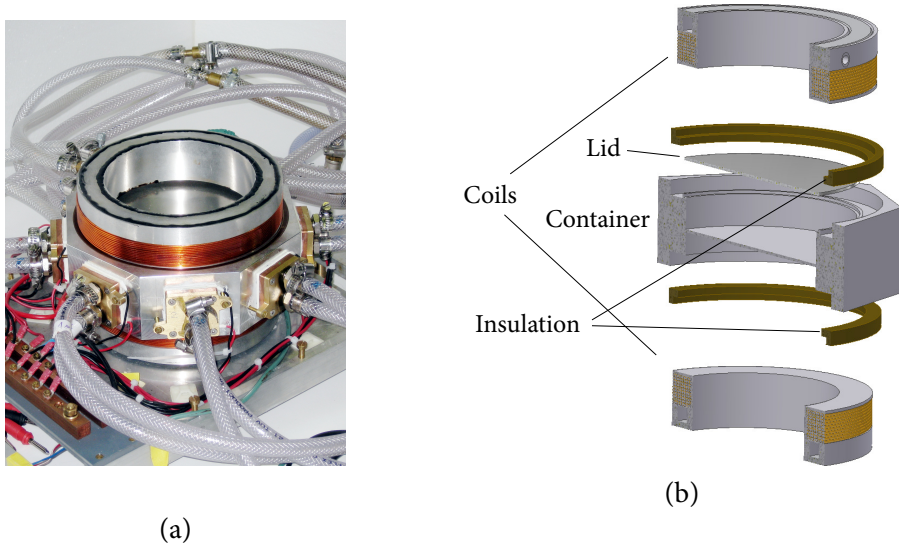$$\frac{\partial A}{\partial t} = f(B, A). \tag{3.2}$$

FIGURE 3.1: Setup of the apparatus for dynamic measurements of the Rosensweig instability (without the X-ray source and detector). (a) Photograph of the assembled container (b) Exploded view.

Here f is an analytic function, which does not directly depend on the time t. Up to a friction coefficient, f can be seen as a force field which acts on the system. From the experimental data, f can be reconstructed and compared directly to the theoretical amplitude equations.

In the next section, we describe the experimental setup and the magnetic fluid we use. Next, the measurement protocol and the data analysis are described. Then the experimental data are compared to theoretical models, and finally the results are discussed.

3.2 Experimental setup

The experimental setup consists of the X-ray apparatus described in section 2.3.1 to measure the surface deflections of the magnetic fluid. In contrast to the experiment in chapter 2, we now use another magnet and a different container for the ferrofluid, which are shown in figure 3.1.

Quantity		Value	Error
Surface tension	σ	30.9	$\pm 5\,\mathrm{mN\,m^{-1}}$
Density	ρ	1168	$\pm 1\,\mathrm{kg\,m^{-3}}$
Viscosity at 10 °C	η	4.48	$\pm 0.1\,\mathrm{Pa\,s}$
Saturation magnetization	M_S	26.6	$\pm 0.8\,\mathrm{kA\,m^{-1}}$
Initial susceptibility at 10 °C	χ_0	3.74	± 0.005
Exponent of the Γ-distribution	α	3.8	± 1
Typical diameter	d_0	1.7	$\pm 0.2\,\mathrm{nm}$
Volume fraction	ϕ	5.96	$\pm 0.2\,\%$

TABLE 3.1: Material properties of the ferrofluid APG E32 (Lot G090707A) from Ferrotec Co.

The container is a regular octagon machined from aluminium with a side length of 77 mm and two concentric inner bores with a diameter of 140 mm. These circular holes are carved from above and below, leaving only a thin base in the middle of the vessel with a thickness of 2 mm. On top of the octagon, a circular lid is placed, which closes the hole from above (see figure 3.1 b). Each side of the octagon is equipped with a thermoelectric element QC-127-1.4-8.5MS from Quick-Ohm. These are powered by a 1.2 kW Kepco KLP-20-120 power supply. The hot side of the Peltier elements is connected to water cooled heat exchangers. The temperature is measured at the bottom of the aluminium container with a Pt100 resistor. A closed loop control, realized using a computer and programmable interface devices, holds the temperature θ of the vessel constant with an accuracy of 10 mK.

The container is surrounded by a pair of Helmholtz coils, thermally isolated from the vessel with a ring made from FR-2. The size of the coils is adapted to the size of the vessel in order to introduce a magnetic ramp, a technique introduced by Richter & Barashenkov (2005). With these coils, the magnetic field strength falls off towards the border of the vessel, where it reaches 80 % of its value in the centre.

We use the commercial ferrofluid APG E32 from Ferrotec Co, the basic material parameters of which are listed in table 3.1. The viscosity η deserves a special attention for the experiments of this chapter, as it influences the time scale of the pattern formation. It has been measured in a temperature range
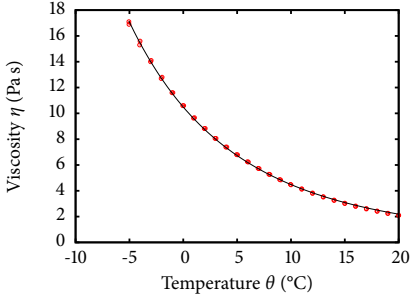
FIGURE 3.2: The dynamic viscosity η of the ferrofluid APG E32 versus the temperature θ. The symbols represent measurements, and the solid line is an approximation by equation (3.3).
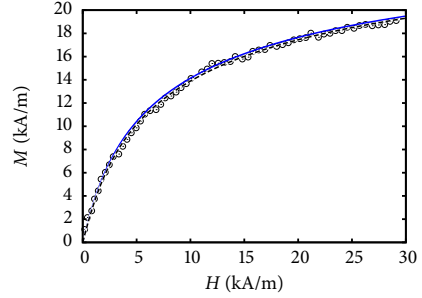
FIGURE 3.3: Magnetization curve of the ferrofluid APG E32. The symbols show the measured data at $\theta = 20\,°C$. The black dashed line is a fit with the model by Ivanov & Kuznetsova (2001). The blue solid line shows an evaluation of the model at $\theta = 10\,°C$.

of $-5\,°C \leq \theta \leq 20\,°C$ using a commercial rheometer (MCR 301, Anton Paar) in cone and plate geometry (figure 3.2). At room temperature, the ferrofluid we use is 2000 times more viscous than water with a viscosity $\eta = 2\,Pa\,s$. This value can be increased by factor of 9 when the liquid is cooled to $-5\,°C$. The data from figure 3.2 can be very well fitted with the well-known Vogel-Fulcher law (Rault 2000)

$$\eta = \eta_0 \exp\left(\frac{\psi}{\theta - \theta_0}\right), \tag{3.3}$$

with $\eta_0 = 0.48\,mPa\,s$, $\psi = 1074\,K$, and $\theta_0 = -107.5\,°C$ (the dashed line in figure 3.2). This means, that the viscosity can easily be adjusted in a wide range by controlling the temperature. For the present measurements, we chose a temperature of $\theta = 10\,°C$, where the viscosity amounts to $\eta = 4.48\,Pa\,s$ according to equation (3.3).

The magnetization curve has been determined using the fluxmetric magnetometer described in section 2.2 (see figure 3.3) at a temperature $\theta = 20\,°C$. For a comparison with the pattern formation experiments, this curve must be extrapolated to $\theta = 10\,°C$, which is done using the model by Ivanov & Kuznetsova (2001) (equation 2.6).
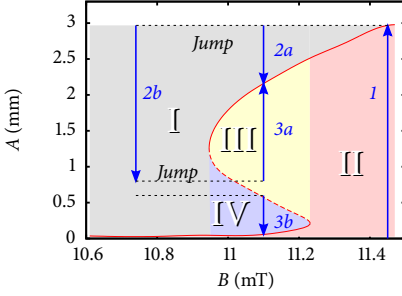
FIGURE 3.4: The multistep measurement protocol for the relaxation measurements. Dotted lines indicate jumps of the magnetic inductions. Blue arrows denote the path of the system during the relaxation phases.

More problematic is the measurement of the surface tension. We measure the surface tension using a commercial ring tensiometer (LAUDA TE 1) and a pendant drop method (Datayphysics OCA 20). Both methods result in a surface tension of $\sigma = 31 \pm 0.5$ mN/m, but when the liquid is allowed to rest for one day, σ drops down to 25 ± 0.5 mN/m. This effect, which is not observed in similar magnetic liquids like the one used in chapter 2, gives a hint that our liquid is chemically less stable in the sense that the surfactants change the surface tension on a longer time scale, when the surface is changed. Since the pattern formation experiments do change the surface during the measurements, the uncertainty of the surface tension is ≈ 5 mN/m, as given in table 3.1.

3.3 Measurement protocol

Figure 3.4 displays the measurement protocol on the basis of the bifurcation diagram. The static amplitude of the pattern of the Rosensweig instability for our fluid is indicated by the red line. When the system is set onto an arbitrary initial point (B_{ini}, A_{ini}) in this diagram, and the magnetic induction B is kept constant, the amplitude A monotonically increases or decreases, until the system reaches the stable equilibrium (solid red line). The direction of the change of A depends on the region, where (B_{ini}, A_{ini}) is situated – in the regions II and III in figure 3.4, A increases, and in regions I and IV, the amplitude decreases with time.

In order to push the system to an arbitrary location (B_{ini}, A_{ini}), a multistep measurement protocol is employed. The first step (path *1*) is always a relaxation of the pattern at the overcritical induction $B_{high} = 11.45$ mT for 1 min, to reach

the final amplitude at that point A_{high} = 2.98 mm. To get to an arbitrary point in the region I in diagram 3.4, a second step is needed. When the system is settled at (B_{high}, A_{high}), the magnetic induction is quickly changed to the desired value B_0, and the resulting dynamics is observed (path *2a*), until the desired amplitude A_0 is reached. To get into the regions III or IV, three steps are needed in total – coming from (B_{high}, A_{high}), the second step (path *2b*) is a decay of the pattern amplitude at the undercritical induction B_{low} = 10.74 mT, until the intended amplitude A_{ini} is reached. The induction is then quickly raised to the desired B_{ini}. The system then follows the path *3a* or *3b* in region III or IV, respectively.

When the desired initial amplitude A_{ini} is zero, for example when the growth of the pattern in region II shall be observed, we also apply the three step protocol with the detour by paths *1* and *2b*. At this point, the pattern decays until the amplitude is very small (A_{ini} = 0.05 mm). After that, the induction is raised to $B = B_{ini}$. We use this procedure instead of directly switching the magnetic induction from zero to $B = B_{ini}$ in order to establish the exact same pattern in all regions. Coming from a perfectly flat surface, the pattern has some additional degrees of freedom manifesting in point defects or different orientations of the wave vectors. When we take the detour by the paths *1* and *2b*, we seed the wave vectors of the pattern at (B_{high}, A_{high}), and the final pattern developed is likely to be the same.

We explored all regions in figure 3.4 in several rounds. In the first round, we examined region I by starting from $A_{ini} = A_{high}$ and 65 different inductions in the range 10.61 mT $\leq B \leq$ 11.46 mT. The decay of the pattern was observed until it reaches the stable solution or zero. The second round was devoted to region II. We used the three step procedure to observe the growth of the pattern from a very small amplitude up to the stable solution for 21 different inductions in the range 11.19 mT $\leq B \leq$ 11.46 mT. The third to sixth rounds covered the regions III and IV. Starting from four different amplitudes, we observed the evolution of the pattern in the range of 10.89 mT $\leq B \leq$ 11.27 mT. At each round, we recorded the complete evolution of the surface topography of the ferrofluid during the last step with the fastest possible frame rate (7.5 Hz) of the X-ray method (see chapter 2.3.1), in total taking about 170 000 frames.
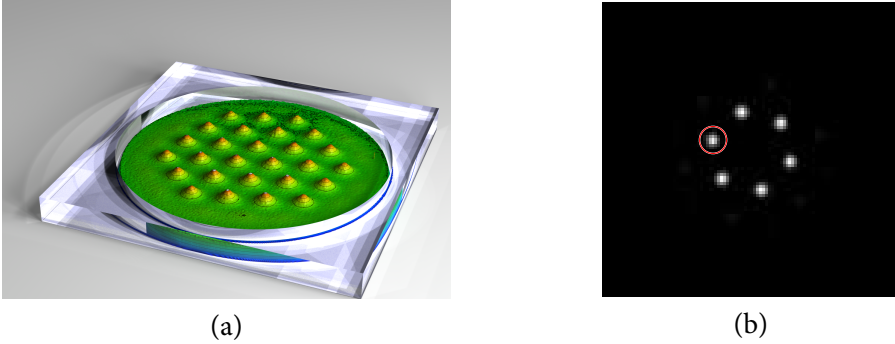
(a)

(b)

FIGURE 3.5: The final pattern at B = 11.45 mT. The black contour lines in the reconstruction of the surface (a) are 1 mm apart. The amplitude is determined from the corresponding power spectrum (b) by the total power in the encircled mode.

3.4 Image processing

After processing the image data, we finally arrive at the surface topography map for every frame. Figure 3.5 (a) shows a reconstruction of the surface at $B = B_{\text{high}}$. A description of the technical details of this process can be found in the paper by Gollwitzer *et al.* (2007). The amplitude of the pattern, A, is then determined in Fourier space (figure 3.5 a). We use a circularly symmetric Hamming window with the weight function

$$w(x, y) = \begin{cases} \left(0.54 + 0.46 \cos\left(\frac{\pi\sqrt{x^2+y^2}}{b}\right)\right)^2 & x^2 + y^2 \leq b^2 \\ 0 & \text{else} \end{cases} \tag{3.4}$$

for apodization (Gollwitzer *et al.* 2006) with a radius b = 46 mm. The total power in one of the modes (marked with a red circle in figure 3.5 b) is used to compute the amplitude of the pattern

$$A = N \cdot \sqrt{\sum_j \left|c_j\right|^2}, \tag{3.5}$$

where c_j are the Fourier coefficients inside the circle. In order to get a meaningful estimate, the normalization factor N is chosen such that A is the height
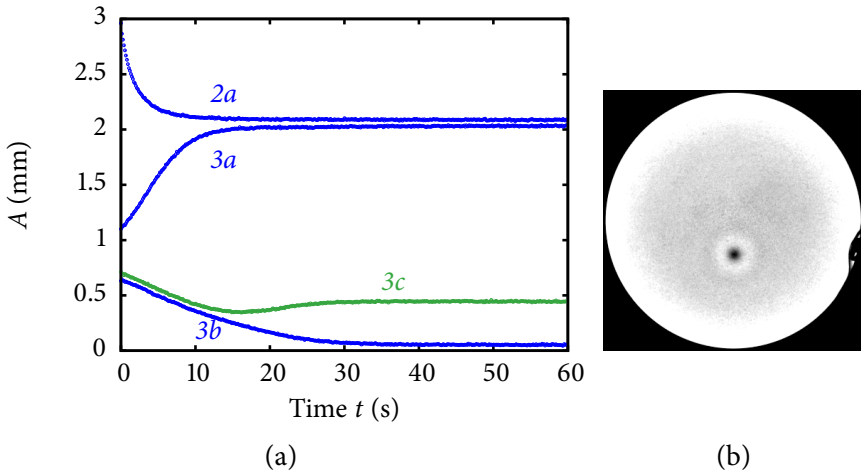
(a)   (b)

FIGURE 3.6: The evolution of the pattern amplitude at an induction $B = 11.06$ mT, starting from different amplitudes (a). The labels of the datasets correspond to the paths in figure 3.4. The path *3c* ends in a localized state with only one spike (X-ray image shown in b), and has been removed from the data.

difference between maxima and minima, when the input is a perfectly sinusoidal hexagonal pattern.

Figure 3.6 (a) displays the resulting amplitude versus time for the paths labelled *2a*, *3a* and *3b* in figure 3.4. As expected from the bifurcation diagram, the amplitudes for paths *2a* and *3b* decrease monotonically, and the stable solution is approached in an asymptotic fashion. Similarly, *3a* increases monotonically and asymptotically converges to the patterned state. There is, however, a small glitch. The bifurcation diagram 3.4 provides only a single solution for the patterned state, but the asymptotic amplitudes of the paths *2a* and *3a* differ by 2.6 %. A further path, *3c*, which starts very close from the initial amplitude of the path *3b*, ends in a finite intermediate amplitude. The reason is, that the final pattern is different, in spite of the aforementioned efforts – path *2a* ends in a pattern with 20 spikes, whereas the final pattern of path *3a* contains only 11 spikes. These additional spikes are situated near the border of the window function and therefore contribute only little to the overall amplitude. Path *3c* finally ends in a localized solution with only one single spike, depicted in
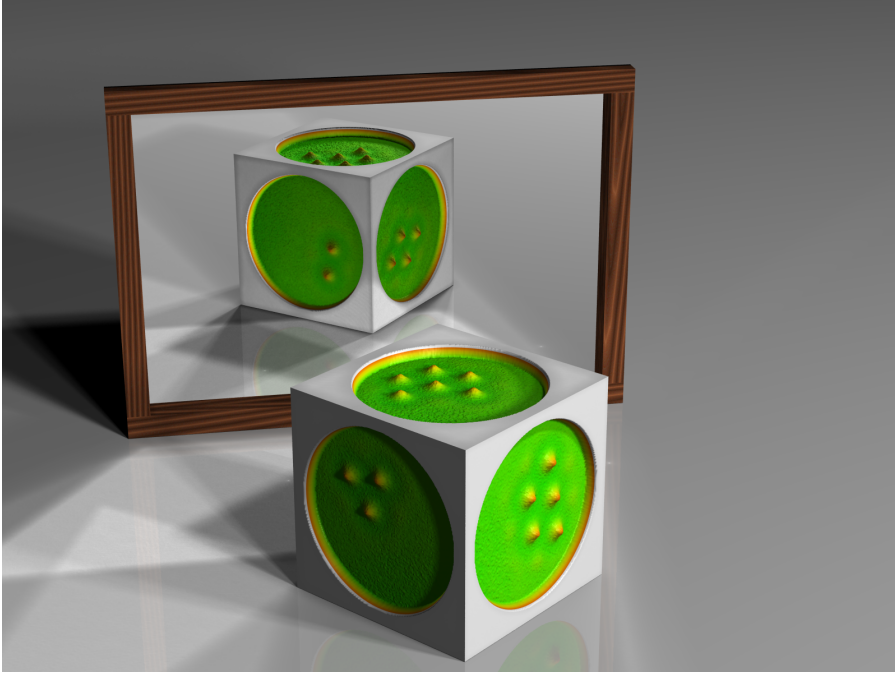
FIGURE 3.7: Artwork about localized patterns. A rendering containing hexagonal patches of two to six spikes on the faces of a dice. All patterns show the symmetry of the underlying hexagonal structure of the fully developed pattern.

figure 3.6 (b).

We are currently unable to control this additional degree of freedom for the system. In the following, the datasets with a reduced number of spikes have not been treated in a special way. Only when the final pattern does not fill the full width at half maximum of the window function, that is for less than 10 spikes, the estimated amplitude would be more than 9 % too small for the given window function. These datasets have been sorted out.

Out of 205 datasets, 32 have been rejected, the final pattern of which consists of only a small number of spikes. Any pattern from a single spike up to a cluster of 9 has been found. An artistic rendering of some of those patterns is shown in figure 3.7. These patterns occur only in the bistable regime (region III and IV) and have been previously observed by Richter & Barashenkov (2005). In
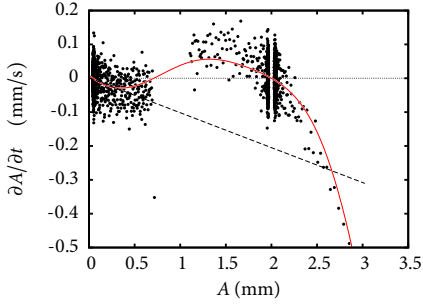
FIGURE 3.8: Reconstruction of the amplitude equation at an induction $B = 11.05\,\text{mT}$. The symbols are central differences from equation (3.6). The red line serves as a guide to the eye. The dashed line is a linear fit to the range $A < 0.37\,\text{mm}$.

their experiment, they have been initiated by a localized disturbance. In the present experiment, these patterns predominantly emerge from a starting point $(B_{\text{ini}}, A_{\text{ini}})$ near the unstable solution branch. In this study, however, we focus only on the fully developed pattern.

3.5 Results

3.5.1 Recovery of the amplitude equation

In the following, we will describe a method to derive the amplitude equation from the data. So far, we have measured the evolution of the amplitude $A(t)$ for different values of the induction B and a set of initial amplitudes A_{ini}. Suppose, that the system can indeed be described by an amplitude equation of the form (3.2). Then $A(t)$ is the solution of this equation for different initial conditions $(B_{\text{ini}}, A_{\text{ini}})$, and we want to get the function $f(A, B)$ on the right hand side of (3.2). Because this function should not be dependent on time, the time derivative $\dot{A} = \partial A / \partial t$ of our measured $A(t)$ directly gives a value of this function at the corresponding amplitude. We therefore plot $\dot{A}$ as a function of A in figure 3.8 for one selected induction in the bistable region. The time derivative has been estimated from the measured data by central differences (Abramowitz

& Stegun 1965, §25.1.2)

$$\frac{\partial A}{\partial t}\bigg|_{n+\frac{1}{2}} \approx \frac{A_{n+1} - A_n}{\Delta t}$$

$$A\big|_{n+\frac{1}{2}} \approx \frac{A_{n+1} + A_n}{2}, \tag{3.6}$$

where $\Delta t = 0.134\,\mathrm{ms}$ is the time between consecutive frames, and A_i denotes the pattern amplitude of the ith frame. Because these differences suffer heavily from noise, we also plot the radial basis function approximation explained later in section 3.5.3 as a guide to the eye (red line in figure 3.8). In the bistable regime, the amplitude equation has three roots, corresponding to one unstable and two stable solutions. In the diagram 3.8, the stable and unstable solutions are characterized by zero-crossings with a negative or positive slope, respectively. These slopes correspond to the linear growth rate of the pattern amplitude and will be compared to theoretical predictions in the next section.

3.5.2 The linear growth rate

According to the linear stability analysis by Lange *et al.* (2001), the pattern amplitude can be described by an exponential growth, when A is small

$$A \sim \exp\left(-i\tilde{\omega}t\right) \tag{3.7}$$

$$\tilde{\omega} = \omega_1 + i\omega_2 \tag{3.8}$$

The exponent $\tilde{\omega}$ follows from the dispersion relation given by Knieling *et al.* (2007) for a layer of ferrofluid with the finite depth h, a nonlinear magnetization

curve $M(H)$, the surface tension σ, the density ρ, and the kinematic viscosity ν

$$
\begin{aligned}
0 = \frac{\nu^2}{\tilde{k}\coth(\tilde{k}h) - k\coth(kh)} &\left(\tilde{k}\left[4k^4 + (k^2 + \tilde{k}^2)^2\right] \right. \\
&\times \coth(\tilde{k}h) - k\left[4k^2\tilde{k}^2 + (k^2 + \tilde{k}^2)^2\right]\tanh(kh) \\
&- \frac{4k^2\tilde{k}(k^2 + \tilde{k}^2)}{\cosh(kh)\sinh(\tilde{k}h)} \right) + \tanh(kh)\left(gk + \frac{\sigma}{\rho}k^3 \right. \\
&\left. - \frac{\mu_0(1 + \bar{\chi})M^2}{\rho}\Lambda(kh)\,k^2 \right),
\end{aligned}
\tag{3.9}
$$

where

$$
\Lambda(kh) = \frac{e^{kh(1+\bar{\chi})/(1+\chi_t)}(2 + \bar{\chi}) - \bar{\chi}e^{-kh(1+\bar{\chi})/(1+\chi_t)}}{e^{kh(1+\bar{\chi})/(1+\chi_t)}(2 + \bar{\chi})^2 - \bar{\chi}^2 e^{-kh(1+\bar{\chi})/(1+\chi_t)}}
\tag{3.10}
$$

$$
\tilde{k} = \sqrt{k^2 - \frac{i\tilde{\omega}}{nu}}.
\tag{3.11}
$$

The susceptibility $\bar{\chi}$ is defined by a geometric mean $1 + \bar{\chi} = \sqrt{(1 + \chi_t)(1 + \chi_{ch})}$, with the tangent susceptibility $\chi_t = \partial M/\partial H$ and the chord susceptibility $\chi_{ch} = M/H$. It can be evaluated for any field H, when the magnetization curve is known.

Lange (2003) revises the solutions for the dispersion relation in case of a linear magnetization curve. The solution space is rather complex, but the following conclusions can be drawn: for an overcritical magnetic induction $B > B_c$ and $k = k_c$, $\tilde{\omega}$ is purely imaginary and the pattern grows exponentially with the linear growth rate ω_2. For magnetic inductions smaller than B_c, ω_2 is negative and any pattern decays. ω_1 may be different from zero, resulting in an oscillatory decay. As opposed to the experiments conducted by Reimann *et al.* (2003), oscillations are never observed in our experiments due to the high viscosity, and therefore the real part ω_1 is always small and can be neglected.

The exponential growth or decay corresponds to a linear amplitude equation for small amplitudes

$$
\frac{\partial A}{\partial t} = \omega_2(A - A_0),
\tag{3.12}
$$

where A_0 is the amplitude of the (un)stable solution. We therefore fit the
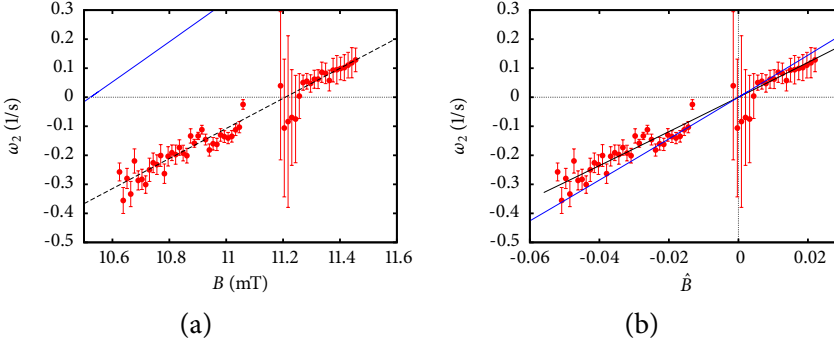
FIGURE 3.9: The linear growth rate ω_2 of the pattern amplitude as a function of the magnetic induction (a) and the rescaled induction (b). The symbols with error bars represent the measured data. The blue solid line shows the theory for the measured surface tension $\sigma = 31\,\text{mN/m}$. The dashed black line in (a) displays a linear fit to the experimental data to find the critical induction $B_{\text{c,exp}}$. The solid black line in (b) shows a best fit of the theory to the data with $\sigma = 20\,\text{mN/m}$.

measured data with equation (3.12) in a region around the flat state solution $A < 0.37\,\text{mm}$, treating A_0 and ω_2 as adjustable parameters. In this region, the measured amplitude equations are at least monotonic and the nonlinearity cannot be seen by visual inspection. In figure 3.8, this linear fit is represented by the dashed line. The resulting growth rate ω_2 is shown in figure 3.9. The comparison of ω_2 versus the induction B provides a rather poor match (figure 3.9 a). The feature most distinct between the theory (blue line) and the experimental data (symbols) is the critical induction B_c, where the growth rate changes its sign. The theoretical analysis with the material parameters from table 3.1 yields

$$B_{\text{c,theo}} = 10.52\,\text{mT}, \tag{3.13}$$

while a linear fit to the experimental data suggests

$$B_{\text{c,exp}} = 11.21\,\text{mT}. \tag{3.14}$$

This 7 % difference of the threshold induction makes a comparison of the growth rate as a function of the induction completely unsuitable, because the growth rate scales with the distance from the critical point. For a meaningful compari-

son, the induction is rescaled (figure 3.9 b) with

$$\hat{B} = \frac{B - B_c}{B_c},\tag{3.15}$$

where B_c is the critical induction of the corresponding dataset. In a restricted range of $\hat{B} \in [-0.025 \ldots 0.015]$, the measured data coincide very well with the theoretical computations within the the experimental error. Outside this range, the experimental data has slightly smaller absolute values than the computed growth rates. By treating the surface tension σ as an adjustable parameter, the experimental data can be fitted in the whole range with the theoretical expression (solid black line in figure 3.9 b) with $\sigma = 20\,\text{mN/m}$. The growth rates determined by this best fit differ from the ab initio calculations by 21 %. This deviation is of the same magnitude as the difference found by Knieling *et al.* (2007). It can partly be caused by an inaccuracy of the material parameters in table 3.1. A lower value of the surface tension, as suggested by the fit, is consistent with the observations from section 3.2, that the surface tension is smaller, when the liquid is allowed to rest, albeit not as small, as determined from the fit.

Another reason for the difference might be the nonlinearity of the real amplitude equation, which deviates from the linear function (3.12). The influence of this nonlinearity depends on the curvature of the amplitude equation, which can hardly be estimated from the very noisy data itself (see figure 3.8). For this matter, the fully nonlinear equations are needed, which will be considered in the next sections.

3.5.3 Approximation with radial basis functions

Figure 3.10 displays the dynamics of the amplitude determined from equation (3.6) in the full range of A and B. The color scale indicates sign and strength of the force $f(B, A)$ and confirms the bifurcation diagram suggested in figure 3.4. However, the data points are not only affected by noise, they are also irregularly distributed. The density is high at the stable solution branch, and in contrary there are "holes" in the diagram, where no data is available at all. These holes belong to datasets which have been removed, because they converge to a localized solution (cf. section 3.5.1).

In order to further interpret the data, a smooth approximation is helpful. We
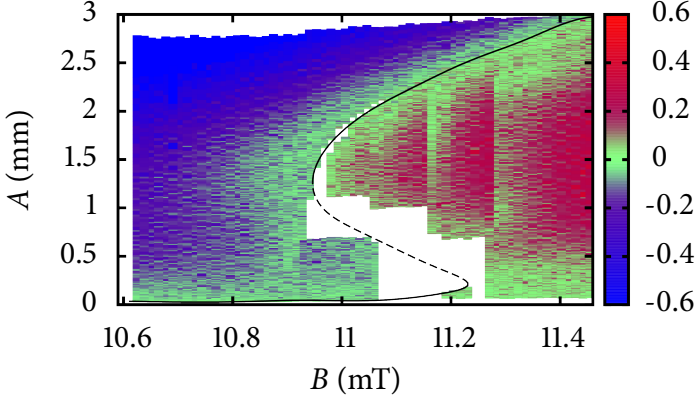
FIGURE 3.10: The measured amplitude dynamics for the whole phase space. The color indicates the force $f(B, A)$. Red (blue) means rising (falling) amplitude, respectively. Green indicates the zero (root of the amplitude equation).

use a multiquadric *r*adial *b*asis *f*unction (RBF) network to compute a smooth sensible approximation to the amplitude equation (Powell 1990). A RBF network is a linear combination of shifted basis functions

$$s(\boldsymbol{r}) = \sum_j \lambda_j \phi(\|\boldsymbol{r} - \boldsymbol{c}_j\|) + p(\boldsymbol{r}), \tag{3.16}$$

with the arbitrarily chosen centres $\boldsymbol{c}_j$ and the weights λ_j. $p(\boldsymbol{r})$ is a low order multivariate polynomial, typically linear or just constant. We choose the multiquadric basis function

$$\phi(x) = \sqrt{1 + x^2} \tag{3.17}$$

and a linear polynomial $p(\boldsymbol{r})$. The vector $\boldsymbol{r}$ is a scaled combination of the
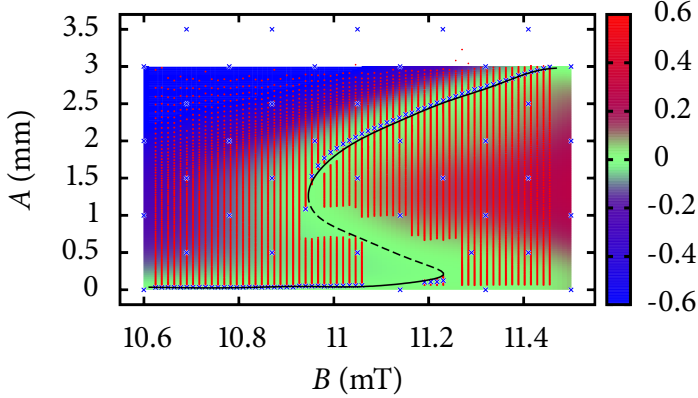
FIGURE 3.11: The multiquadric RBF approximation of the amplitude equation. The red dots correspond to the measured data. The blue crosses show the position of the centres of the radial basis functions. The black solid (dashed) line represents the stable (unstable) zero of the approximant.

coordinates of the phase space

$$\boldsymbol{r} = (B/\delta_B, A/\delta_A) \tag{3.18}$$
$$\delta_B = 0.2\,\mathrm{mT}$$
$$\delta_A = 1\,\mathrm{mm}$$

RBF networks with the basis function (3.17) are infinitely differentiable and thus well-suited to the approximation of smooth functions. This kind of approximation has been proven useful in many applications. For an overview see the review by Hardy (1990).

Figure 3.11 displays the result from fitting the measured data (shown in figure 3.10) with equation (3.16) The centres $\boldsymbol{c}_j$ can be chosen almost arbitrarily; we have selected 50 centres equally distributed in the measured region and additionally placed 68 centres near the stable solution branch. The location of these 118 centres is marked in figure 3.11 by the blue crosses. The scale variables $\delta_{A,B}$ have been chosen according to the empirical rule, that they should be

approximately equal to the distance between centres in the corresponding direction.

Only the weights λ_j in equation (3.16) are adjusted, while the position of the centres $\boldsymbol{c}_j$ are held constant. The problem of adjusting equation (3.16) to our data is therefore reduced to a general linear least squares fitting problem with 118 free parameters. In order to avoid the problem of overfitting, we do not fit the data directly with equation 3.16, but instead apply Tikhonov regularization (Neumaier 1998)

$$\sum_j \left| s(\boldsymbol{r}_j) - f(\boldsymbol{r}) \right|^2 + \xi \sum_k \lambda_k^2 = \text{min!}, \tag{3.19}$$

where $f(\boldsymbol{r})$ are the measured data and ξ is the regularization parameter. This parameter controls the complexity of the model. A value near zero results in a standard least squares fit of the model to the data, while a larger value makes the resulting model more smooth. To find the optimal value for the regularization parameter, we apply standard 2-fold cross validation (Picard & Cook 1984), which yields an optimal regularization parameter of $\xi = 0.4$.

The zero from this fit gives an estimate for the stable and unstable solution of the amplitude equation and is indicated by the solid and dashed black line in figure 3.11, respectively. For comparison, the original data are also shown with the red dots. The RBF reconstruction of the solution gives a very plausible result, which captures the essential features of the raw data, namely the imperfection, and provides an estimate for the unstable solution, which can only be approached to a certain limit by this method (see the holes in diagram 3.10). This result of the RBF reconstruction has also been used to display the equilibrium in the diagrams 3.4 and 3.10 above.

This approximation of the measured data by an RBF network has proven useful to get an unbiased estimate of the equilibrium and to fill in missing data. However, such a non-parametric regression technique cannot provide physically meaningful parameters (Green & Silverman 1994). In the next section, we compare the data with nonlinear model equations for the bifurcation.

3.5.4 Model equations

The standard model equation for a hysteretic bifurcation diagram like 3.4 is a cubic amplitude equation (Cross & Hohenberg 1993)

$$\tau \frac{\partial A}{\partial t} = \varepsilon A + \beta A^2 + \gamma A^3 + \kappa, \qquad (3.20)$$

where τ denotes a time scale and $\varepsilon = (B^2 - B_c^2)/B_c^2$ measures the distance from the bifurcation point. For the diagram depicted in figure 3.4, β must be positive, and the width of the hysteresis increases with the magnitude of β. In order to get stable patterns for $\varepsilon > 0$, γ must be negative, and the final amplitude decreases with the magnitude of γ. The constant term κ represents the imperfection of the system. For $\kappa \neq 0$, the transcritical bifurcation at $\varepsilon = 0, A = 0$ dissolves into two saddle-node bifurcations, the distance of which is controlled by the magnitude of κ.

Equation (3.20) does not incorporate any specific knowledge of the mechanism of the instability, it can be applied to a wide range of physical pattern forming systems like non-Boussinesq Rayleigh-Bénard convection (Busse 1967), Bénard Marangoni convection (Schatz *et al.* 1995) or chemical reactions (Turing 1952; Cross & Hohenberg 1993). For the case of the Rosensweig instability, Bohlius *et al.* (2008) provide a systematic derivation of this amplitude equation.

Friedrichs & Engel (2001) formulate the free energy density $\mathcal{F}$ of a magnetic liquid as a function of the pattern amplitude. From this expressions, one can extract an alternative amplitude equation of the hexagonal pattern of the Rosensweig instability

$$\tau \frac{\partial A}{\partial t} = \varepsilon A + \beta \left(1 + \varepsilon\right) A^2 + \gamma A^3 + \kappa, \qquad (3.21)$$

with the only difference being the additional factor $(1 + \varepsilon)$ in the quadratic term. The physical reasoning behind this higher order correction is a scaling of the quadratic coefficient with B^2, which is treated equivalently to B_c^2 in the classical analysis. By making this dependence explicit, and with $1 + \varepsilon = B^2/B_c^2$, one arrives at equation (3.21). In the limit of $\varepsilon \to 0$, both equations coincide.

From a more abstract point of view, one might ask, whether this additional factor $(1 + \varepsilon)$ in the quadratic term could also incorporate another adjustable

parameter, resulting in the equation

$$\tau \frac{\partial A}{\partial t} = \varepsilon A + \beta \left(1 + \lambda \varepsilon\right) A^2 + \gamma A^3 + \kappa. \tag{3.22}$$

Such a model can reduce to either of the two previous equations in the limits $\lambda = 0$ and $\lambda = 1$. Therefore, a comparison of the experimental data with the latter equation provides some evidence, whether it is empirically advantageous to incorporate the ε-dependence in the quadratic coefficient.

The coefficients in the equations (3.20) and (3.21) are in principle given by Bohlius *et al.* (2008) and Friedrichs & Engel (2001), respectively, as functions of the material parameters. However, these analyses are carried out for a linear magnetization curve $M(H) = \chi H$ and, in the latter case, small values of χ only, and therefore cannot be directly applied to our fluid. By treating $\tau, B_c, \beta, \lambda, \gamma$, and κ as adjustable parameters, these equations can nevertheless be fitted to the measured data.

Figure 3.12 displays the result of fitting the model equations to the experimental data together with the RBF approximation of the previous section for reference. At a first glance, all models give reasonable approximations to the experimental data and the differences are minor. One such difference becomes apparent when looking at the equilibrium line (black solid line). The experimental data (red dots) evidently contain the final static amplitude in almost all cases, so the equilibrium should pass through, or very nearby the endpoints of the experimental data lines. This condition does not hold for the plain cubic equation in figure 3.12 (a). The width of the bistable regime suggested by the experimental data amounts to $\Delta B_{\text{hyst}} = 0.29\,\text{mT}$, but the cubic equation provides only $\Delta B_{\text{hyst}} = 0.18\,\text{mT}$. The equation (3.21), which is augmented with $(1 + \varepsilon)$, gives a much better approximation of the equilibrium line (figure 3.12 b). Here, the width of the hysteresis amounts to $\Delta B_{\text{hyst}} = 0.25\,\text{mT}$, which is better but still smaller than the true value. Finally equation (3.22), which is a blend of the two former models, scores in between them in this test with $\Delta B_{\text{hyst}} = 0.20\,\text{mT}$ (figure 3.12 c). The best fit blend parameter $\lambda = 0.755$ tends more to the augmented equation (3.21) than to the plain cubic equation (3.20). So from this test, the augmented equation (3.21) is the clear winner. Of course, the nonparametric RBF approximation, which is included only for reference in figure 3.12 (d), faithfully reproduces the hysteresis.
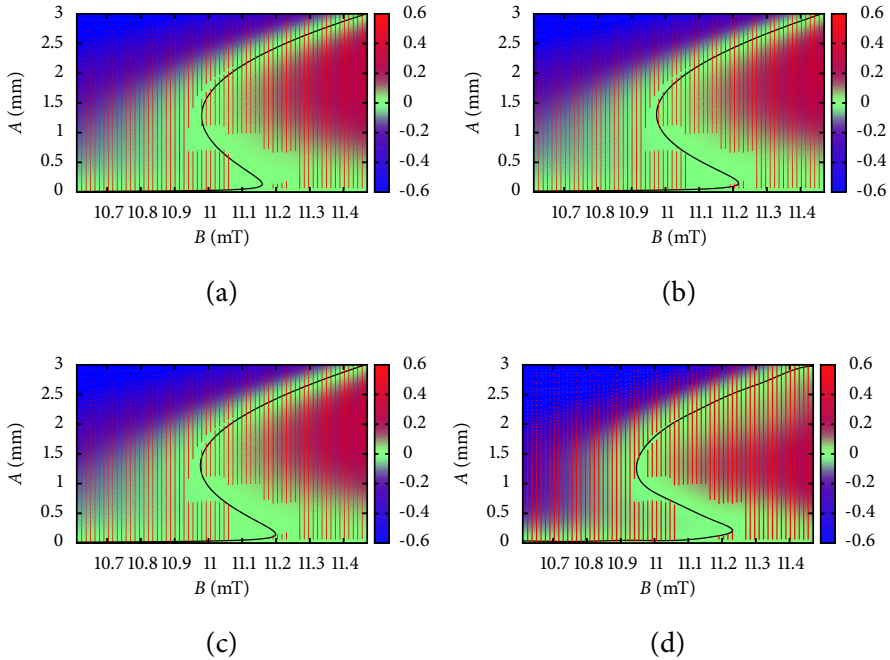
FIGURE 3.12: Comparison of different models for the amplitude equation. (a) cubic equation (3.20) (b) equation (3.21) (c) equation (3.22) with $\lambda = 0.755$ (d) RBF approximation.

Even though the equilibrium curve can be represented reasonably well by at least the augmented amplitude equation, the fitted models all deviate from the measured data off the neutral curve in two ways. At small inductions, the model equations underestimate the velocity of the pattern decay. Figure 3.13 (a) depicts the amplitude equations for an undercritical induction of $B = 10.80$ mT. Here, the model equations all yield approximately the same result, but the difference to the measured data is roughly 30 %. At overcritical inductions (figure 3.13 b), the model equations result in asymmetric curves, while the experimental data suggest symmetric amplitude equations. Of course, the model equations are expansions about the critical point, and are not expected to be accurate far from the critical induction.

For the overcritical induction, also the RBF approximation shows artefacts.
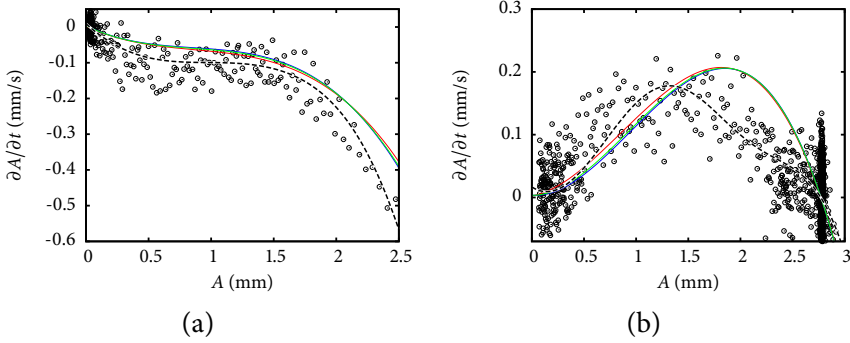
FIGURE 3.13: Comparison of the amplitude equations for a constant induction B = 10.80 mT (a) and B = 11.35 mT (b). The symbols display the original measured data, the dashed line is the RBF approximation, and the solid lines represent the parametric model equations (3.20,red), (3.21,blue) and (3.22,green).

The measured data suggest a smooth shape of the amplitude equation, while the RBF approximant shows a bump near A = 2 mm. This irregularity is probably due to an effect similar to the one which causes the seemingly double equilibrium point in figures 3.6 and 3.8. These double equilibrium points exist also in the neighbourhood of the data shown in figure 3.13 (b) and influence the RBF network, because it is a global approximation scheme.

3.6 Conclusion

Using a highly viscous ferrofluid, the dynamics of the formation of the Rosensweig instability can be slowed down to the order of minutes. Therefore, it is possible to conveniently observe the dynamics using a two-dimensional imaging technique. This is in contrast to the work by Knieling *et al.* (2007), who could observe only a one-dimensional cut through the two-dimensional pattern. From the evolution of the amplitude we have estimated the linear growth rate of the pattern and successfully compared to the theory by Knieling *et al.* (2007). Similar to their experimental work, we find an agreement within 21 % in an 8 % range of the magnetic induction around the threshold value of the instability. In a smaller range of 4 % of the critical threshold, the measured data agree with the theoretical predictions within 9 %.

We have also reconstructed the nonlinear amplitude equations from the measured data. An approximation of the noisy experimental data with radial basis functions provides an estimate for missing data and for the static amplitude. Standard model equations for the instability by Friedrichs & Engel (2001) and Bohlius *et al.* (2008) could be fitted to the experimental data. The estimate of the static amplitude from the plain cubic amplitude equation derived by Bohlius *et al.* (2008) can be significantly improved by augmenting the quadratic coefficient with $(1 + \varepsilon)$, as suggested by the free energy of Friedrichs & Engel (2001). However, a comparison of the absolute magnitude of both amplitude equations with the experimental data at an induction 5 % below the critical induction B_c reveals, that neither amplitude equation can successfully fit all of the measured experimental data. Even if the static amplitude is represented quite well by at least the augmented equation, the data outside the equilibrium line shows deviations both in magnitude (figure 3.13 a) and shape (figure 3.13 b) from the model equations. Future theoretical research would be desirable, which focuses not only on the immediate vicinity of the critical point, but represents the data in a wider range.

By the use of the amplitudes in Fourier space, only space filling homogeneous patterns have been considered. However, the real system has additional degrees of freedom, which are manifested in the formation of localized states as shown in figure 3.7 and observed previously by Richter & Barashenkov (2005). In this chapter, they have not been studied in detail. Further experimental investigation could be dedicated to the spontaneous formation of these localized states in our system as opposed to the work by Richter & Barashenkov (2005), where an external disturbance is needed.

Part II

Ferrogel

4 Magnetodeformation of a ferrogel sphere

A small ferrogel sphere is subjected to a homogeneous magnetic field and consequently stretches along the field lines. When the magnetic field is suddenly switched on, the sphere first performs vibrations around the new equilibrium position and then slowly elongates on a longer time scale. Both phenomena can well be described by a damped harmonic oscillator model, where the spring constant depends on time. Poisson's ratio of the gel can be calculated from the ratio of the relative elongation parallel and perpendicular to the field lines. The static elongation is compared to theoretical descriptions of the problem by Raikher & Stolbov (2005*a*) and Landau & Lifschitz (1960). This chapter investigates, how well can a ferrogel sample be modelled as a uniform elastic magnetizable body in a simple geometry. These results have been published as a regular article in the Journal of Chemical Physics (Gollwitzer *et al.* 2008).

4.1 Introduction

A sphere is the most perfect, most symmetric geometrical object. The Pythagoreans believed that the sun and the earth are perfect and thus spherical. Today we know that the shape of the earth, the geoid, deviates from a perfect sphere by the influence of centrifugal and gravitational forces (Meissner 2002), which break the spherical symmetry. This symmetry breaking is important in various fields of physics. For example, the efficiency of nuclear fission depends on the shape of the nucleus (Bohr & Wheeler 1939). In the case of a magnetic liquid drop, this breaking of the symmetry can be achieved by an external homogeneous field. The droplet then elongates along the direction of the applied magnetic field (Bacri & Salin 1982, 1983), which can be used to measure the interfacial tension between the ferrofluid a second immiscible liquid (Flament *et al.* 1996). Very recently, Lahaye *et al.* (2007) performed a similar experiment with an amount

of "quantum ferrofluid", consisting of dipolar Cr-Atoms, and have found it to elongate as well in a magnetic field.

All examples presented above have in common that they deal with plain fluids, without any elasticity. This means, they are kept together only by the surface tension of the magnetic fluid. A ferrogel, instead, assumes its equilibrium shape in the absence of external forces as a consequence of elastic volume forces (Varga *et al.* 2003). Under the influence of an external field, though, the equilibrium size and shape can be changed significantly (Zrínyi *et al.* 1997*b*). This *magnetic deformation effect* provides the basis for many of the proposed applications, where a piece of ferrogel is supposed to produce work. In this way Zimmermann *et al.* (2006, 2007) build autonomous robots, Zrínyi (2000) propose artificial muscles and Lao & Ramanujan (2004) describe magnetic drug targeting. All these applications need the coupling between the mechanic and magnetic degrees of freedom.

In its simplest form, the magnetic deformation effect is reduced to a spherical piece of gel subjected to a homogeneous magnetic field. An approximation for the resulting deformation has been given by Landau & Lifschitz (1960) for the case of a dielectric elastic sphere, which can readily be transferred to the magnetic case, i.e. ferrogels (Raikher & Stolbov 2003). The relative elongation ε in this case was calculated as

$$\varepsilon = \frac{\kappa \mu_0}{G} M^2 \qquad (4.1)$$

where $\kappa = \frac{1}{15}$, G is the shear modulus and M is the magnetization. Recently, the elongation has been recomputed by Raikher & Stolbov (2005*a*, *b*) without constraining the shape to an ellipsoid. In this case, the elongation is expected to be 30 % larger. This effect has not yet been observed, a possible reason being that it is rather small for the large values of G, characteristic for most of the covalently cross linked polymer gels (Zrínyi *et al.* 1996, 1997*b*). In contrast, the elasticity of the new class of thermoreversible ferrogels (Lattermann & Krekhova 2006) can reversibly be tuned via their temperature. In this chapter, we cast thermoreversible ferrogels in spherical samples and expose them to a uniform magnetic field, to test the above predictions.
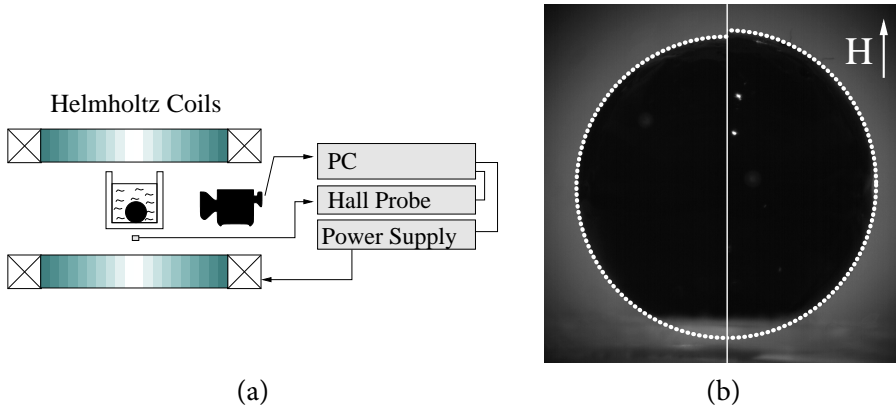
FIGURE 4.1: (a) Schematic drawing of the experimental setup. (b) Image of the symmetrical (left) and distorted ball (right). The dotted line displays a fit with a circle (left) and an ellipse (right).

4.2 Experiment

4.2.1 Setup

The experimental setup is sketched in figure 4.2 (a). A ferrogel ball is immersed in a rectangular container, positioned on the common axis midway between two Helmholtz coils. For the empty Helmholtz pair of coils, the spatial homogeneity is better than ±1 %. This grade is valid within a cylinder of 1 cm in diameter and 14 cm in height oriented symmetrically around the centre of the coils. The coils are powered by a current amplifier (fug electronic GmbH), which is controlled by a computer. The magnetic system cannot follow the control signal immediately. For a maximal jump height $\Delta B = 36$ mT the field is reached after $t_B = 30$ ms, as recorded by the Hall probe (Group3-LPT-231) connected to a digital teslameter (DTM 141).

The temporal evolution of the ball shape is recorded using a high-speed camera, capable of taking 400 frames per second with a resolution of 768×768 pixels. Figure 4.2 (b) shows the original and distorted shape. The dotted curves stem from a fit of a circle to the edges in the image. The circle is located utilizing a normalized correlation technique (Dickey & Romero 1991), where the correlation between the gradient of the image and a circle is maximized.

The gradient is estimated by the Sobel operator (Wang *et al.* 2006), and the circle is rasterized with anti-aliasing provided by a Gaussian filter (Crow 1977). This method is able to extract the radius and the coordinates of the centre with subpixel resolution.

4.2.2 Material

The ball was prepared with a magnetic, thermoplastic elastomer gel or in other words with a thermoreversible ferrogel (Lattermann & Krekhova 2006). Therefore, an ABA-type poly(styrene-b-(ethylene-co-butylene)-b-styrene) (SEBS) triblock copolymer (Kraton G-1650) was used as a gelator. As measured with size exclusion chromatography (SEC), Kraton G-1650 exhibits a molar mass of 99 000. The styrene content is 29 % (manufacturer information). The gelator concentration is 3.5 w% per paraffin oil used. The ferrofluid was prepared in the way described by Lattermann & Krekhova (2006) with 24.5 w% magnetite per paraffin oil Finavestan A 50 B (Total). The shear viscosity at 20 °C of 11 mPa s and the molar mass of 280 (manufacturer information) are lower than that of the paraffin oil Finavestan A 80 B used by Lattermann & Krekhova (2006). Using A 80 B, the resulting ferrogels are too stiff to be remarkably deformed by the magnetic field. On the other hand, using the gelator Kraton G-1652 instead of Kraton G-1650 with a lower molar mass of 79 000 (SEC), the prepared ferrogels are too soft, i. e. they are not shape-retaining. Furthermore, they sweat out ferrofluid, slowly on standing, faster in the magnetic field.

4.2.3 Sample preparation

Above its softening temperature at 45°C the material becomes a magnetic liquid. We produce the ferrogel sphere by casting the liquid into an aluminium mould at 55°C. The mould consists of two parts with a spherical cavity, tightly screwed together, which is connected by a thin channel to a hopper mounted on top of the upper part. To avoid any air bubbles in the final sphere, the mould is first filled with the liquefied material under vacuum (≈ 1 mPa). Then atmospheric pressure is applied, which compresses any low-pressure air bubbles. By repeating the process of varying the ambient pressure and under the influence of gravity, eventually all bubbles leave the mould via the hopper. Next we cool down the mould and separate the two parts of it.
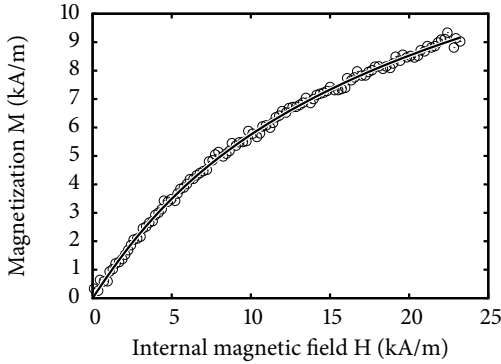
FIGURE 4.2: Magnetization curve of the ball.

The ball is then immersed into water with added salt. The salt establishes a vertical density gradient which keeps the ball floating in the middle of the container at half depth. With the help of a syringe, water has been sampled directly above and below the ball. The density of both samples is then measured by means of a vibrating tube density meter (DMA 4100, Anton Paar Co.). From the mean of both values follows the density of the ball to be $\rho = 1085 \pm 3\,\mathrm{kg/m^3}$.

The density of the solution of salt is subsequently reduced by adding pure water, until the ball touches the bottom of the container. All experiments have been carried out in this configuration, where the density of the surrounding liquid is only slightly smaller than that of the sphere. This is necessary to reduce the influence of the gravity on the shape of the sample; the ball is so soft that, without buoyancy, it is deformed into an oblate ellipsoid under gravity.

4.2.4 Magnetization

Next, we measure the magnetization of the sphere for various fields, utilizing a fluxmetric magnetometer (Lakeshore, Model 480). The resulting magnetization curve is plotted in figure 4.2. The solid line displays an approximation with the model presented by Ivanov & Kuznetsova (2001). The sample is superparamagnetic with an initial susceptibility $\chi_0 = 0.81$.
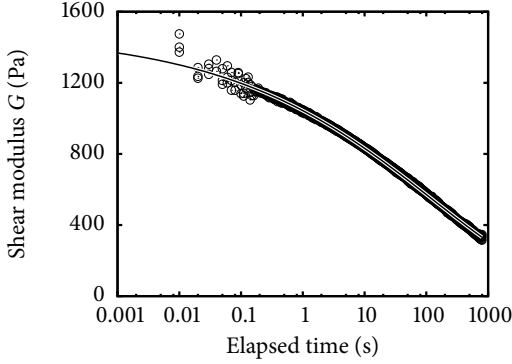
FIGURE 4.3: The force response to a jump in the deformation. The solid line displays a fit to equation (4.2) with the parameters G_{rheo} = 1480 Pa, t_0 = 127 s and β = 0.218.

4.2.5 Rheology

For the characterization of the elastic properties we measure the shear modulus G with a rheometer (MCR 301, Anton Paar) in cone and plate geometry. The cone has a diameter of 50 mm and a base angle of 1°. We perform a stress relaxation experiment on the sample: from the equilibrium position we shear the sample by a deformation of γ = 1 % and measure the stress τ as a function of time. Figure 4.3 displays the results. The restoring force decays by 50 % during one second, which means that the shear modulus $G = \tau/\gamma$ cannot be treated as constant. This decay can well be approximated by a stretched exponential (the solid line in figure 4.3)

$$G(t) = G_{rheo} \exp\left(-(\frac{t}{t_0})^\beta\right). \tag{4.2}$$

The material therefore softens under load. To account for that time dependence, the magnetic experiment cannot be performed in a static manner.

4.3 Results and discussion

We performed time-resolved measurements of the relative elongation ε of the ball after applying a magnetic induction B in a jump-like fashion for ten different values of B. Figure 4.4 shows $\varepsilon(t)$ for the case B = 36 mT. The elongation $\varepsilon = (d - d_0)/d_0$ measures the scaled difference of the diameters in the direction
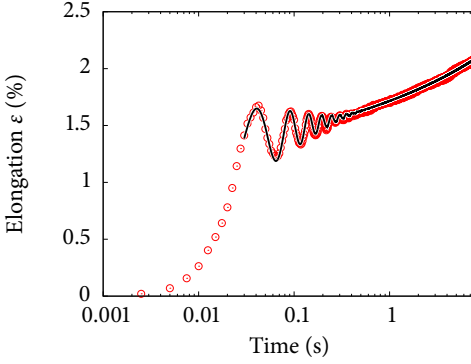
FIGURE 4.4: Elastic response of the ball, when a magnetic field is suddenly applied. The solid line represents a fit to equation (4.3).

of the field (d) and without a field (d_0). Due to the sudden increase of the magnetic field and the inertia of the ball, the latter performs uniaxial damped vibrations with a frequency f = 22.4 Hz. When the oscillations cease, the elongation continues to grow due to the softening under load. Because the time scale of the softening is much larger than that of the oscillation, the experiment may be approximated by a harmonic oscillator pulled by a constant force, where the spring constant relaxes according to equation (4.2)

$$\ddot{\varepsilon} + \delta\dot{\varepsilon} + \omega_0^2 \exp\left(-(\frac{t}{t_0})^\beta\right) \varepsilon = F. \tag{4.3}$$

Here δ is the damping constant, F the pulling force (i.e. related to the magnetic induction) and ω_0 the natural frequency. A fit with the solution of that equation is displayed in figure 4.4 as the solid line. The ratio F/ω_0^2 corresponds to the relative elongation in the equilibrium state if the spring constant would not change. Therefore, this ratio compares to the elongation predicted by the static theories.

The dependence of the elongation on the magnetization is shown in figure 4.5 a. For ten different values of the magnetic induction we have recorded and evaluated the elongation ε of the ball. Figure 4.5 a presents the outcome for the elongation parallel (ε_z) and perpendicular (ε_x) to the magnetic field. The data have been plotted versus M^2. In agreement with equation (4.1) we find a linear relationship $\varepsilon_i = c_i M^2$ with $c_z = 13.4 \cdot 10^{-5} (\frac{m}{kA})^2$ and $c_x = -6.1 \cdot 10^{-5} (\frac{m}{kA})^2$. Figure 4.5 b shows the oscillation frequency $f = \omega_0/(2\pi)$ versus M^2.
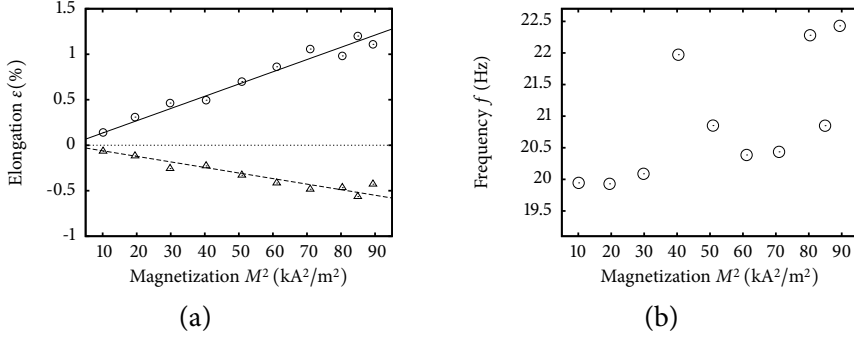
FIGURE 4.5: (a) The static elongation as a function of M^2. The circles (triangles) denote the elongation (contraction) parallel (perpendicular) to the applied field, respectively. The solid (dashed) line is the best linear fit. (b) The frequencies of the initial vibrations obtained from equation (4.3).

Next we compare the ratio of the slopes $c_z/c_x = \kappa_z/\kappa_x$ with the theoretical predictions. For a deformation restricted to an ellipsoidal shape and the assumption of a uniform strain field, the expressions given by Landau & Lifschitz (1960) can be rewritten in terms of Poisson's ratio σ

$$\kappa_z = \frac{3 - 2\sigma}{20\sigma + 20} \tag{4.4a}$$

$$\kappa_x = \frac{1 - 4\sigma}{20\sigma + 20}. \tag{4.4b}$$

For an incompressible gel ($\sigma = 1/2$) this leads to $\kappa_z = \frac{1}{15}$. For arbitrary σ one obtains for the ratio

$$\kappa_x/\kappa_z = \frac{1 - 4\sigma}{3 - 2\sigma}. \tag{4.5}$$

We exploit equation (4.5) to determine σ, and by substituting σ in the equations (4.4b) and (4.1), one finally arrives at G. This yields

$$\sigma = 0.48 \pm 0.01 \quad G = 0.65\,\text{kPa}. \tag{4.6}$$

For the more general case of a non-uniform strain field and a shape not

restricted to an ellipsoid considered by Raikher & Stolbov (2005*a*), one obtains

$$\kappa_z = -\frac{6\sigma^2 + \sigma - 7}{20\sigma^2 + 48\sigma + 28} \tag{4.7a}$$

$$\kappa_x = -\frac{\sigma^2 + 2\sigma}{10\sigma^2 + 24\sigma + 14} \tag{4.7b}$$

which yields

$$\kappa_x/\kappa_z = \frac{2\sigma^2 + 4\sigma}{6\sigma^2 + \sigma - 7} \tag{4.8}$$

and finally gives

$$\sigma = 0.47 \pm 0.01 \quad G = 0.87\,\text{kPa}. \tag{4.9}$$

Both approaches yield a Poisson's ratio σ very close to the limit of incompressibility $\sigma = \frac{1}{2}$, which is characteristic for rubberlike materials (Rinde 1970). As Raikher & Stolbov (2005*a*) already point out, the values derived for the shear modulus G differ by $\approx 30\,\%$. But the value obtained from the rheometer, $G_{\text{rheo}} = 1.48\,\text{kPa}$, exceeds the old and new predictions by a factor of 2.3 and 1.7, respectively. So none of them is corroborated by the experiment.

The frequency of the vibrations after the sudden increase of the magnetic field offers another possibility to measure the shear modulus. For an incompressible elastic sphere that performs spheroidal vibrations, where the sphere gets alternately deformed into a prolate and oblate ellipsoid of revolution, the frequency is given by (Love 1944) as

$$f = 0.848\sqrt{\frac{G}{4\rho r^2}}. \tag{4.10}$$

Since the radius of the sphere r and the density ρ are known, we can compute the shear modulus from the measured vibration frequency f. Figure 4.6 shows a comparison of the value of the shear modulus obtained from f with the values from the elongation and the mechanical measurement. The average shear modulus determined by this method is $G_{\text{vib}} = 0.1\,\text{kPa}$, which differs by a factor of 15 from G_{rheo}. This large deviation may arise, because the model for the vibrations does not take into account the surrounding water. This needs to oscillate together with the sphere, leading to an increased effective mass of the oscillator, and thus a reduced frequency.
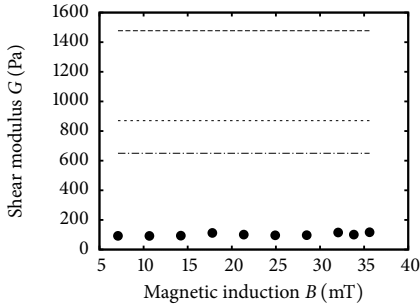
FIGURE 4.6: The shear modulus measured by different methods: Commercial rheometer (dashed), elongation theory by Raikher & Stolbov (2005*a*) (short dashed), elongation theory by Landau & Lifschitz (1960)(dash-dotted), vibrations (solid circles).

Now we reconsider the deviation between the shear modulus G as determined from the elongations and G_{rheo} determined via rheology. They differ by factor of about two. This difference cannot be explained solely by the inaccuracy of the measurement of G_{rheo}, which is typically around 10 % for a commercial rheometer. Rather, the deviation is likely to stem from the fact that the idealistic models by Landau & Lifschitz (1960) and Raikher & Stolbov (2005*a*) consider only Hookean elasticity, which is insufficient for our material. In fact, the deformation of a gel put under load can be made up of three contributions, namely instantaneous elastic deformation, retarded anelastic deformation and viscous flow (Strobl 1997). Our material clearly shows anelasticity, as demonstrated in figure 4.3. Moreover, our sample shows the phenomenon of viscous flow, as illustrated in figure 4.7. In this measurement we first apply a constant strain for 800 s, and then record the relaxation of the strain for zero stress. The remaining deformation at $t = 7000$ s is about 15 % of the strain initially applied. This value can be regarded as an upper bound for the plastic contribution to the deformation (viscous flow). While the existence of anelasticity and viscous flow gives no straight-forward explanation of the 70 % deviation between experiment and theory, it is obvious that the full viscoelastic behaviour of the gel should be included in the computations from the very beginning.

4.4 Conclusion

We have measured the deformation of a ferrogel sphere in response to a uniform magnetic field by direct optical means. We compare the results for the first time with the models by Landau & Lifschitz (1960) and Raikher & Stolbov
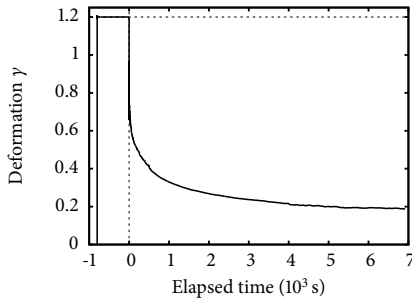
FIGURE 4.7: The shear deformation as a function of time, after applying a constant deformation of 1.2 % for 800 s.

(2005*a*, *b*). From the ratio of the elongation parallel and perpendicular to the field, we calculate Poisson's ratio, which is close to the value $\sigma = 0.5$, which is expected for an incompressible material. More importantly, the absolute value of the elongation is 70 % larger than the one calculated from the models. This is presumable caused by the neglection of the anelasticity and viscous flow of the ferrogel. Very recently, Morozov *et al.* (2009) proposed another model which incorporates magnetostriction. The elongation predicted by them is four times smaller than the elongation computed by Raikher & Stolbov (2005*a*). Therefore also this enhanced model can not explain our findings.

So further theoretical investigation, including the full viscoelastic properties of the gel, is needed to explain the experiment quantitatively. With such a model one would also be able to compute the dynamic response of the gel under a sudden change of the external magnetic field. This is not only of fundamental interest, but also important for possible technical applications of these smart materials.

5 Rosensweig instability with a ferrogel

After experiments on pattern forming surface deflections with plain ferrofluids in the static and dynamic case (chapters 2 and 3), and shape changes of ferrogels in a simpler geometry (chapter 4), we now move on to pattern formation in ferrogels. Since magnetic gels are a relatively new class of materials, available for one and a half decade, intensive research is currently under way to find new applications on the one hand and to explain the basic physical properties on the other hand. Into the second category belongs the question introduced by Bohlius *et al.* (2006*a*), whether the normal field instability also exists in ferrogels and how the pattern formation differs from plain ferrofluids. This chapter describes an experimental realization of the instability with thermoreversible ferrogels. These results have been published in Soft Matter (Gollwitzer *et al.* 2009*a*).

5.1 Introduction

The Rosensweig instability on the surface of a magnetic liquid is a well-researched topic. A basic explanation for the spontaneous formation of surface protuberances balances magnetic energy on the one hand and gravity and surface tension on the other hand. From these, only the magnetic energy favours the formation of spikes, which decreases the demagnetizing field and lowers the overall energy. In case of a ferrogel, additionally elastic energy comes into play, which also counteracts the patterned surface. Bohlius *et al.* (2006*a*) first address this issue and derive the critical induction B_c by means of a linear stability analysis from the dynamic equations formulated by Jarkova *et al.* (2003). According to their analysis, the threshold B_c can be expressed in terms of the surface tension σ, the mass density ρ, the gravity g, and of the elastic shear

modulus G of the gel as

$$B_c^2 = 2 \frac{\mu_0 \mu_r (\mu_r + 1)}{(\mu_r - 1)} (\sqrt{\sigma \rho g} + G), \tag{5.1}$$

where μ_0 is the vacuum permeability and μ_r is the relative permeability of the ferrogel.

In comparison to the formulae given by Cowley & Rosensweig (1967) for the normal field instability in ferrofluids with $G = 0$, the threshold value is increased by the elasticity due to an enlarged "stiffness" of the surface. On the other hand, the critical wavelength is independent of the elastic modulus of the gel and is equal to the capillary wavelength

$$k_c = \sqrt{\frac{\rho g}{\sigma}}, \tag{5.2}$$

as with ferrofluids (Cowley & Rosensweig 1967). In both cases, neither the critical field nor the critical wavelength depend on the viscosity. On a side note, Bashtovoi (1978) predicts, that the critical wavelength increases drastically with the elasticity for the case of a ferrofluid layer covered with a thin elastic film. In this chapter, however, we are dealing with bulk elasticity, which, according to Bohlius *et al.* (2006a), leaves the wavelength unchanged.

More recently, Bohlius *et al.* (2006b) derived the final pattern which forms in ferrogels. These results are limited to patterns of small amplitude and were obtained via a minimization of the energy density, similarly to the method used for ferrofluids by Gailitis (1977) and Friedrichs & Engel (2001). This weakly nonlinear analysis makes it possible to discuss the stability of different patterns and the actual bifurcation scenario. In standard ferrofluids, the Rosensweig instability is associated with a transcritical bifurcation and exhibits a hysteresis (Gailitis 1977; Bacri & Salin 1984). Bohlius *et al.* (2006b) now predicts that this hysteresis shrinks with increasing shear modulus in the case of a ferrogel.

The Rosensweig instability in ferrofluids has been studied in many experiments; confer to the review by Richter & Lange (2009). However, its counterpart in ferrogels is still awaiting measurements. The reason for this void is that up to now mostly covalent cross linked polymer gels (Zrínyi *et al.* 1996; Collin *et al.* 2003; Filipcsei *et al.* 2007) have been synthesized. This process results usually in rather "hard" gels. Due to their high elasticity and the saturation of the magne-

tization, one can not excite surface instabilities in these gels even for very high magnetic field strength. Only recently Lattermann & Krekhova (2006) have invented *soft ferrogels* which take advantage of thermoreversible, i.e. physically crosslinked gelators. Contrary to chemically crosslinked, irreversible ferrogels, their elasticity heavily depends on a thermoreversible sol-gel transition and can be controlled via temperature. In the following we investigate the Rosensweig instability in such a thermoreversible ferrogel.

5.2 Material and Methods

5.2.1 Synthesis

We prepared a thermoreversible ferrogel by swelling 5 wt.% of a gelator in an oil-based ferrofluid containing 30 wt.% of magnetite particles. The carrier liquid for the preparation of the ferrofluid was paraffin oil (Finavestan A50B from Total Deutschland GmbH) with a kinematic viscosity $v = 13.6\,\mathrm{mm^2/s}$ at 20 °C and a molar mass of 280 g/mol (manufacturer information). The magnetite particles were prepared by co-precipitation and stabilized with oleic acid (Lattermann & Krekhova 2006). Transmission electron micrographs show, that the diameter of the particles is 8 ± 1 nm (Krekhova & Lattermann 2008). As a gelator we have utilized Kraton G 1726 from Kraton Polymers, Belgium, which is a mixture of 30 wt.% triblock copolymer and 70 wt.% of a diblock copolymer. The triblock copolymer is poly(styrene-b-(ethylene-co-butylene)-b-styrene) (SEBS) with a molar mass of $\bar{M}_W = 77\,700$ and a polydispersity index PDI = 1.01 (Krekhova & Lattermann 2008). The diblock copolymer (SEB) is exactly one half of the triblock. The size distribution has been established by means of size exclusion chromatography. For both the di- and triblock copolymer the styrene content amounts to 30 wt.% (manufacturer information). In comparison with the pure triblock copolymers used by Krekhova & Lattermann (2008), the diblock acts here as a plasticizer and lowers the softening temperature to 25 °C, according to the falling ball method (Lattermann & Krekhova 2006). Both the ferrofluid and the ferrogel reveal no structure in optical micrographs, i.e. they are perfectly homogeneous down to a sub-micrometer scale. The ferrogel sample remains stable for 1½ year without any separation of the fluid phase from the gelator, i.e. without any syneresis. Likewise, we did not observe changes of the magnetic properties and the microstructure within this time.
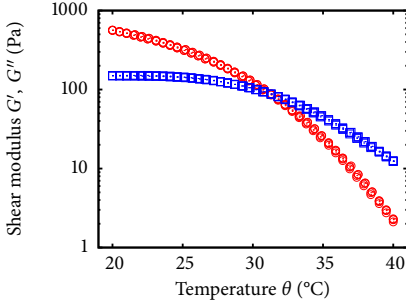
FIGURE 5.1: Storage modulus G' (red circles) and loss modulus G'' (blue squares) versus the temperature for the thermoreversible ferrogel.

5.2.2 Material properties

For the characterization of the elastic properties we utilize a rheometer (MCR 301, Anton Paar) in cone-and-plate geometry. The cone has a diameter of 50 mm and a base angle of 1°. The rheometer is equipped with a Peltier thermostated temperature device (C-PTD 200/E). Figure 5.1 displays the result of oscillatory measurements of the shear modulus at 1 Hz for a deformation of $\gamma = 0.01$ versus the temperature. G' and G'', which denote the real and imaginary part of the shear modulus, respectively, have a crossover around 31 °C. Above $\approx$ 45 °C, the sample becomes liquid.

To measure the magnetization curve of the ferrogel, we use the method described in section 4.2.3 to produce a sphere of the gel enclosed in an aluminium container. The magnetization of the spherical sample was then measured by means of a fluxmetric magnetometer (Lake shore, model 480) at $\theta = 20$ °C. Figure 5.2 shows this data. The sample is superparamagnetic with an initial susceptibility of $\chi_0 = 0.82$. This data has been fitted with the model of Ivanov & Kuznetsova (2001), assuming a gamma distribution of the particle diameters (cf. equation 2.6). We use this model as well to extrapolate $M(H)$ for all sample temperatures, by evaluating the fit with a different θ, while all other parameters are held constant. As an example, the dashed line gives the extrapolation for the maximal applied temperature of $\theta = 38$ °C.

The density ρ of the ferrogel is measured with the same method used in section 4.2.3, where the sphere is suspended in a solution of salt. The density amounts to $\rho = 1085 \pm 1$ kg/m³.

More cumbersome is an estimate for the surface tension σ. As a rough estimate, we measure the surface tension of the paraffin based ferrofluid the
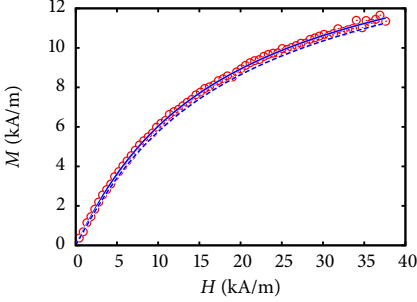
FIGURE 5.2: Magnetization as a function of the applied magnetic induction for the thermoreversible ferrogel. The solid line represents a least squares approximation with the model by Ivanov & Kuznetsova (2001). The best fit parameters for the gamma distribution are: exponent α = 8.1 ± 1.3, mean diameter $d_0 \cdot (\alpha + 1)$ = 8.1 ± 0.4 nm, volume fraction ϕ = 3.9 ± 0.09 %. The core magnetization has been held constant at M_F = 446 kA/m. The dashed line indicates the prediction for θ = 38 °C with the above parameters.

gel was created from with a ring-tensiometer (LAUDA TE 2). We get σ_{FF} = 28.7 mN/m for both the ferrofluid and also the underlying paraffin oil that was used as a carrier liquid for the ferrofluid. For obvious reasons, the tensiometer can not be directly applied to the ferrogel. Because the gelator is not surface active, it shall not have a significant influence on σ. We therefore use σ_{FF} in the subsequent calculations as the surface tension of the gel.

5.2.3 Setup for measurements of the normal field instability

The experimental setup is shown in figure 5.3 (a). To measure the surface deformation, the two-dimensional X-ray imaging technique is employed, which is described in detail in section 2.3.1. We record the height profiles with the fastest possible frame rate of 7.5 Hz. At this rate, an individual frame has a noise floor with an RMS value of h_{RMS} = 20 μm in the vertical direction. Only by averaging many frames (≈ 2000), the theoretical resolution of the detector of 0.4 μm can be achieved. The calibration of the absolute height is limited to ≈ 0.1 mm by the stability of the X-ray source and the mechanical positioning. For details see section 2.3.1.

As a container for the ferrogel a thermostated aluminium block of size (x,y,z)=(60,60,50) mm³ is used in this chapter. A cylindrical bore of 50 mm and a depth of 25 mm serves as a vessel for the ferrogel. A bore with the same diameter, but a depth of 23 mm penetrates the block from the lower side, in this way leaving a bottom plate with a thickness of 2 mm (cf. figure 5.3 a). Utilizing thermal grease, the vessel is thermally connected to two Peltier elements, as
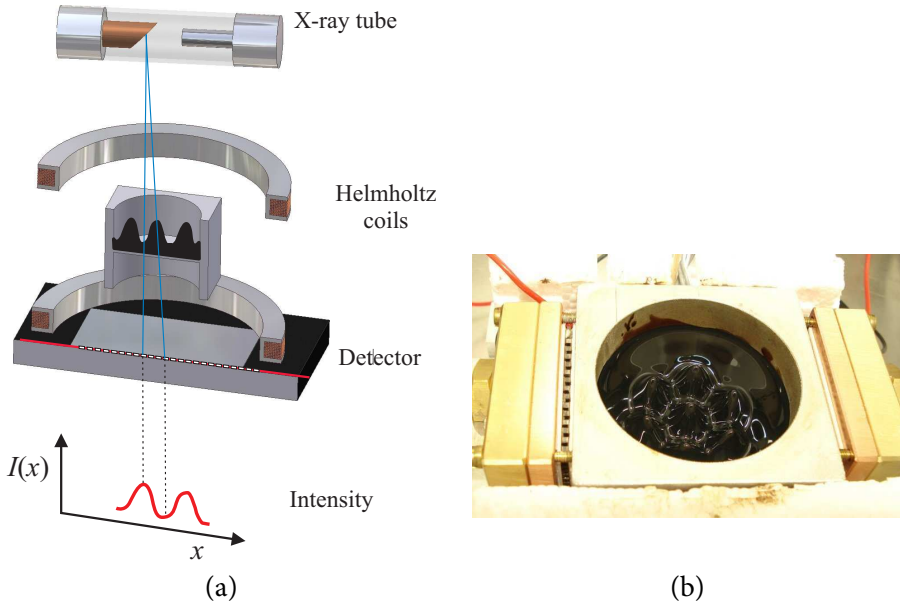
FIGURE 5.3: Experimental setup. (a) Scheme of the setup (not to scale) (b) Photograph of the temperature controlled container, filled with ferrogel.

shown in figure 5.3 (b). They are equipped with heat exchangers (1A cooling Co., type 1A-SL2), which are circulated by water from a closed cooling system (LAUDA RK20 KP). A thermo-resistor Pt100 serves to monitor the temperature of the vessel. The Peltier elements are powered by a DC-current source (EUROTEST Co., type LAB/SL 230/AI/LT) which is controlled via IEEE from the computer. By a proportional-integral method, the computer regulates the temperature of the vessel with a precision of 5 mK in the range of −35 °C to 110 °C. The vessel is covered from above by means of an aluminium plate with a thickness of 0.5 mm. This lid creates an insulating layer of air above the free surface of the ferrogel. This small aspect ratio $\Gamma = h/d \approx 5$ of the container has been chosen, because the amount of ferrogel was limited.

Prior to each series of measurements, a batch of 12 ml of ferrogel is positioned in the empty vessel. This amount is molten by heating up the vessel to 90 °C, in this way creating a flat layer of ferrogel. Then the temperature is lowered to the desired value for the measurement and held constant.
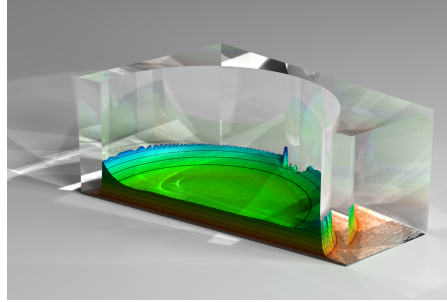
(a)
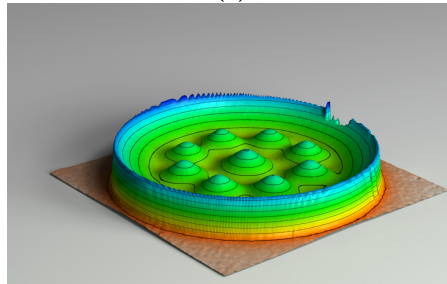
(b)

FIGURE 5.4: A Rosensweig pattern emerging in ferrogel, measured by radioscopy: (a) cross section for B = 22.9 mT; the transparent material illustrates the size of the aluminium container; (b) full profile for B = 28.1 mT. The black contour lines indicate consecutive levels with a distance of 1 mm.

5.3 Results

5.3.1 Quasistatic Experiments

Figure 5.4 presents characteristic topographies of the ferrogel for subcritical (a) and supercritical inductions (b). Due to the step-like jump of the magnetization at the container edge, a field gradient arises which attracts the ferrogel towards the container edge. Therefore a meniscus is formed. Chart (b) shows an example of the Rosensweig pattern. In the following, the height h of the central peak of the pattern serves as an order parameter and is estimated by fitting a paraboloid to the tip of the spike.
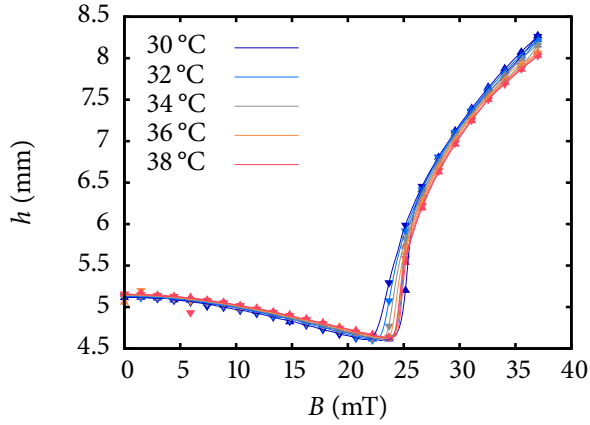
(a)
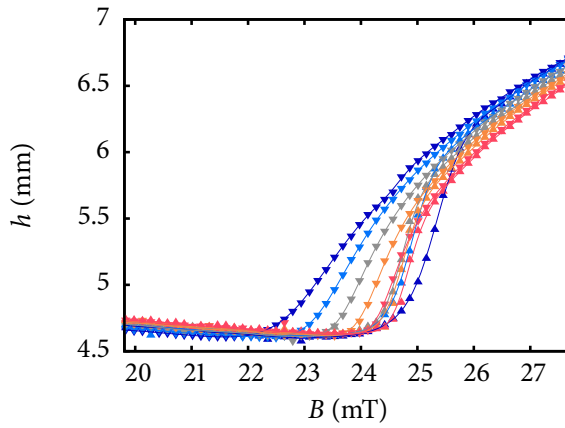
(b)

FIGURE 5.5: Height of the central peak for an increase (upward triangles) and decrease (downward triangles) of the magnetic induction. The colour encodes the temperature from 30 °C (blue) to 38 °C (red), as in the legend. (a) Full range. For clarity only every 10th data point is shown. The lines are splines to the full data set. The time for the measurement was 2 h. (b) Zoom of the hysteresis. All data points are shown.
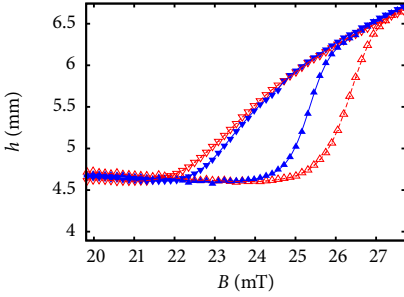
FIGURE 5.6: Height of the central peak for increasing induction (upward triangles) and for decreasing induction (downward triangles). The time between subsequent data points was doubled from 14.4 s (red dashed line) to 28.8 s (blue solid line). The time for a full cycle from 0 mT to 37 mT amounts to 2 h and 4 h, respectively.

Figure 5.5 gives the variation of the order parameter for a slow increase (upward triangles) or decrease (downward triangles) of the magnetic induction for five different temperatures. In the interval from $B = 19$ mT to around 24 mT one notices a monotonic decay. In this regime no spikes exist. However, due to the formation of a meniscus (cf. figure 5.4 a), the level of the material in the central part of the vessel, where h is estimated, decreases. For higher inductions, we observe a steep increase of h for all curves. It is this regime where the ferrogel spikes are emerging.

Whereas in laterally infinitely extended liquid layers the transcritical bifurcation gives a proper scaling of the order parameter (Friedrichs & Engel 2001), for small pools of ferrofluid, imperfections induced by the container edges obscure the analytical scaling law. In this case, only a numerical model is available (Spyropoulos *et al.* 2010; Gollwitzer *et al.* 2009*b*). In lack of an analytical expression, we can not extrapolate the values for the critical induction B_c from a fit of $h(B)$. As an approximation for the threshold of the predicted discontinuous transition we determine the induction $B_{max.up}$ where the amplitude $h(B)$ has its steepest inclination, i.e. $\partial h/\partial B = $ max. It is determined from a spline fit and listed in table 5.1 for all investigated temperatures. A lower bound for the threshold is given analogously from the data for decreasing magnetic induction. It is denoted by $B_{max.dn}$. The hysteresis, defined by $B_{max.up} - B_{max.dn}$, is in the range of 2 mT at 30 °C and shrinks to a fraction of 1 mT at 38 °C, as shown in the zoom presented in figure 5.5 (b).

Next we check, whether the time for a measurement cycle in B has an influence on the evolution of the order parameter. In figure 5.6 we present the results for a measurement cycle of 2 h (red dashed line) and of 4 h (blue solid
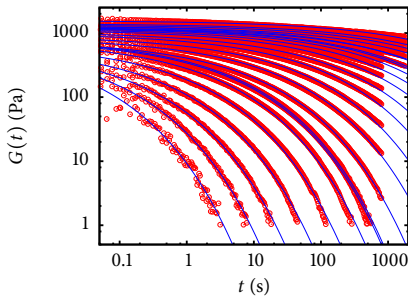
FIGURE 5.7: Time dependent shear modulus $G(t, \theta)$ after a jump in the deformation of $\gamma = 0.01$ for different temperatures of the ferrogel. The temperatures have been varied from $-10\,°C$ to $32\,°C$.

line) for a temperature of $\theta = 30\,°C$, which is the lowest temperature, at which the measurements discussed beforehand have been performed. One clearly sees that the hysteresis between the upward- and downward branch shrinks for longer cycle times. This variation is in the range of $1\,mT$.

For higher temperatures (and lower G) the influence of the cycle time becomes even less significant. Notwithstanding, the influence of the cycle time indicates, that we have different time scales in the ferrogel. These time scales will be studied next.

5.3.2 Dynamic Experiments

Stress Relaxation Experiment

In order to characterize the shear modulus G, we perform a stress relaxation experiment for a series of temperatures. We shear the sample by a deformation of $\gamma = 0.01$ and measure the relaxation of the stress τ while the deformation is held constant. Figure 5.7 displays the data points recorded for various temperatures of the sample.

For a specific temperature, the restoring force decays drastically during one second, which means that in our experiment, the shear modulus $G = \tau/\gamma$ cannot be treated as constant.

Commonly, a stretched exponential function is used to describe the time dependent moduli of linear viscoelastic media (Kohlrausch 1854, 1863; Williams

& Watts 1970; Berry & Plazek 1997; Anderssen *et al.* 2004)

$$G(t, \theta) = G_0(\theta) \exp\left(-\left(\frac{t}{t_0(\theta)}\right)^\beta\right).$$ (5.3)

Here, the exponent β is restricted to the range $[0, 1]$, with $\beta = 1$ for a simple exponential decay, and an increasingly broader distribution of relaxation times for smaller values of β. Moreover, this scaling law was recently observed in the stress relaxation of a triblock copolymer subject to an extensional strain (Hotta *et al.* 2002), and consecutively explained in a model, which assumes that the copolymer reversibly splits into domains of different size (Baeurle *et al.* 2005). These domains consist of a regular homogeneous network of PS micelles which are interconnected by bridging chains of the middle block of the polymer. Also in our ferrogels, we observe glassy PS micelles arranged in clusters, which are interconnected by bridging chains of the ethylene-butylene middle block of the triblock copolymer gelator used. The size of these domains varies in the range from 60 to 120 nm (Lattermann & Krekhova 2006).

Next, we apply (5.3) to our relaxation data. The solid lines in figure 5.7 give approximations of $G(t, \theta)$ with equation (5.3) for different temperatures θ from $\theta = 32\,°\text{C}$ down to $-10\,°\text{C}$. This temperature range was determined by the resolution of our rheometer. All the fits use a common exponent β. The best value amounts to $\beta = 0.34 \pm 0.01$.

The characteristic relaxation time $t_0(\theta)$ of the ferrogel drops drastically with increasing temperature. It varies over six orders of magnitude, as shown in the Arrhenius plot figure 5.8. However, the dependence does not make up a straight line – therefore no simple Arrhenius behaviour with an activation energy can be inferred.

Thus we observe for all temperatures a stretched exponential softening under load with a characteristic scaling exponent near ⅓ for all temperatures, while the characteristic relaxation time t_0 varies over six decades. These experimental findings are in agreement with the observation of domains (Krekhova & Lattermann 2008) and the predicted scaling law based upon a reversible splitting of domains (Baeurle *et al.* 2005).

For $t \to \infty$, the time dependent shear modulus $G(t, \theta)$ approaches 0. This means, that we have a viscoelastic soft magnetic material, without any long
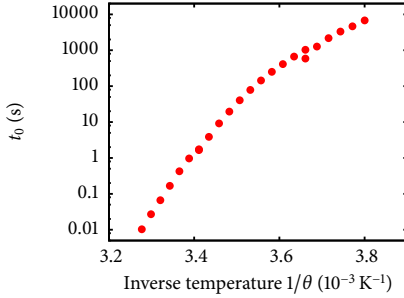
FIGURE 5.8: Arrhenius plot of the characteristic relaxation time. The data stem from fits of (5.3) to the measurements presented in figure 5.7.

term elasticity.

Periodic Driving Magnetically

In the effort of constraining G to some finite value, we are next selecting a specific time scale. We periodically drive the imposed magnetic induction according to

$$B(t) = B_0 + \Delta B \sin(2\pi f_D t). \tag{5.4}$$

Here, B_0 denotes the bias value, $\Delta B = 1.6\,\text{mT}$ the driving amplitude, and $f_D = 1\,\text{Hz}$ the driving frequency of the induction imposed by the Helmholtz-pair-of-coils. For each sample temperature, we measure the surface response for 24 different values of B_0. For small B_0, the surface oscillates with f_D around its meniscus-like shape, which becomes alternatingly more and less pronounced concave. Beyond a threshold, spikes appear which oscillate with the amplitude Δh around a mean height $\bar{h}$ with the driving frequency. For the whole range of values, we observe a harmonic response which can be described by

$$h(t) = \bar{h} + \Delta h \sin(2\pi f_D t + \phi). \tag{5.5}$$

In order to determine the quantities $\bar{h}$ and Δh, we measure the absorption of X-rays in the oscillating surface pattern by means of an X-ray movie. For each data point we record $n = 2200$ frames with a frame rate of $7.5\,\text{Hz}$. Each absorption picture is transformed into a height profile $h_n(x, y)$. From the series

of height profiles, we extract the desired quantities via the equations

$$\bar{h}(x, y) \;=\; \frac{1}{n} \sum_{1}^{n} h_n(x, y)$$

$$h_{\sin}(x, y) \;=\; \sum_{1}^{n} \sin(2\pi f_D n\Delta t)\, h_n(x, y)\, W(n\Delta t)$$

$$h_{\cos}(x, y) \;=\; \sum_{1}^{n} \cos(2\pi f_D n\Delta t)\, h_n(x, y)\, W(n\Delta t)$$

$$\Delta h(x, y) \;=\; \sqrt{h_{\sin}^2(x, y) + h_{\cos}^2(x, y)}\; \mathrm{sgn}(h_{\sin}),$$

with

$$\mathrm{sgn}(x) = \begin{cases} -1 & : & x < 0 \\ 0 & : & x = 0 \\ +1 & : & x > 0 \end{cases} \tag{5.6}$$

The time delay between two consecutive frames amounts to $\Delta t = (1/7.5)\,\mathrm{s}$, and $W(t) = N \exp\left(-(t - t_{1/2})^2/s^2\right)$ denotes a normalized Gaussian window function with $s = 0.4\, t_{1/2}$ and its centre at $t_{1/2}$, i.e. at the half of the measured time interval.

Figure 5.9 (a) displays the time averaged height of the central extremum of the surface estimated in this way from the series of measurements at five different temperatures. In the interval from $B_0 = 0\,\mathrm{mT}$ to around $24\,\mathrm{mT}$ one notices again a monotonic decrease of the central height, due to the growth of the meniscus at the container edge. For higher inductions, ferrogel spikes appear which again lead to a steep increase of $\bar{h}$ for all curves.

Also here, we use the maximal inclination of $\bar{h}(B_0)$, which is determined from a spline, as an estimate for the threshold. It is denoted by $\tilde{B}_{\mathrm{max.up}}$ and is listed in table 5.1 for all temperatures investigated. This estimate for the threshold is shifted for higher temperatures towards higher fields. The shift amounts only to $\approx 0.5\,\mathrm{mT}$.

Next, we present the oscillation amplitude Δh of the central spike, as shown in figure 5.9 (b). The amplitude is increasing with increasing temperatures, i.e. larger for a softer ferrogel. From the maximal increase, we determine an additional estimate for the threshold $\Delta\tilde{B}_{\mathrm{max.up}}$. The results are listed in table 5.1.
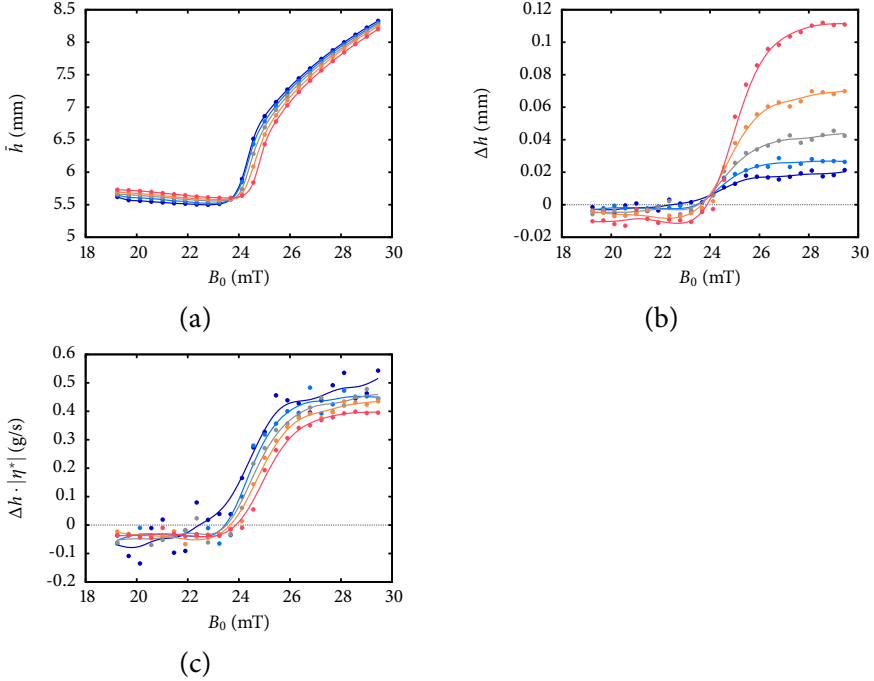
FIGURE 5.9: Amplitude of the central peak of the surface pattern (cf. figure 5.4) versus the bias of the magnetic induction B_0. (a) Time averaged height $\bar{h}$ (b) Oscillation amplitude Δh (c) Rescaled oscillation amplitude $\Delta h \cdot |\eta^*|$. The lines stem from a spline fit. The colour encodes the temperature the same way as in figure 5.5.

Once more the shift for different temperatures is only ≈ 0.5 mT.

The X-ray movies of our oscillating spikes show, that the response is always harmonic and never sub-harmonic. This is also true for a driven harmonic oscillator. For strong damping and a driving frequency not much smaller than the resonant frequency, the amplitude of an oscillator is inverse proportional to the damping constant. To uncover such a scaling in our measurements, we plot the rescaled amplitude $\Delta h \cdot |\eta^*|$ in figure 5.9 (c), where $|\eta^*| = |G|/\omega$ is the absolute value of the complex viscosity. Within the experimental resolution, the graphs collapse onto a master curve. This indicates that the increase of $\Delta h(B)$ under variation of θ stems solely from the softening of the ferrogel. Therefore, one possible simplified explanation for our experiment could be an

oscillator, where the driving force comes from the magnetic stress at the edge of the container and the viscosity provides the damping.

5.3.3 Comparison of the thresholds with predictions

Now we want to take a closer look at the experimentally determined thresholds of the Rosensweig instability and how they compare to the predictions by Bohlius *et al.* (2006*b*). For a ferrofluid, the threshold can be computed from the nonlinear magnetization curve, the density ρ and the surface tension σ via the linear stability analysis according to the book by Rosensweig (1985), § 7.1. The critical magnetization M_c of the fluid layer is given by

$$M_c^2 = \frac{2}{\mu_0} \left(1 + \frac{1}{r_c}\right) \sqrt{g\rho\sigma}. \tag{5.7}$$

Here $r_c = \sqrt{\mu_{ch}\mu_t}/\mu_0$ denotes the geometrical mean of the chord permeability $\mu_{ch} = \frac{B}{H}\big|_{H_c}$ and the tangent permeability $\mu_t = \frac{\partial B}{\partial H}\big|_{H_c}$ at the critical field. Together with $M(H)$ and the jump condition of the magnetic field at the base of the dish, $B = \mu_0\left[H + M(H)\right]$, the critical induction can be determined from these implicit equations.

For a ferrogel with a Hookean shear modulus G and a linear magnetization curve, Bohlius *et al.* (2006*b*) provide the expression (5.1). We combine this equation with equation (5.7) for a non-linear $M(H)$ to get the more general form

$$M_c^2 = \frac{2}{\mu_0} \left(1 + \frac{1}{r_c}\right) \left(\sqrt{g\rho\sigma} + G\right). \tag{5.8}$$

If either one of the elasticity ($G \neq 0$) or non-linearity ($M \neq \chi H$) is left out, this equation reduces to (5.1) or (5.7), respectively.

In table 5.1, we present the calculated critical inductions B_{cFG} according to equation (5.8). For all calculations, we utilize the storage modulus $G'(1\,\text{Hz})$ as determined by the oscillatory measurements (cf. figure 5.1). The other properties entering equation (5.8) are taken from section 5.2.2, accordingly. Specifically the surface tension is not well known for our gel. The value used here was $\sigma_{FF} = 28.7\,\text{mN/m}$. Calculations for $\sigma = 35\,\text{mN/m}$ show that a variation of σ does not change B_{cFG} by more than 5 %.

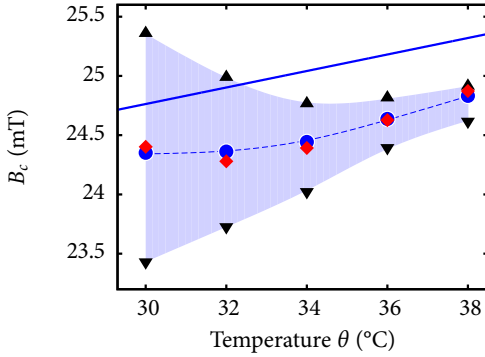The comparison between the experimentally determined thresholds in ta-

FIGURE 5.10: Temperature dependence of the thresholds. The black upward (downward) triangles mark $B_{max.up}$ ($B_{max.dn}$) for an adiabatic increase (decrease), respectively. The shaded area in between denotes the hysteresis. The blue circles and red diamonds show $\tilde{B}_{max.up}$ ($\Delta\tilde{B}_{max.up}$), respectively. The dashed line is just a guide for the eye. The theoretical value for a ferrofluid is displayed by the solid line.

ble 5.1 and the predictions by Bohlius *et al.* (2006*b*) reveals two prominent differences.

Firstly, we observe a decrease of the hysteresis of the pattern amplitude for a decrease of G, i.e. higher temperatures, when the magnetic induction is varied in a quasi-static manner. This hysteresis is denoted in figure 5.10 by the shaded area and the upward and downward oriented full triangles. In contrast, Bohlius *et al.* (2006*b*) predict an increase of the hysteresis under reduction of G for a ferrogel with *Hookean elasticity*.

This can be explained from the temperature dependent relaxation process of the ferrogel. The relaxation times are increasing from $\tau \approx 0.01\,\text{s}$ (at $32\,°\text{C}$) to $\tau \approx 10000\,\text{s}$ (at $-10\,°\text{C}$). At the same time the measurement protocol for a full ramping of the magnetic induction was kept at $2\,\text{h}$. The hysteresis increases because the material needs more and more time to follow a variation of B. We have checked that by increasing the cycle time from $2\,\text{h}$ to $4\,\text{h}$. The hysteresis was diminished, as shown in figure 5.6.

Secondly, whereas $G'(1\,\text{Hz})$ varies in the investigated temperature range over two decades (cf. figure 5.1), the threshold of the instability is varying only within $10\,\%$. This is in contrast to the model (Bohlius *et al.* 2006*b*) for a ferrogel with *Hookean elasticity*. However we found a different mechanical behaviour of our material. The shear modulus is strongly time-dependent and even vanishes for $t \to \infty$.

In an attempt to select a specific, finite value for G, we modulated the magnetic induction with a fixed amplitude and a frequency of $1\,\text{Hz}$ and applied this magnetic driving together with a magnetic bias induction B_0. Under increase of
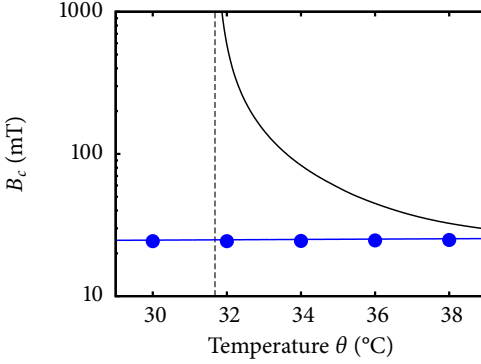
FIGURE 5.11: Comparison of theoretically (solid black line) and experimentally (filled circles) determined critical inductions, as listed in table 5.1. The solid blue line is the theory for a ferrofluid. Note, that in this scale, all experimental values collapse onto that line. The dashed line denotes the vertical asymptote of the theoretical curve at $\theta = 31.7\,°C$.

B_0 a threshold is overcome and we observe a steep increase of the time averaged peak height $\bar{h}$. The magnetic induction at which this transition occurs is marked in figure 5.10 by the blue filled circles. Also the oscillation amplitude Δh shows a steep increase under variation of B_0. The corresponding thresholds are shown in figure 5.10 by red diamonds. Within the experimental scatter both thresholds coincide. Similar to the static experiment, their values vary only in fractions of $1\,mT$ under decrease of the sample temperature θ.

In contrast, the theoretical value, estimated according to (5.8) at $G'(1\,Hz)$, increases drastically under decrease of θ, as shown in figure 5.11. Only for high temperatures, the experimental and theoretical values are close to each other. For lower temperatures, the gap between them increases drastically. According to (5.8) it even diverges at a critical shear modulus of

$$G_c = \frac{\mu_0}{4} M_S^2 - \sqrt{\rho g \sigma} = 77.8\,\text{Pa}. \tag{5.9}$$

For our gel, the saturation magnetization M_S of the ferrogel amounts to $M_S = 14.7\,kA/m$ and the divergence occurs at $\theta = 31.7\,°C$. Obviously, there is a mismatch of our complex, soft material and the linear model (5.8) when implementing $G'(1\,Hz)$.

Let us look more closely on the small variation of the experimentally determined thresholds in figure 5.10. We see that under an increase of the temperature all estimates for the onset of the instability are slightly shifted to higher inductions. This shift can be understood from the fact that for increasing θ the magnetization diminishes. Utilizing the $M(H, \theta)$-model by Ivanov & Kuznetsova

(2001), we have taken into account this effect. The corresponding results for B_{cFF} are marked in figure 5.10 by the solid line. The good agreement between the experiment and the plain Rosensweig estimate for the threshold computed in this way indicates that the shear modulus $G'(1\,\mathrm{Hz})$ has no influence on the threshold at all.

5.4 Conclusion

To conclude, we conducted the first measurements of the Rosensweig insta-bility in thermoreversible ferrogels. The present material shows a complex viscoelastic relaxation process with an interesting critical exponent $\beta \approx \frac{1}{3}$, for experiments carried out in the time domain. It is possibly explained by a reversible splitting of the polymer network into domains of different size (Lat-termann & Krekhova 2006; Baeurle *et al.* 2005). Due to this relaxation, the threshold of the Rosensweig peaks is not much different from the Rosensweig instability in ferrofluids under an adiabatic increase of a static magnetic field. However, the time scales are much slower. This is especially pronounced for the lower part of the investigated temperature range. Experiments with a periodic modulation of the magnetic field show that the *complex viscosity* can be used to describe the response of the ferrogel.

Such a complex elastic behaviour, however, is unsuitable to proof or rebut the model of the Rosensweig instability by Bohlius *et al.* (2006*b*), which was derived for just a Hookean shear modulus. Certainly soft matter with finite G for $t \to \infty$ would come closer to that model. One may think that a ferrogel with a higher gelator concentration will serve this aim. However, as a consequence for such a gel, the instability is completely hindered by the strong elastic modulus. Un-fortunately, the amount of magnetite cannot be increased further to overcome the critical magnetization (5.8). Here, magnetic gels incorporating particles with a higher saturation magnetization could solve this problem. Despite some attempts, with e.g. cobalt particles, such gels are not yet available.

TABLE 5.1: Critical inductions for various temperatures: B_{cFF} gives the results of (5.8) for $G = 0$ Pa, i.e. for a virtual ferrofluid with otherwise the material parameters of the ferrogel. B_{cFG} (mT) is estimated from G' at 1 Hz and the measured value of σ. Experimentally, the thresholds were determined from the maximal inclination of $h(B)$, as marked by $B_{max.up}$ for increasing B and $B_{max.dn}$ for decreasing B. From the oscillatory measurements we determine the maximal inclination of $\bar{h}(B)$, marked by $\tilde{B}_{max.up}$, and the maximal inclination of $\Delta h(B)$ abbreviated by $\Delta\tilde{B}_{max.up}$

θ (°C)	B_{cFF} (mT)	B_{cFG} (mT)	$B_{max.up}$ (mT)	$B_{max.dn}$ (mT)	$\tilde{B}_{max.up}$ (mT)	$\Delta\tilde{B}_{max.up}$ (mT)
30	24.76	∞	25.36	23.43	24.35	24.40
32	24.90	587.09	24.99	23.73	24.36	24.28
34	25.04	83.17	24.76	24.02	24.44	24.39
36	25.18	32.51	24.81	24.39	24.64	24.63
38	25.32	28.03	24.91	24.62	24.83	24.87

6 Conclusion

In this thesis, four different experiments with magnetic continua in homogeneous fields have been performed. These magnetic continua are synthetically created superparamagnetic liquids and gels, the magnetism of which is based on a dispersion of nanosized magnetic particles. Table 6.1 gives an overview of the distinct properties of each experiment (a) along with what has been achieved in the theoretical analysis so far and what would be the most important improvement (b), considering the experimental results.

Two geometric configurations are considered: a horizontally extended flat layer with a free surface as well as a spherical sample. In both cases, the application of a homogeneous magnetic field leads to changes of the shape of the free boundary. In the case of the spherical geometry, the sample is deformed into a prolate ellipsoid under the action of the field, a phenomenon named "magnetodeformational effect" by Raikher & Stolbov (2003). The magnetic field presumably remains homogeneous inside the ellipsoidal sample (Jackson 1998), and the transition of the shape is smooth. In case of the extended flat layer, an abrupt shape transition into a patterned state takes place, the normal field or Rosensweig instability. The magnetic field inside the sample is distorted by the

Experiment	Ferrofluid	Ferrogel	Static	Dynamic	Rosensweig
Single spike (2)	✓		✓		✓
Rosensweig dynamics (3)	✓			✓	✓
Ferrogel sphere (4)		✓	✓	✓	
Ferrogel Rosenweig (5)		✓		✓	✓

(a)

Theory	Analytic	Numerics	Static	Dynamic	Challenge
Single spike (2)		✓	✓		analytic expression
Rosensweig dynamics (3)	✓			✓	nonlinear dynamics
Ferrogel sphere (4)	✓		✓		viscoelasticity
Ferrogel Rosenweig (5)	✓		✓		viscoelasticity

(b)

TABLE 6.1: Overview of the experiments performed in this thesis (a) and the features of the existing theoretical work (b).

transition with the same wavelength as the pattern on the surface. In contrast to the smooth deformation of the sphere, this is an instability, which breaks the translational symmetry, and the transition occurs at a certain threshold value of the magnetic induction B_c.

These two shape transitions have already been known. However, in the case of the ferrogel sphere (chapter 4), an experimental realization was completely missing, even though theoretical predictions exist since 1960. Chapter 4 fills this gap and demonstrates that the magnetodeformational effect indeed exists and can even be exploited to measure Poisson's ratio of a soft gel, but it raises new questions. Specifically the viscous flow of a soft gel is not accounted for in the static theories, which makes the results difficult to compare. Therefore the experiment challenges the theoretical analysis to provide a dynamic theory, which can incorporate viscoelastic material properties, especially time dependent elastic moduli.

In the case of the normal field instability, the experiments in this thesis shed light on different limiting cases. In chapter 2, the ideal geometry of an infinitely extended flat layer is intentionally reduced to a cylinder such that only a single spike in the centre exists, and the solution space becomes rotationally symmetric. Two distinct experimental techniques and numerical simulations, the latter performed in close cooperation by a group in Athens, show a convincing agreement within a few percent. It remains an open question, whether the result can be deduced in analytic form, however.

In chapter 3, the nonlinear dynamics of the normal field instability is studied at very low Reynolds numbers. The linear growth rate for the growth and decay of the pattern at small amplitudes is extracted from the measurements and compared with existing theories, which are mainly restricted to the linear regime. Nonlinear amplitude equations exist, but they can only describe the dynamics of the growth in the immediate vicinity of the critical point so far. Utilizing a highly viscous fluid, the experiments in chapter 3 allow a reconstruction of a fully nonlinear amplitude equation, which can serve as a basis for the comparison to further theoretical analysis. Additionally, localized patterns are observed which arise spontaneously in the neighbourhood of the unstable solution branch. An in-depth experimental study and theoretical analysis of this phenomenon can be performed in future work.

The dynamics of the normal field instability is also utilized as a tool in chapter 5, which deals with the experimental realization of the instability in a ferrogel.
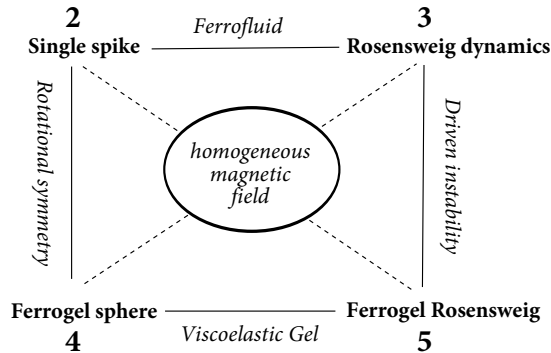
FIGURE 6.1: Relations between the experiments. The numbers and the terms in boldface represent the four main chapters of this thesis. The common properties between them are marked in italics along the connecting lines (solid and dashed).

In contrast to chapter 3, where a Newtonian fluid is used, now a viscoelastic ferrogel is employed. This is a consequence of the need for a very soft material, such that the growth of the pattern is not completely suppressed by the elastic forces. The theory by Bohlius *et al.* (2006*b*), on the other hand, does not account for viscoelastic effects. An extension of the theory, which incorporates viscoelasticity and an external driving, is therefore needed to quantitatively compare the experimental results with, similar to the case of the ferrogel sphere.

All the experiments in this thesis are interconnected by various features into a graph, as described in the previous paragraphs, and share the common property of homogeneous magnetic fields. These relations are visualized in figure 6.1.

To conclude, the surface deformation of magnetic continua in homogeneous fields has been examined on the basis of four phenomena. Each experiment reveals a field which is not yet completely understood and poses a challenge to the theoretical analysis, as seen in table 6.1 (b). Further experimental work can be directed towards unexplored phenomena such as the spontaneous formation of localized patterns.

Bibliography

ABOU, B., WESFREID, J.-E. & ROUX, S. 2001 The normal field instability in ferrofluids: hexagon-square transition mechanism and wavenumber selection. *J. Fluid. Mech.* **416**, 217–237.

ABRAMOWITZ, M. & STEGUN, I. 1965 *Handbook of mathematical functions: with formulas, graphs, and mathematical tables*, 9th edn. Courier Dover Publications.

ANDERSSEN, R. S., HUSAIN, S. A. & LOY, R. J. 2004 The Kohlrausch function: properties and applications. *ANZIAM J.* **45**, C800–C816.

ARISTOTLE 350 B.C. *Physics*. Athens.

BABINCOVÁ, M., LESZCZYNSKA, D., SOURIVONG, P., ČIČMANEC, P. & BABINEC, P. 2001 Superparamagnetic gel as a novel material for electromagnetically induced hyperthermia. *J. Magn. Magn. Mater.* **225**, 109–112.

BACRI, J. C. & SALIN, D. 1982 Instability of ferrofluid magnetic drops under magnetic field. *J. Phys. Lett.* **43**, 649–654.

BACRI, J.-C. & SALIN, D. 1983 Dynamics of the shape transition of a magnetic ferrofluid drop. *J. Phys. Lett.* **44**, 415–420.

BACRI, J.-C. & SALIN, D. 1984 First-order transition in the instability of a magnetic fluid interface. *J. Phys. Lett.* **45**, L559–L564.

BAEURLE, S. A., HOTTA, A. & GUSEV, A. A. 2005 A new semi-phenomenological approach to predict the stress relaxation behavior of thermoplastic elastomers. *Polymer* **46**, 4344–4354.

BASHTOVOI, V. G. 1978 Surface stability of a magnetized liquid covered with a thin elastic film. *Magnetohydrodynamics* **14** (4), 408–410.

BAYAT, N., NETHE, A., GULDBAKKE, J., HESSELBACH, J., NALETOVA, V., STAHLMANN, H.-D., UHLMANN, E. & ZIMMERMANN, K. 2009 Technical applications. In *Colloidal Magnetic Fluids: Basics, Development and Application of Ferrofluids* (ed. S. Odenbach), *Lect. Notes Phys.*, vol. 763, chap. 6, pp. 359–430. Berlin, Heidelberg, New York: Springer.

BERKOVSKI, B. & BASHTOVOY, V. 1996 *Magnetic fluids and applications handbook*, 1st edn. New York: Begell house, inc.

BERRY, G. & PLAZEK, D. 1997 On the use of stretched-exponential functions for both linear viscoelastic creep and stress relaxation. *Rheologica Acta* **36**, 320–329.

BLUMS, E., CEBERS, A. & MAIOROV, M. M. 1997 *Magnetic Fluids*. Walter de Gruyter.

BOHLIUS, S., BRAND, H. R. & PLEINER, H. 2006*a* Surface waves and Rosensweig instability in isotropic ferrogels. *Z. Phys. Chem* **220**, 97–104.

BOHLIUS, S., BRAND, H. R. & PLEINER, H. 2008 Amplitude equation for the rosensweig instability. *Prog. Theor. Phys. Supp.* **175**, 27–36.

BOHLIUS, S., PLEINER, H. & BRAND, H. R. 2006*b* Pattern formation in ferrogels: analysis of the Rosensweig instability using the energy method. *J. Phys.: Condens. Matter* **18**, 2671–2684.

BOHLIUS, S., PLEINER, H. & BRAND, H. R. 2007 Solution of the adjoint problem for instabilities with a deformable surface: Rosensweig and Marangoni instability. *Phys. Fluids* **19**, 094103.

BOHR, N. & WHEELER, J. A. 1939 The mechanism of nuclear fission. *Phys. Rev.* **56**, 426–450.

BOUDOUVIS, A. G. 1987 Mechanisms of surface instabilities and pattern formation in ferromagnetic liquids. PhD thesis, University of Minnesota, Minneapolis, MN, USA.

BOUDOUVIS, A. G., PUCHALLA, J. L. & SCRIVEN, L. E. 1988 Magnetohydrostatic equilibria of ferrofluid drops in external magnetic fields. *Chem. Eng. Comm.* **67**, 129–144.

BOUDOUVIS, A. G., PUCHALLA, J. L., SCRIVEN, L. E. & ROSENSWEIG, R. E. 1987 Normal field instability and patterns in pools of ferrofluid. *J. Magn. Magn. Mater.* **65**, 307–310.

BUSSE, F. H. 1967 The stability of finite amplitude cellular convection and its relation to an extremum principle. *J. Fluid Mech.* **30**, 625–649.

COLLIN, D., AUERNHAMMER, G. K., GAVAT, O., MARTINOTY, P. & BRAND, H. R. 2003 Frozen-in magnetic order in uniaxial magnetic gels: Preparation and physical properties. *Macromol. Rapid Commun.* **24**, 737–741.

COWLEY, M. D. & ROSENSWEIG, R. E. 1967 The interfacial stability of a ferro-magnetic fluid. *J. Fluid Mech.* **30**, 671–688.

CROSS, M. C. & HOHENBERG, P. C. 1993 Pattern formation outside of equilibrium. *Rev. Mod. Phys.* **65**, 851–1112.

CROW, F. C. 1977 The aliasing problem in computer-generated shaded images. *Commun. ACM* **20**, 799–805.

DICKEY, F. M. & ROMERO, L. A. 1991 Normalized correlation for pattern recognition. *Opt. Lett.* **16**, 1186.

DUSSAN, E. B. 1979 On the spreading of liquids on solid surfaces: Static and dynamic contact lines. *Ann. Rev. Fluid Mech.* **11**, 371–400.

EMBS, J. P., WAGNER, C., KNORR, K. & LÜCKE, M. 2007 Measuring the anomalous dispersion branch of surface waves on ferrofluids. *Europhys. Lett.* **78**, 44003.

FARADAY, M. 1846 On the magnetic condition of all matter. *Philos. Trans. R. Soc. London* **136**, 21–41.

FILIPCSEI, G., CSETNEKI, I., SZILÁGYI, A. & ZRÍNYI, M. 2007 Magnetic field-responsive smart polymer composites. *Adv. Poly. Sci.* **206**, 137–189.

FLAMENT, C., LACIS, S., BACRI, J., CEBERS, A., NEVEU, S. & PERZYNSKI, R. 1996 Measurements of ferrofluid surface tension in confined geometry. *Phys. Rev. E* **53**, 4801–4806.

FLEMING, J. A. & DEWAR, J. 1898 On the magnetic susceptibility of liquid oxygen. *Proc. R. Soc. London* **63**, 311–329.

FRIEDRICHS, R. 2002 Low symmetry patterns on magnetic fluids. *Phys. Rev. E* **66**, 066215.

FRIEDRICHS, R. & ENGEL, A. 2000 Statics and dynamics of a single ferrofluid-peak. *Eur. Phys. J. B* **18**, 329–335.

FRIEDRICHS, R. & ENGEL, A. 2001 Pattern and wave number selection in magnetic fluids. *Phys. Rev. E* **64**, 021406.

GAILITIS, A. 1977 Formation of the hexagonal pattern on the surface of a ferromagnetic fluid in an applied magnetic field. *J. Fluid Mech.* **82**, 401–413.

DE GENNES, P.-G. 1985 Wetting: Statics and dynamics. *Rev. Mod. Phys.* **57**, 827–863.

GOLLWITZER, C., KREKHOVA, M., LATTERMANN, G., REHBERG, I. & RICHTER, R. 2009*a* Surface instabilities and magnetic soft matter. *Soft Matter* **5**, 2093–2100.

GOLLWITZER, C., MATTHIES, G., RICHTER, R., REHBERG, I. & TOBISKA, L. 2007 The surface topography of a magnetic fluid: a quantitative comparison between experiment and numerical simulation. *J. Fluid Mech.* **571**, 455–474.

GOLLWITZER, C., REHBERG, I. & RICHTER, R. 2006 Via hexagons to squares in ferrofluids: experiments on hysteretic surface transformations under variation of the normal magnetic field. *J. Phys.: Condens. Matter* **18**, 2643–2656.

GOLLWITZER, C., SPYROPOULOS, A. N., PAPATHANASIOU, A. G., BOUDOUVIS, A. G. & RICHTER, R. 2009*b* The normal field instability under side-wall effects: comparison of experiments and computations. *New Journal of Physics* **11**, 053016.

GOLLWITZER, C., TURANOV, A., KREKHOVA, M., LATTERMANN, G., REHBERG, I. & RICHTER, R. 2008 Measuring the deformation of a ferrogel sphere in a homogeneous magnetic field. *J. Chem. Phys.* **128**, 164709.

GREEN, P. & SILVERMAN, B. 1994 *Nonparametric regression and generalized linear models: a roughness penalty approach*. Chapman & Hall/CRC.

HARDY, R. 1990 Theory and applications of the multiquadric-biharmonic method. 20 years of discovery 1968-1988. *Computers & Mathematics with Applications* **19**, 163–208.

HARKINS, W. D. & JORDAN, H. F. 1930 A method for the determination of surface and interfacial tension from the maximum pull on a ring. *J. Amer. Chem. Soc.* **52**, 1747–1750.

HELLER, J. P. 1960 An unmixing demonstration. *Am. J. Phys.* **28**, 348–353.

HICKEY, R. & SCHIBECI, R. A. 1999 The attraction of magnetism. *Phys. Educ.* pp. 383–388.

HOTTA, A., CLARKE, S. M. & TERENTJEV, E. M. 2002 Stress Relaxation in Transient Networks of Symmetric Triblock Styrene-Isoprene-Styrene Copolymer. *Macromolecules* **35**, 271–277.

IVANOV, A. O., KANTOROVICH, S. S., REZNIKOV, E. N., HOLM, C., PSHENICH-NIKOV, A. F., LEBEDEV, A. V., CHREMOS, A. & CAMP, P. J. 2007 Magnetic properties of polydisperse ferrofluids: A critical comparison between experiment, theory, and computer simulation. *Phys. Rev. E* **75**, 061405.

IVANOV, A. O. & KUZNETSOVA, O. B. 2001 Magnetic properties of dense ferrofluids: An influence of interparticle correlations. *Phys. Rev. E* **64**, 041405.

JACKSON, J. D. 1998 *Classical Electrodynamics*. New York: Wiley.

JARKOVA, E., PLEINER, H., MÜLLER, H. W. & BRAND, H. R. 2003 Hydrodynamics of isotropic ferrogels. *Phys. Rev. E* **68**, 41706.

JOHNSON, T. J., ROSS, D. & LOCASCIO, L. E. 2002 Rapid microfluidic mixing. *Anal. Chem.* **74**, 45–51.

JOULE, J. P. 1842 On a new class of magnetic forces. *Annals of Electricity* **8**, 219.

KAKESHITA, T., TAKEUCHI, T., FUKUDA, T., TSUJIGUCHI, M., SABURI, T., OSHIMA, R. & MUTO, S. 2000 Giant magnetostriction in an ordered FePt single crystal exhibiting a martensitic transformation. *Applied Physics Letters* **77**, 1502.

KISTLER, S. F. & SCRIVEN, L. E. 1983 Coating flow computations. In *Computational Analysis of Polymer Processing* (ed. J. Pearson & S. Richardson), pp. 243–299. Applied Science Publishers Ltd.

KNIELING, H., RICHTER, R., REHBERG, I., MATTHIES, G. & LANGE, A. 2007 Growth of surface undulations at the Rosensweig instability. *Phys. Rev. E* **76**, 66301.

KOHLRAUSCH, F. 1863 Über die elastische Nachwirkung bei der Torsion. *Pogg. Ann. Phys.* **119**, 337–368.

KOHLRAUSCH, R. 1854 Theorie des Elektrischen Rückstandes in der Leidener Flasche. *Pogg. Ann. Phys.* **91**, 179–214.

KOHR, M. & POP, I. 2004 *Viscous incompressible flow for low Reynolds numbers*. Ashurst, Southampton, UK: WIT Press.

KREKHOVA, M. & LATTERMANN, G. 2008 Thermoreversible organoferrogels: morphological, thermal and magnetic characterisation. *J. Mater. Chem.* **18**, 2842–2848.

LAHAYE, T., KOCH, T., FRÖHLICH, B., FATTORI, M., METZ, J., GRIESMAIER, A., GIOVANAZZI, S. & PFAU, T. 2007 Strong dipolar effects in a quantum ferrofluid. *Nature (London)* **448**, 672.

LANDAU, L. D. & LIFSCHITZ, E. M. 1960 *Electrodynamics of Continuous Media*, 3rd edn., , vol. 8. Oxford: Pergamon.

LANGE, A. 2002*a* The adjoint problem in the presence of a deformed surface: the example of the Rosensweig instability on magnetic fluids. *Int. J. Modern Phys. B* **16**, 1155.

LANGE, A. 2002*b* Kelvin force in a layer of magnetic fluid. *J. Magn. Magn. Mater.* **241**, 327–329.

LANGE, A. 2003 Decay of metastable patterns for the Rosensweig instability: revisiting the dispersion relation. *Magnetohydrodynamics* **39**, 65–68.

LANGE, A., REIMANN, B. & RICHTER, R. 2000 Wave number of maximal growth in viscous magnetic fluids of arbitrary depth. *Phys. Rev. E* **61**, 5528–5539.

LANGE, A., REIMANN, B. & RICHTER, R. 2001 Wave number of maximal growth in viscous ferrofluids. *Magnetohydrodynamics* **37**, 261.

LAO, L. & RAMANUJAN, R. 2004 Magnetic and hydrogel composite materials for hyperthermia applications. *J. Mater. Sc.: Mater. Med.* **15** (10), 1061–1064.

LATTERMANN, G. & KREKHOVA, M. 2006 Thermoreversible ferrogels. *Macromol. Rapid Commun.* **27**, 1373–1379.

LOVE, A. 1944 *A Treatise on the Mathematical Theory of Elasticity*. Courier Dover Publications.

MAHR, T. & REHBERG, I. 1998 Nonlinear dynamics of a single ferrofluid-peak in an oscillating magnetic field. *Physica D: Nonlinear Phenomena* **111**, 335–346.

MATTHIES, G. & TOBISKA, L. 2005 Numerical simulation of normal-field instability in the static and dynamic case. *J. Magn. Magn. Mater.* **289**, 346–349.

MAXWELL, J. C. 1861 On physical lines of forces. *Phil. Mag. S. 4* **21**.

MEGALIOS, E., KAPSALIS, N., PASCHALIDIS, J., PAPATHANASIOU, A. G. & BOUDOUVIS, A. G. 2005 A simple optical device for measureing free surface deformations of nontransparent liquids. *Journal of Colloid and Interface Science* **288**, 505–512.

MEISSNER, R. 2002 *The Little Book of Planet Earth*. Berlin, Heidelberg, New York: Springer.

MERRIAM-WEBSTER, I. 1999 *Merriam-Webster's collegiate dictionary*, 10th edn. Springfield, Massachusettes: Merriam-Webster, Inc.

MOROZOV, K., SHLIOMIS, M. & YAMAGUCHI, H. 2009 Magnetic deformation of ferrogel bodies: Procrustes effect. *Phys. Rev. E* **79**, 040801(R).

NEUMAIER, A. 1998 Solving ill-conditioned and singular linear systems: A tutorial on regularization. *SIAM Review* **40**, 636–666.

DU NOÜY, P. L. 1919 A new apparatus for measuring surface tension. *The Journal of General Physiology* **1**, 521–524.

ODENBACH, S., ed. 2009 *Colloidal Magnetic Fluids: Basics, Development and Application of Ferrofluids*, *Lect. Notes Phys.*, vol. 763. Berlin, Heidelberg, New York: Springer.

ØRSTED, H. C. 1821 On electromagnetism. *Annals of Philosophy* pp. 321–337.

PAPATHANASIOU, A. G. & BOUDOUVIS, A. G. 1998 Three-dimensional instabilities of ferromagnetic liquid bridges. *Comput. Mech.* **21**, 403–408.

PAPELL, S. S. 1965 Low viscosity magnetic fluid obtained by the colloidal suspension of magnetic particles. US patent No. 3215572.

PETER, R., HILT, M., ZIEBERT, F., BAMMERT, J., ERLENKÄMPER, C., LORSCHEID, N., WEITENBERG, C., WINTER, A., HAMMELE, M. & ZIMMERMANN, W. 2005 Stripe-hexagon competition in forced pattern-forming systems with broken up-down symmetry. *Phys. Rev. E* **71**, 046212.

PICARD, R. R. & COOK, R. D. 1984 Cross-validation of regression models. *J. Am. Stat. Assoc* **79**, 575–583.

POPPLEWELL, J. & SAKHNINI, L. 1995 The dependence of the physical and magnetic properties of magnetic fluids on particle size. *Journal of Magnetism and Magnetic Materials* **149**, 72–78.

POWELL, M. J. D. 1990 *The Theory of Radial Basis Function Approximation in 1990*, *Advances in Numerical Analysis*, vol. 2, pp. 105–210. Oxford University Press.

PURCELL, E. M. 1977 Life at low Reynolds number. *Am. J. Phys.* **45**, 3–11.

RAIKHER, Y. L. & STOLBOV, O. V. 2003 Magnetodeformational effect in ferrogel samples. *J. Magn. Magn. Mater.* **258-259**, 477–479.

RAIKHER, Y. L. & STOLBOV, O. V. 2005*a* Deformation of an ellipsoidal ferrogel sample in a uniform magnetic field. *J. Appl. Mech. Tech. Phys.* **46**, 434–443.

RAIKHER, Y. L. & STOLBOV, O. V. 2005*b* Magnetodeformational effect in ferrogel objects. *J. Magn. Magn. Mater.* **289**, 62–65.

RAULT, J. 2000 Origin of the Vogel-Fulcher-Tammann law in glass-forming materials: the α-β bifurcation. *Journal of Non-Crystalline Solids* **271**, 177 – 217.

REIMANN, B., RICHTER, R., REHBERG, I. & LANGE, A. 2003 Oscillatory decay at the Rosensweig instability: Experiment and theory. *Phys. Rev. E* **68**, 036220.

RICHTER, R. & BARASHENKOV, I. 2005 Two-dimensional solitons on the surface of magnetic liquids. *Phys. Rev. Lett.* **94**, 184503.

RICHTER, R. & BLÄSING, J. 2001 Measuring surface deformations in magnetic fluid by radioscopy. *Rev. Sci. Instrum.* **72**, 1729–1733.

RICHTER, R. & LANGE, A. 2009 Surface instabilities of ferrofluids. In *Colloidal Magnetic Fluids: Basics, Development and Application of Ferrofluids* (ed. S. Odenbach), *Lect. Notes Phys.*, vol. 763, chap. 3. Berlin, Heidelberg, New York: Springer.

RINDE, J. 1970 Poisson's ratio for rigid plastic foams. *Journal of Applied Polymer Science* **14**, 1913–1926.

ROSENSWEIG, R. 1987 Magnetic fluids. *Ann. Rev. Fluid Mech.* **19**, 437–463.

ROSENSWEIG, R. E. 1985 *Ferrohydrodynamics*. Cambridge, New York, Melbourne: Cambridge University Press.

SALIN, D. 1993 Wave vector selection in the instability of an interface in a magnetic or electric field. *Europhys. Lett.* **21**, 667.

SCHATZ, M. F., VANHOOK, S. J., McCORMICK, W. D., SWIFT, J. & SWINNEY, H. L. 1995 Onset of surface-tension-driven Bénard convection. *Phys. Rev. Lett.* **75**, 1938–1941.

SPYROPOULOS, A. N., PAPATHANASIOU, A. G. & BOUDOUVIS, A. G. 2010 Mechanisms of pattern selection in magnetic liquid pools of finite diameter: Realistic computations and experiments. preprint.

STROBL, G. 1997 *The Physics of Polymers: Concepts for Understanding Their Structures and Behavior*. Berlin, Heidelberg, New York: Springer.

Trahms, L. 2009 Biomedical applications of magnetic nanoparticles. In *Colloidal Magnetic Fluids: Basics, Development and Application of Ferrofluids* (ed. S. Odenbach), *Lect. Notes Phys.*, vol. 763, chap. 5, pp. 327–358. Berlin, Heidelberg, New York: Springer.

Turing, A. 1952 The chemical basis of morphogenesis. *Philos. Trans. R. Soc. London, Ser. B* **237**, 37–72.

Varga, Z., Feher, J., Filipcsei, G. & Zrinyi, M. 2003 Smart nanocomposite polymer gels. *Macromol. Symp.* **200**, 93.

Wang, S., Ge, F. & Liu, T. 2006 Evaluating edge detection through boundary detection. *EURASIP J. Appl. Signal Process.* **2006**, 213–213.

Weilepp, J. & Brand, H. R. 1996 Competition between the Bénard-Marangoni and the Rosensweig instability in magnetic fluids. *J. Phys. II France* **6**, 419.

Wikipedia 2009 `http://en.wikipedia.org/wiki/File:Magnetite_Lodestone.jpg`.

Williams, G. & Watts, D. C. 1970 Non-symmetrical dielectric relaxation behaviour arising from a simple empirical decay function. *Trans. Faraday Soc.* **66**, 80–85.

Zimmermann, K., Naletova, V. A., Zeidis, I., Böhm, V. & Kolev, E. 2006 Modelling of locomotion systems using deformable magnetizable media. *J. Phys.: Condens. Matter* **18**, 2973–2984.

Zimmermann, K., Naletova, V. A., Zeidis, I., Böhm, V., Turkov, V. A., Kolev, E., Lukashevich, M. V. & Stepanov, G. V. 2007 A deformable magnetizable worm in a magnetic field - a prototype of a mobile crawling robot. *J. Magn. Magn. Mater.* **311**, 450–453.

Zrínyi, M. 2000 Intelligent polymer gels controlled by magnetic fields. *Colloid. Polym. Sci.* **278**, 103.

Zrínyi, M., Barsi, L. & Büki, A. 1996 Deformation of ferrogels induced by nonuniform magnetic fields. *J. Chem. Phys.* **104**, 8750–8756.

ZRÍNYI, M., BARSI, L. & BÜKI, A. 1997a Ferrogel: a new magneto-controlled elastic medium. *Polymer Gels and Networks* **5**, 415–427.

ZRÍNYI, M., BARSI, L., SZABO, D. & KILIAN, H.-G. 1997b Direct observation of abrupt shape transition in ferrogels induced by nonuniform magnetic field. *J. Chem. Phys.* **106**, 5685–5692.

Acknowledgement